Title

Lamellar Membrane Perturbation by Surface-Active and Biological Molecules

Author

Speer, Daniel John

Publication Date

2023

Peer reviewed|Thesis/dissertation

Lamellar Membrane Perturbation by Surface-Active and Biological Molecules

By

DANIEL JOHN SPEER
DISSERTATION

Submitted in partial satisfaction of the requirements for the degree of

DOCTOR OF PHILOSOPHY

in

Chemistry and Chemical Biology

in the

OFFICE OF GRADUATE STUDIES

of the

UNIVERSITY OF CALIFORNIA

DAVIS

Approved:

_____
Atul N. Parikh, Chair

_____
Gang-yu Liu

_____
Dylan T. Murray

Committee in Charge

2023

Acknowledgements

I am beyond indebted to the people in my life who have made it that much better. I cannot begin to even fathom where I would be without these people and their community. I love you all so much.

First, thank you to the friends I have made while living in Davis and all of the life you bring me. To Nathan Yoshino, you have been my emotional rock for years and I will always be grateful for your involvement in my life more than you could ever imagine. To Steven Gralinski, your unending joy for life and constant stoke for the next day has been so admirable and I can only hope to carry myself like you. To Hillary and Dustin Sutton, thank you for keeping me grounded and moving forward amongst all of the trials and tribulations. To Hannah Kramer and Emily Kramer, our friendship is something I would never give away for the world and your support carried me through more than I ever could say. To Kellen Ochi and Jayce Taylor, your endless outpouring of love for your communities and each other is beautiful and awe-inspiring. To Zachary Crawford and Aria Ta, thank you all for your encouragement to be myself and love who I am. To Ellen Yuska, Sarah Thornton, and Dana Lawrence, thank you for literally being there with me in the midst of it all. To Kendal Hiemke, thank you for letting me be me. To Daniel Zoltek, your wisdom is invaluable and I'm glad I got to see how much you love yourself. To Minh Hoang and Brad Wolf, all of your care when I was a small fledging has helped me sprout into the beautiful creature I am today. To Michelle Vangsycha, thank you for always being open to conversations about our lives and supporting me through it all. To Ben Souvey, Amanda Meroux, and Orion Edwards, thank you for being such great friends and joining me out on the field to run when it's too hot. To Austin Lourie and Jules Madigan, thank you for your camaraderie both on and off the field. To Seven, your two-week venture in Davis was an absolute light in my life, rest in peace. To Ruth Thurkill, Anthony Soukey, Hannah Brinkman, everyone that works on the 2nd floor of Ghausi Hall, Ciera Street, Marisa Paipongna, everyone who works at Temple Coffee, Heidi Ballard and the Center for Community and Citizen Science, Kris and Kara, Lyric, and everyone who let me crash on their couch, thank you so much for bringing me life.

Second, thank you to my friends in the ultimate frisbee community and all of my growth you've catalyzed. To Munis Thahir, your joy and fire is contagious, please never stop being yourself and discovering more. To Jackie Wataoka and Chris Lung, thank you for letting me crash on your floor and always being so supportive of my athletic journey. To Mischief Ultimate, thank you so much for everything you have done for me as I can only hope to reciprocate the same for you all. And to my physical therapist Dr. Madeline Kennedy, thank you for always helping me feel physically and mentally one.

Third, thank you to my fellow labmates for your support and commiseration. To Pallavi Sambre, thank you so much for being who you are. Your unending support, kindness, and wisdom have been absolutely vital to my success here through my Ph.D. To Caroline Love, thank you for always sharing the emotional labor of graduate school and being a light. To Chris Carnahan and Archan Vyas, thank you for your exemplary dedication and realness. To Zhongrui Liu, thank you for your help and our conversations regarding our futures. All of you have helped me tackle this experience and manage the murky waters of STEM research.

Last but not least, thank you for the physical places and sensations that have helped me find peace. Thank you to the valley wind and the valley heat, your continuity helps keep my brain sane. Thank you to the UC Davis Arboretum, your tranquility is something I wish to exemplify in my life. Thank you to the Pacific Ocean and the California coastline, your beauty has helped ground me in what matters. Thank you to the mandarin tree, the pear tree, and the Meyer lemon tree in my backyard, your lives have taught me the importance of attention and care. To Kai the aloe vera, Lilith the hydrangea (rest in peace), Farrah the pothos, Cassius Jr. the succulent, and Pluto the spider (rest in peace), thank you for your regularity in my life.

And to you reading this, I may not ever meet you but I'm thankful that you invested your time into learning more about my work. Please love yourself and do what matters to you.

Abstract

Like impressionist art, a multitude of subtle and complex interactions determine the behavior of biological systems but a generalized perception loses significant resolution. This is true within the discipline of soft matter, where the chemical multiplicity of the involved components and their resulting physical consequences within lamellar mesophase assemblies are commonly ignored. Therefore, it is imperative to investigate the minute thermodynamic considerations between varied lipidic lamellar mesophases and biologically relevant dopants (like surface-active agents and proteinaceous content) and their resulting physical behaviors. By using various microscopy techniques and x-ray diffraction measurements, lamellar mesophase behavior can be monitored upon the addition (in real-time or post-doping event) of these surface-active and biological substances, and the resulting analyses elucidate the microscopic information others have commonly missed. Such studies can not only enlighten scientists with a higher-level understanding of amphiphilic systems but also lead to the development of unique structural assemblies for various applications.

In a larger perspective, this dissertation aims to assemble structurally-diverse lamellar mesophases and expose them to surface-active molecules (also written as surfactant or detergent) and proteinaceous content in varying methods to connect macroscopic and microscopic information. Employing various methodologies like directed aqueous hydration, water vapor hydration, and electroformation, both multilamellar and unilamellar mesophases populated by common lipids and fluorescently-tagged phospholipids were assembled. Such assemblies were then perturbed by symmetric (or internalized) or asymmetric (or external) doping of the focal substances. The consequential physical and structural properties of the mixed-component systems were then investigated to understand the impacts of chemical multiplicity. This dissertation only begins to expound the subtleties of chemistry within lamellar mesophases and question the value of generalized models of membrane behavior. Through these efforts, a new, adaptable, and inclusive intellectual framework of membranes can be developed and considered.

TABLE OF CONTENTS

LIST OF ABBREVIATIONS

AC	Alternating current
AFM	Atomic force microscopy
C	Cubic phase
CHOL	Cholesterol
CMC	Critical micelle concetration
D	Lamellar spacing
D_{hh}	Headgrou-to-headgroup distance
D_t	Bilayer thickness
D_w	Water layer thickness
DDAPS	*n*-dodecyl-*N,N*-dimethyl-3-ammonio-1-propanesulfonate
DOPC	1,2-dioleoyl-*sn*-glycero-3-phosphocholine
DOPG	1,2-dioleoyl-*sn*-glycero-3-phospho-(1'-rac-glycerol) (sodium salt)
EDTA	Ethylenediaminetetraacetic acid
F_r	Bilayer rupture force
FRAP	Fluorescence recovery after photobleaching
FWHM	Full width at half maximum
GUVs	Giant Unilamellar Vesicles
h	Diffraction order
H	Hexagonal phase
H_{II}	Inverted hexagonal phase
I_n	Integrated intensity of nth order peaks of XRD measurements
ITO	Indium tin oxide
J	Curvature
L_α	Lamellar phase
L_d	Liquid-disordered phase
L_o	Liquid-ordered phase
LB	Luria-Bertani
MAPs	Membrane active proteins
MOPS	3-(*N*-Morpholino)propanesulfonic acid
NBD-DPPE	1,2-dipalmitoyl-*sn*-glycero-3-phosphoethanolamine-*N*-(7-nitro-2-1,3-benzoxadiazol-4-yl) (ammonium salt)
O-Lyso-PC	1-oleoyl-2-hydroxy-*sn*-glycero-3-phosphocholine
POPC	1-palmitoyl-2-oleoyl-sn-glycero-3-phosphocholine

q	Peak location
Q	Scattering Vector
R_e	Detergent-lipid ratio
R_e^{sat}	Saturated detergent-lipid ratio
R_e^{sol}	Solubilizing detergent-lipid ratio
RH	Relative humidity
Rho B-DOPE	1,2-dioleoyl-*sn*-glycero-3-phosphoethanolamine-*N*-(lissamine rhodamine B sulfonyl) (ammonium salt)
SDS	Sodium dodecyl sulfate
SM	Sphingomyelin
SUVs	Small unilamellar vesicles
TFA	Trifluoroacetic acid
Vpp	Peak-to-peak voltage
XRD	X-ray diffraction

LIST OF FIGURES

CHAPTER 1 – Introduction to Phospholipid Assembly and Lamellar Mesophase Perturbation

Life is commonly assembled from the structural organization of smaller building blocks. This can be true across a plethora of size and length scales, for example bodily tissues are formulated from cells which are derived from organelles and so on. Therefore, it is of merit to characterize the building blocks of living systems to understand their larger biological functionality.[1] One such function of life is the cellular membranes and its perturbation.[2] Cellular membranes are generally composed of a semi-permeable bilayer of phospholipid molecules as well as other biological materials like proteins and polysaccharides, and they have previously been characterized using the famous "fluid mosaic model" from Singer and Nicolson in 1972.[3] However, further studies have depicted much more complicated dynamics within membranes, including the disruption of the bilayer structure by biological materials, leading to constantly evolving appreciations of membrane behavior.[4] Therefore, the chemical and biological components that perturb membranes warrant themselves as worthwhile subjects of study to better characterize the transportation and isolation of biological material and information.

One such membrane-active component is the amphiphilic, micelle-forming surface-active agent (also known as surfactants or detergents) which can solubilize lamellar membranous structures into isotropic solutions of mixed-component micelles.[5] Such behavior has been exhaustively studied, from which a generalized "three-stage model" was developed. First proposed by Helenius and Simons in 1975, the consensus model describes there stages of concentration-dependent equilibrium between the lipidic bilayer and perturbing surfactant as well as the resulting morphological evolution of the system.[6] The process begins with stage 1, where detergents molecules first dope into the bilayer up to an effective concentration below a membrane-dependent saturation value. Here, the percolation of surfactants within the membrane results in an asymmetry of mass density, surface area, chemical composition, tension, and spontaneous curvature (or occupied volume) which alters the physical properties of the bilayer. During stage 2, the concentration of surfactant available within the system surpasses that saturation value and a

characteristic lamellar to micellar phase transition occurs for the lipidic mesophase. This morphological transition produces local lipid-dominant mixed micelles that coexist within the original lamellar bilayer. Stage 3 describes detergent concentrations above the threshold solubilizing concentration in the system, in which the entropically-driven mixing of the previously mentioned lipid-dominant mixed micelles and available, pure detergent micelles leads to smaller detergent-dominant mixed micelles at final equilibrium. This model was generally held to be true until further research efforts complicated this depiction.[7-10] Such results scrutinize this "three-stage model" and its usefulness in advancing biotechnologies, as it ignores the structural and chemical complexities of the involved components. Therefore, it is facile to ask what happens when our system gets more complex?

Another such membrane-perturbing component of focus here is proteinaceous content.[11, 12] Membrane-bound proteins are practically a ubiquitous property of cellular life, as their functionality is wide-reaching from the facilitation of cellular communication to energy conversion.[13, 14] Their topology within cellular membranes is primarily determined by a balance of hydrophobicity and charged amino acids residues within helical segments when inserted into the lamellae.[15] Furthermore, minute chemical and physical aspects of individual amino acids can also impact the protein's membrane packing.[16, 17] There has been a plethora of scientific studies that have examined the activity of these biological molecules, including full proteins, shorter peptides, digested proteins, and singular amino acids, all of which exhibit unique behaviors.[16-21] As such, what previously unappreciated biological systems could exhibit unique membrane-active properties?

To examine these membrane-perturbing substances, I assembled various lamellar mesophases of lipidic components using multiple techniques.[22-24] One such assembly is the myelin figure, a unique class of lyotropic, cylindrical, smectic mesophase that was first reported by Virchow more than 150 years ago.[25, 26] These tubule-like structures originate from the contact of an aqueous solution with a dried mass of nearly insoluble (~10^{-10} M) lipids.[22, 27-30] These interfacial protrusions are composed of thousands of cylindrical, concentric lamellae of lipid bilayers and aqueous spacer channels wrapping an aqueous center.[28, 31, 32] As

such, this mesophase merits itself as an interesting subject of study for the doping of these perturbing substances as each interacting molecule can only approach the externally-available bilayers of the tubule, therefore providing insight into the kinetics of such behaviors in real time.[33] Another multilamellar assembly employed is the multilayer stack, being the layering of lyotropic, lipidic bilayers on top of one another supported by a flat surface.[24, 34] Instead of direct contact with an aqueous solution, vaporous water is used to hydrate a dried mass of lipids into a multilamellar stack from which structural properties can be measured using averaged x-ray diffraction techniques.[35-38] With this, I aimed to internally dope these active substances within the multilamellar mesophase to elucidate holistic depictions of bilayer structural modulation across the entire stack.[35] Last, I employed giant unilamellar vesicles, assembled using known electroformation techniques, as a cell-like structure for the involved perturbing components.[19, 23, 39] These micrometer-sized, spherical mesophases separate their internal components from their external bath due to the selective permeability of the bilayer, therefore presenting a unique ability to experimentally investigate singular active molecules externally or internally.[7, 18, 40] From there, perturbing molecules were introduced within these mesophases and the resulting properties were visualized by various types of microscopy, x-ray diffraction, or atomic force microscopy.

In **Chapter 2**, we introduce our participating components, the focal structural organizations of these lipidic molecules, and microscopy systems with which we performed the proceeding work.

In **Chapter 3**, we investigated the morphogenesis and solubilization of a non-equilibrium lipidic mesophase when exposed to a micelle-forming surfactant. Multilamellar myelin figures were assembled in the presence of a micelle-forming surfactant, and the resulting behaviors were visualized and quantitated in real time. Such experiments allow us to analyze kinetic information of mesophase solubilization as well as suggest a holistic depiction of the thermodynamics of the lipid-surfactant system. We found that myelin figures composed of fluid-phase lipids proceeds through distinct morphological steps that are emblematic of a complex balance of energetic considerations *en route* to solubilization with no detergent concentration dependence while myelin figures composed of heterogeneous domain-forming mixtures did not proceed

along that pathway during solubilization. Therefore, this study foregrounds the relatively unappreciated complexity of lipid-surfactant systems and their thermodynamic interactions.

In **Chapter 4**, we examined the nanoscopic structural impacts of surfactant doping within flat, lipidic, multilamellar membrane stacks. Various molar ratios of lipid to surfactant (lipid:surfactant) were deposited on a supported surface and hydrated by vaporous water, in which the structural properties of the involved lamellae were measured by various analytical techniques. By investigating the nanoscopic properties of lipid-surfactant systems, we can more accurately explain complex amphiphilic systems like the experimental system in **Chapter 3**. We found that an increased amount of surfactant generally disordered the hydrophobic space of a lamellae and shrunk its thickness while trends of the hydrating water layer thickness were highly variable between the surfactants utilized. These results help explain the apparent behaviors and kinetics of the experimental system in **Chapter 3** as well as highlight the need to consider the chemical properties of these doping surfactants when employing them for various biotechnologies.

In **Chapter 5**, we surveyed the membrane-interacting activities of two proteins from the iridocytes of the California market squid (*Doryteuthis opalescens*) with both giant unilamellar vesicles as well as multilamellar myelin figures. Both of these fluid-phase mesophases were exposed to the pH-sensitive proteins reflectin A1 and reflectin C at various concentrations and their resulting behaviors were visualized in real time. An investigation of this protein family is of merit as characterizing the properties of these biological molecules can allow us to develop materials with highly unique reflective properties for usage in other materials. Through these studies, we found that both of the lamellar mesophases exposed to reflectin A1 were destroyed through varying methods: vesicles burst and collapsed while myelin figures had lipidic material removed from its external layers. These results suggest that isolated protein activity does not align with *in vivo* studies, where the complex protein mixture within the cytosol of the iridocytes maintains their light-reflecting functionality while inhibiting the destructive activity of their components, highlighting the delicate evolutionary balance constructed by these squids that needs to be employed for future material development.

In **Chapter 6**, we studied how a complex environmental solution, acting as a simple model for biofilm matrices, impact the behavior and properties of various giant unilamellar vesicles. These electroformed vesicles, with two different compositions, were aliquoted into the bacterial culture media 2-YT and their resulting dynamics were visualized in real time. Such a study can help us begin to suggest how biological material, compartmentalized within lamellar vesicles, can be more efficiently transported within biofilm matrices between bacterial individuals. Here, we found that vesicles coagulated and adhered to one another when exposed to 2-YT, but not other isomolar solutions, while maintaining similar fluidity within their lamellae at the adhered regions. Therefore, through these results, we hypothesize that extracellular vesicles could be packaged as quantized "packets" within biofilm matrices for efficient transportation and delivery.

With these five chapters, we demonstrate a small slice of the multiplicity of dynamics exhibited by various amphiphilic and biological dopants, and we hope to inspire others in examining the microscopic and macroscopic impacts of membrane-perturbing agents.

CHAPTER 2 – Lamellar Mesophase Assembly and Microscopy Instrumentation

2.1. LAMELLAR MESOPHASE SAMPLE PREPARATION AND ASSEMBLY

Phospholipids are highly unique building blocks of microbiology because of their tunable structural variance. This is true due to the chemical and physical properties that dictate their behavior. Such properties include the hydrophobic effect, electrostatics, hydrophobicity, van der Waals' interactions, molecular shape, and molecular packing.[41] Such forces influence the three-dimensional self assembly of these components into various phases, including cubic (C), micellar, hexagonal (H), and inverted hexagonal phases (H_{II}).[41-44] The work presented herein focuses on the lamellar phase (L_α) of these biomimetic amphiphilic materials, a generally ubiquitous structural organization in biological systems. In this phase, molecules align laterally with like neighbors as a semi-permeable bilayer that controls the passage of material between compartments. These structures can either be unilamellar or multilamellar, both of which are present in biological systems.[45-47] In this dissertation, three unique types of lamellar mesophases are formed: giant unilamellar vesicles (GUVs), multilamellar myelin figures, and flat multilamellar stacks of bilayers. All of which assemble in particular conditions which we introduce generally below. Specific procedures and methods in forming these lamellar mesophase are explained in the proceeding chapters.

Beginning with GUVs, these lamellar mesophases were prepared using an already established technique called electroformation.[23] In this procedure, a stock solution of lipidic material is spread on two cleaned, conducting microscope slides and allowed to dry. Then, these dried lipid films are hydrated by an aqueous solution before being sandwiched together. An electrical function generator is connected to this lipidic "sandwich" and an electrical current is applied across the slides where vesicles ~10-100 μm swell and form. Next, we focus on myelins. For these mesophases, we employ an existent technique called directed hydration.[48] First, a stock solution of lipids is deposited on a non-electrically conducting microscope slide and allowed to dry. Another slide is then sandwiched on top of the lipid film before an aqueous solution is aliquoted on the edge of this "sandwich". By capillary action, the aqueous solution

travels in between the slides and contacts the edge of the dried lipids from which the myelin tubules grow outward at their root as they assemble. Last, we introduce the formation of the multilamellar stacks. Instead of a hydration by liquid water, vaporous water is employed to assemble these structures.[24] To begin, a stock solution of lipids is deposited on a non-conducting microscope slide and dried. These lipidic films were then placed into a humidity chamber with a saturated aqueous solution of K_2SO_4 (which elevates the relative humidity of that chamber to 98%), sealed, and equilibrated to an elevated temperature of ~50-55ºC for ≥ 24 hours. Once equilibrated, the sealed chamber is returned to room temperature for another 24 hours. All of these lamellar mesophases can then be visualized by brightfield microscopy or wide-field and confocal fluorescence microscopy (by the addition of a fluorescently-tagged lipid in the employed stock solutions) which we discuss below.

2.2. MICROSCOPY INSTRUMENTATON

Throughout the chapters of this dissertation, we employ three techniques for mesophase imaging and visualization: brightfield microscopy (also known as light microscopy), wide-field fluorescence microscopy, and confocal fluorescence microscopy. All of these techniques capture images and videos of subjects in the size range of ~1 μm-1 mm. Subjects are observed by either the contrast of light originating from the attenuation of white light (brightfield) or the fluorescent excitation and emission of specific wavelengths of visible light by fluorophores (wide-field and confocal fluorescence).[49] Each method utilized here possesses a unique level of complexity and functionality, which we elucidate below.

Brightfield microcopy is the simplest of the three techniques (**Figure 2.1**). Here, white light is emitted by a simple light source and passed through focusing mirrors before reaching the sample. When passing through the subject, some of the light is absorbed, scattered, or deflected by the composition of the subject. The remaining light then passes through an objective lens to resolve and magnify the consequential image before reaching the final destination of a detector (whether it be the observer's eyes or a camera

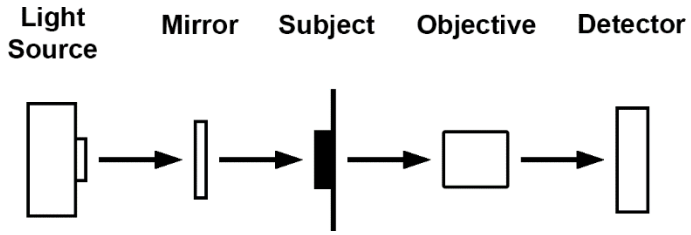

Figure 2.1. Simplified Depiction of a Brightfield Microscopy Instrument. A simplified depiction of a brightfield microscopy instrument, including the light source of white light, the focusing mirror, the subject, the objective lens, and the detector.

connected to a computer). This microscopy technique is the simplest as it solely depicts the subject as a black contrast from the white background signal.

Wide-field and confocal fluorescence microscopies are innately more complicated as these methods interact with specific molecules within the subject instead of simply providing a contrast image (**Figure 2.2**). For wide-field microscopy, a light source (such as a mercury-vapor lamp or light-emitting diode) produces a signal of light with all of the wavelengths of visible light. Of these wavelengths, one is selected as the excitation wavelength by passing through a set of filters found within a filter cube before heading to the microscope's objective lens.[49] This excitation light then interacts with the molecules of the subject, of which one (known as the fluorophore) readily absorbs this wavelength of light.[50] The fluorophore molecule uses the energy of this light to promote an electron to a higher, quantized energy level before releasing this energy and demoing the electron's energy state.[51] The emitted or emission light then passes back through the same objective lens (with its dichroic mirror) for magnification and resolving before reaching the detector.[49] In this method, the entire vertical column of the subject is illuminated by the excitation light, so the emission light also originates from the entire vertical column.[49] This includes signal from parts of the subject that are not in focus with the objective and the detector, making the overall image the observer sees much blurrier.[52] Therefore, confocal fluorescence microscopy is employed as the method only interacts with certain points or vertical slices of the subject (**Figure 2.2b**).[52] Here, the excitation light passes through a small hole where only light at that focal plane passes through.[49] This means that excitation light which would interact with out-of-focus areas of the subject do not pass through the hole to the subject. Once the excitation light interacts with the subject, the emitted light then passes back through the objective lens to the detector as per usual. These techniques are vital to the investigation of the dynamics of the aforementioned lamellar mesophases, especially when imaging these systems in real-time.

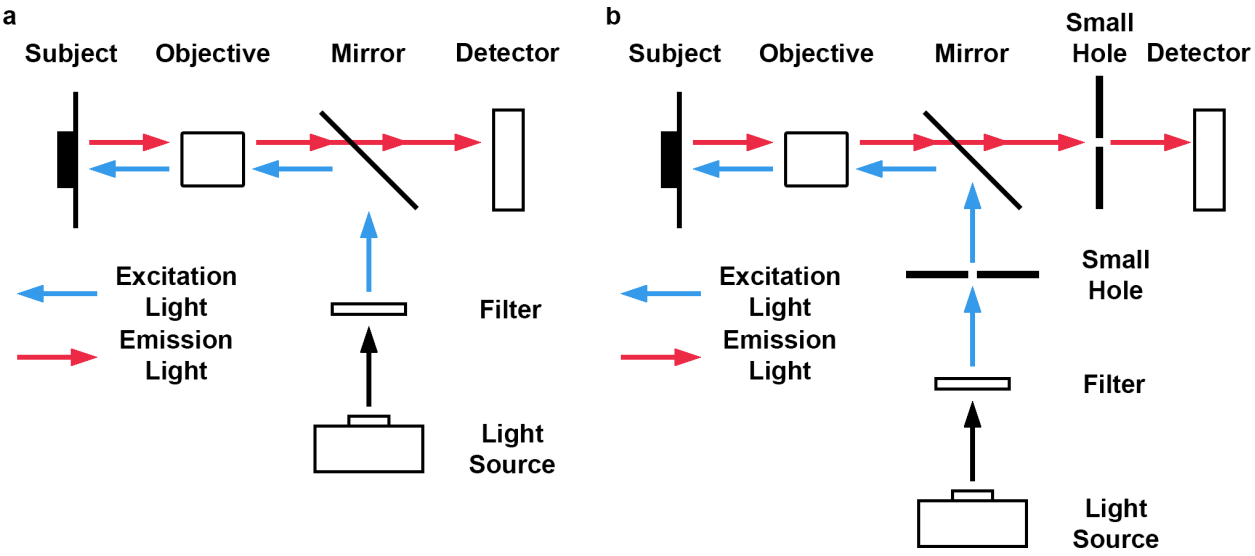

Figure 2.2. Simplified Depiction of Wide-Field and Confocal Fluorescence Microscopy Instruments. (a) A simplified depiction of a wide-field microscopy instrument, including the light source of visible light, the filter for the excitation light, a mirror to direct the excitation light, the objective lens, the subject, the emission light, and the detector. (b) A simplified depiction of a confocal microscopy instrument, including the light source of visible light, the filter for the excitation light, the small holes for light at the focal plane, a mirror to direct the excitation light, the objective lens, the subject, the emission light, and the detector.

CHAPTER 3 - Surfactant-Mediated Solubilization of Myelin Figures: A Multi-Step Morphological Cascade

3.1. ABSTRACT

Lamellar mesophases of insoluble lipids are readily solubilized by the micellar mesophases of soluble surfactants. This simple process underscores a broad array of biochemical methodologies, including purification, reconstitution, and crystallization of membrane proteins, as well as the isolation of detergent-resistant membrane fractions. Although much is now known about the thermodynamic driving forces of membrane solubilization, the kinetic pathways by which the surfactant alters vesicular mesophases are only beginning to be appreciated. Little is known about how these interactions affect the solubilization of more complex, multilamellar mesophases. Here, we investigate how a common zwitterionic detergent affects the solubilization of a smectic, multilamellar, cylindrical mesophase of lipids, called the myelin figure. Our results reveal that myelin solubilization occurs in a multi-step manner producing a well-defined sequence of morphologically distinct intermediates *en route* to complete solubilization. The kinetic processes producing these intermediates include (1) coiling, which encompasses the formation, propagation, and tightening of extended helices; (2) thinning, which reflects the unbinding of lamellae in the smectic stacks; and (3) detachment or retraction, which either dissociates the myelinic protrusion from the source lipid mass or returns the myelinic protrusion to the source lipid mass – all in transit toward complete solubilization. These occasionally overlapping steps are most pronounced in single-lipid component myelins, while compositionally-graded multi-component myelins inhibit the coiling step and detach more frequently. Taken together, the appearance of these intermediates during the solubilization of myelins suggests a complex free energy landscape characterizing myelin solubilization populated with metastable, morphological inter-mediates correlated to locally minimized changes in energy dependent upon the mesophase's composition. This then predicts the accessibility of structurally distinct, kinetic intermediates – such as loose- and tight-coiled helices, peeled myelins, retracted tubes, and detached protrusions – before reaching the stable ground state corresponding to a dissolved suspension of mixed surfactant-lipid micelles.

3.2. INTRODUCTION

Molecular components of biological membranes – phospholipids, glycolipids, sterols, and membrane proteins – are insoluble amphiphiles.[41, 43] Taken alone, they spontaneously aggregate in aqueous media, forming smectic liquid-crystalline, lamellar mesophases, or insoluble precipitates.[53, 54] Surfactants and detergents, by contrast, are soluble amphiphiles.[41] Above a threshold concentration – the critical micelle concentration (CMC) – they form micelles in water.[43, 54] When these two hydrophobically-assembled mesophases – one comprising insoluble lipids and the other soluble surfactants – interact, complex dynamics ensue.[44] In a typical case, the surfactant from the micellar phase invades the lipidic mesophase, thereby driving it far outside thermal equilibrium.[5, 6, 55] The subsequent evolution of this non-equilibrium state, as it progresses toward a new equilibrium, is often complicated: It is dominated by the rates and manners by which the surfactant dopes in the parent mesophase and how it perturbs, evolves, and modifies the initial morphology.[7, 56-59]

This is perhaps best exemplified by the common biochemical process of detergent-mediated membrane solubilization.[5, 6] Detergents (or surfactants), used extensively to extract, purify, and reconstitute membrane proteins as well as isolate detergent-resistant lipid rafts, destabilize the bilayer motif, ultimately leading to complete solubilization of the target membrane.[60-66] A sequence of complex and reversible phase transformations accompany membrane solubilization, the qualitative phenomenology of which is captured elegantly by the so-called three-stage model. First proposed by Helenius and Simons in 1975, the consensus model distinguishes three stages of equilibration or morphological evolution.[6] Stage 1 represents a state characterized by an effective concentration of detergents in a membrane (or detergent-lipid ratio, R_e) below a threshold saturation value ($R_e < R_e^{sat}$). Here, detergent binds and partitions into the bilayer. The resulting diversification of mass, area, composition, tension, and curvature alters the physical properties of the membrane. In stage 2, when the membrane is saturated with the detergent ($R_e^{sat} < R_e < R_e^{sol}$), a characteristic lamellar to micellar phase transition produces large, lipid-saturated mixed micelles that coexist in equilibrium with the residual lamellar bilayer. Beyond solubilizing detergent concentrations

($R_e \geq R_e^{sol}$), which represents stage 3, the lamellar phase is fully solubilized. Here, the entropic mixing between large, lipid-detergent mixed micelles and small, pure detergent micelles stabilizes smaller detergent-saturated mixed micelles at equilibrium. These three stages, which describe shifting equilibria corresponding to increasing surfactant concentrations, are thought to map onto the temporal steps characterizing the morphological evolution that ensues when membranes encounter detergents at solubilizing concentrations (above the critical micelle concentration or > CMC).[5, 67]

Conspicuously absent in this picture – which treats different aggregates (as well as monomers) as distinct thermodynamic pseudo-phases in equilibrium with one another – are the dynamics and specificities of interactions between the surfactant and the lipidic mesophase.[7, 68] This is perhaps best illustrated by a recent study examining the dynamics of interactions between surfactants and giant unilamellar vesicles (GUVs) in real-time.[7] The investigation documents a striking diversity of kinetic pathways that characterize the membranous dissolution dynamics. Some of the characteristic pathways that the study identifies involve continuous shrinking, inside-out topological inversions, site-directed openings, and rapid bursting of GUVs. Each of these pathways is a consequence of how surfactants intercalate into and organize within the membrane; none are predicted by the equilibrium three-stage model.[7] Other more recent investigations confirm these findings and further reveal a plethora of additional, qualitatively different phase and morphological transformations that accompany membrane solubilization when lipid compositions are altered, and other classes of amphiphilic surfactants are used.[8-10, 69, 70]

These nuances of the surfactant-mesophase interactions, namely the specificities of how surfactants partition within the membrane and the types of deformations they elicit, become exacerbated when the solubilizing morphology is a structurally complex mesophase. Consider, for example, a multilamellar, smectic phase of lipids. In these hierarchically organized mesophases, only the outermost lamellae are initially available for interaction with added surfactants. Thus, the solubilization must proceed in a multi-step cascade with each subsequent lamellae interacting with the micelles of the surfactant as well as mixed micelles of varying compositions produced by its interactions with preceding lamellae. Furthermore,

morphological changes, which follow when surfactant enters the lamellar mesophases, are constrained by the interlamellar interactions (i.e., Helfrich interactions) holding the smectic layers together.[71] Finally, any compositional differences, such as those that may exist in the layers of the parent mesophase, must also alter the kinetics and thermodynamics of solubilization. How these structural complexities influence the abilities of surfactants to solubilize complex mesophases is largely unknown.

Motivated by these considerations, we investigate here the surfactant-induced solubilization of a novel class of lyotropic, cylindrical, smectic mesophase called the myelin figure. First reported by Virchow more than 150 years ago, these mesophases appear as a dense tangle of tubules when water encounters a dried mass of nearly insoluble (~10^{-10} M) lipids.[22, 27-30] These finger-like protrusions – which are tens of micrometers wide and extend to hundreds of micrometers in length – nest thousands of cylindrically-stacked, alternating lamellae of lipid bilayers and aqueous channels wrapping a narrow (~100 nm), central, aqueous core.[28, 31, 32] Their 1D smectic order is stabilized by the inter-lamellar Helfrich repulsion, which separates the neighboring bilayers by nanometer-scale aqueous channels and inhibits molecular exchanges between individual lamellae.[71] Previous research efforts have explored the perturbations of the myelinic organization with amphiphilic, aqueous-soluble dopants, finding that the tubes morphologically transition from linear tubes to coiled helices.[72] While valuable for our understanding of myelin behavior, these molecular dopants did not undertake any solubilizing action.

In our study, the solubilizing detergent of choice was the synthetic zwitterionic surfactant Zwittergent 3-12 (*n*-dodecyl-*N,N*-dimethyl-3-ammonio-1-propanesulfonate or DDAPS, CMC = 2-4 mM), which is used widely in the isolation of membrane proteins.[73-76] Both single-lipid component and multi-component myelins were studied. Single component myelins were prepared using fluid phase 1-palmitoyl-2-oleoyl-sn-glycero-3-phosphocholine (POPC), and multi-component myelins comprised an equimolar mixture of POPC, cholesterol (CHOL), and egg-sphingomyelin (SM). In both cases, either the dried lipid mass was hydrated using the detergent-laden aqueous solution, or the pre-formed myelins were exposed to

solutions of DDAPS. The resulting myelinization and morphological changes were monitored in real-time using brightfield, confocal fluorescence, and wide-field fluorescence microscopies.

The results reported here establish that the DDAPS-mediated dissolution of myelins is neither direct nor independent of myelin molecular composition. *En route* to complete solubilization, the chemically homogeneous single component myelins composed of fluid phase POPC lipids undergo a sequence of well-defined morphological changes before undergoing complete solubilization. These steps include coiling, which encompasses the formation, propagation, and tightening of extended helices; thinning, reflecting the unbinding of smectic lamellae; and retraction. In sharp contrast, the dissolution of multi-component myelins consisting of phase-separating ternary mixtures of POPC, CHOL, and SM – which are known to form compositionally-graded myelins – exhibit little or no propensity for coiling, but undergo gradual thinning as well as retraction or detachment.[77] The appearance of these intermediates during the dissolution of myelins suggests a complex free energy landscape of myelin solubilization, possibly parallel with the one predicted by the Ostwald's rule of stages.[78]

This work is published in *Langmuir* and reproduced here as it is open access.

3.3. RESULTS AND DISCUSSION

Preliminary characterization of the hydration of the single component mother lipid reservoir (or "lipid cake") by pure water was carried out to confirm myelinization. Upon contacting water, the boundaries of dried POPC cakes roughen instantaneously. A dense tangle of well-defined myelin figures projecting into the aqueous phase decorates the lipid-water interface confirming the essential phenomenology.

Although individual myelins meander and grow sinuously, the average length – the distance (ℓ) between the front extending into the water and the root at the base of the lipid cake – for a collection of myelins in single experiments showed a characteristic growth pattern: On average, myelins grew with a square root of time $\left(\ell \propto t^{1/2}\right)$ dependence (**Figure 3.1**). This growth pattern is fully consistent with previous observations, and lends further credence to the preponderance of diffusive mechanisms in

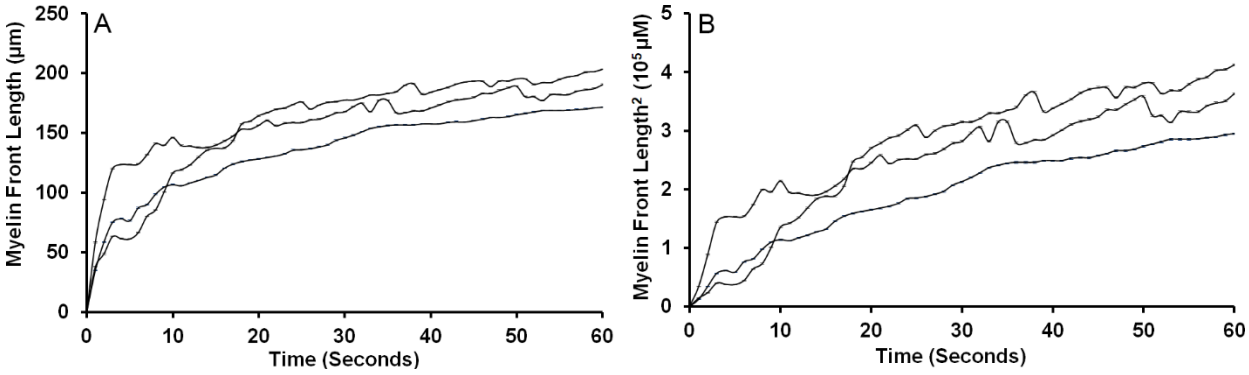

Figure 3.1. Myelin Front Growth over Time. (A) Myelin front length versus time and (B) myelin front length^2 versus time were plotted for the growth regime of the myelin front for three trials. All lengths were measured from the myelinic protrusions' root to their tips in a linear manner perpendicular to the lipid cake. Error bars are the resolution of the image (0.4 µm) for (A) and propagated from the resolution for (B).

determining myelinic growth: a combination of (1) collective diffusion of lipid aggregates in response to the hydration gradient at the lipid-water interface and (2) lateral diffusion of lipids within the bilayer.[29, 79-81] Quantifying the growth ($\ell^2 = k\,t + c$), we find that the apparent diffusion constant, k, to be 3.00 x 10^{-6} ± 0.02 cm^2/s (n = 3) during the first 60 s of growth, which is comparable to the range of values reported previously (4.3 x 10^{-6} cm^2/s for a hen-egg lipid mixture, 2.0 x 10^{-6} cm^2/s for an unspecified phosphatidylcholine lipid, 7.0 x 10^{-7} cm^2/s for the amphiphile $C_{12}E_3$, 2.2 x 10^{-6} cm^2/s for the amphiphile $C_{12}E_6$, and 1.0 x 10^{-6} cm^2/s for egg-PC at room temperature**)**.[79, 80, 82-84] Although infrequent, we occasionally observed that the linearly protruding myelins coiled spontaneously, typically within the first few minutes (2-3 min) of hydration. Examining the behaviors of a large number of myelins (n = 253), we find that this spontaneous higher-order organization is both stochastic and rare, measuring at 0.4% of all myelins examined.

Substituting the hydrating solution with one containing DDAPS at concentrations above its CMC (2-4 mM), we find a dramatic shift. Although the lipid-water interface roughened and tubular myelins projected into the aqueous phase at comparable growth rates as above, the protrusions abandoned their linear morphologies. Instead, a statistically significant proportion of myelins, far surpassing the 0.4% above (see below), exhibited extended coiling – a higher-order organization breaking the chiral symmetry of the stacked myelin membranes. In sharp contrast, the giant vesicle, an exemplary, single component, unilamellar mesophase, did not express such unique morphological developments in its solubilization. The vesicular organization catastrophically ruptured when exposed to comparable concentrations of DDAPS.

Real-time visualization of this gross shape remodeling (**Figure 3.2**) reveals a rapid propagation of an initial stochastically-generated, localized twist along the length of the myelin, often producing extended

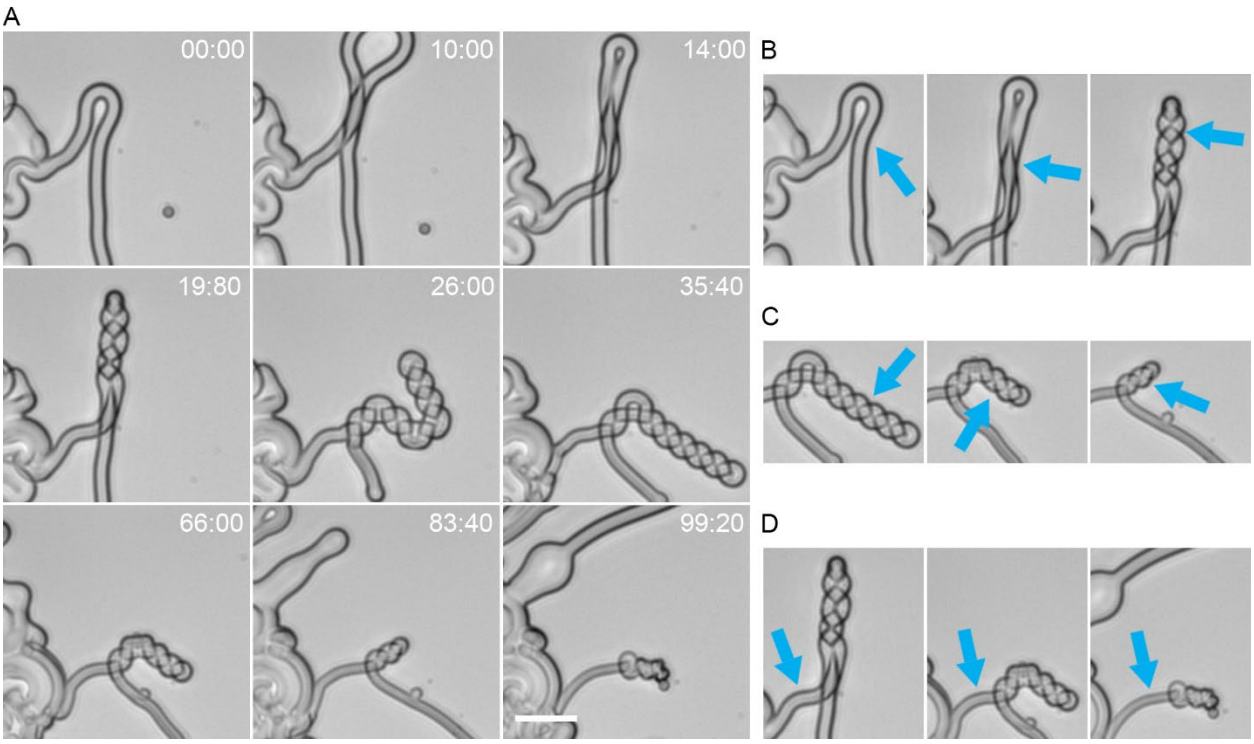

Figure 3.2. Detergent-Mediated Shape Remodeling of Single Component Myelin Figures. (A) A selection of time-lapse brightfield microscopy images of a representative myelin figure consisting of 100 mol% POPC lipids coiling and dissolving in an aqueous solution containing 120 mM DDAPS. The example reveals a single, flexible myelin looping, twisting, and coiling to form an extended helix propagating away from the tip of the loop. With time, the myelin thins, uncoils, and retracts back to the mother lipid mass. Timestamp, sec:centisec; Scale bar, 20 μm. (B-D): Cropped images highlight the overlapping development of the (B) loose coiled state, (C) tight coiled state, and (D) peeled state marked by arrows.

helices spanning the length of myelin figures themselves (> 50 μm). The twisting motif forming the helices was also substantially diverse: Both self-coiling (single strands) and, less commonly, cross-coiling of neighboring myelins producing double helices were evident, often in single samples. The former, self-coiling, propagated by the generation of new pitches from a twisting deformation of a hairpin loop connecting the two arms and the latter, cross-coiling, occurring through helical coiling of separate myelins around one another. Moreover, there appeared to be little or no discernible preference for the sense of winding direction (handedness): Roughly 45% were left-handed, 42% were right-handed, and 13% had both left- and right-handed sections on a single pair of strands (n = 60).

Performing myelinization experiments using aqueous solutions with systematically varied DDAPS concentrations (1 mM, 5 mM, 15 mM, 30 mM, 60 mM, 90 mM, and 120 mM), we found that the surfactant concentration had a profound effect on the prevalence of this higher-order organization (**Figure 3.3**). At low surfactant concentrations – in the vicinity of the CMC value of DDAPS (2-4 mM) – the myelins formed were essentially indistinguishable from those produced in pure water. In other words, they were largely unperturbed by the presence of the surfactant and displayed a clear tendency to form linear myelins extending several times their diameters. At and above 15 mM surfactant concentration, however, noticeably higher fractions of myelins displayed the appearance of the coiling motif. Quantifying the myelin landscape, we find that the number fractions of coiled myelins grew with the surfactant concentration: 3.57 ± 1.55% (n = 5) at 15mM to 22.14 ± 4.20% (n = 5) at 120 mM (**Figure 3.3)**.

The formation of a coil necessitates the consolidation of the length of the tube, effectively reducing the extension of the myelinic protrusion. This could be achieved by shortening the linearly extending tube or consolidating additional growth. Our observations provide evidence for each of the two mechanisms. Our results reveal that the surfactant-induced coiling can recruit existing portions of the essentially linear sections of a myelin, iron-out any available wrinkles of sinuous sections of a myelin (**Figure 3.4**), or access additional tube length made available by the growing of a myelin. Over time, helical myelins exhibited a

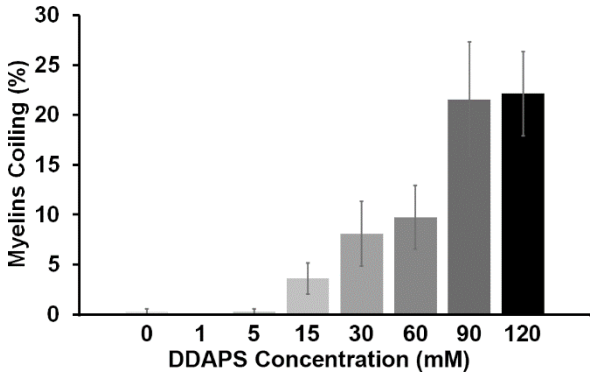

Figure 3.3. Detergent Concentration Dependent Coiling of Myelin Figures. With increasing DDAPS concentration (0-120 mM) in the hydrating solution, the proportion of individual POPC myelins undergoing a coiling transition within the first 5 min of hydration increases monotonically. The error bars represent the standard error of means (n = 5).

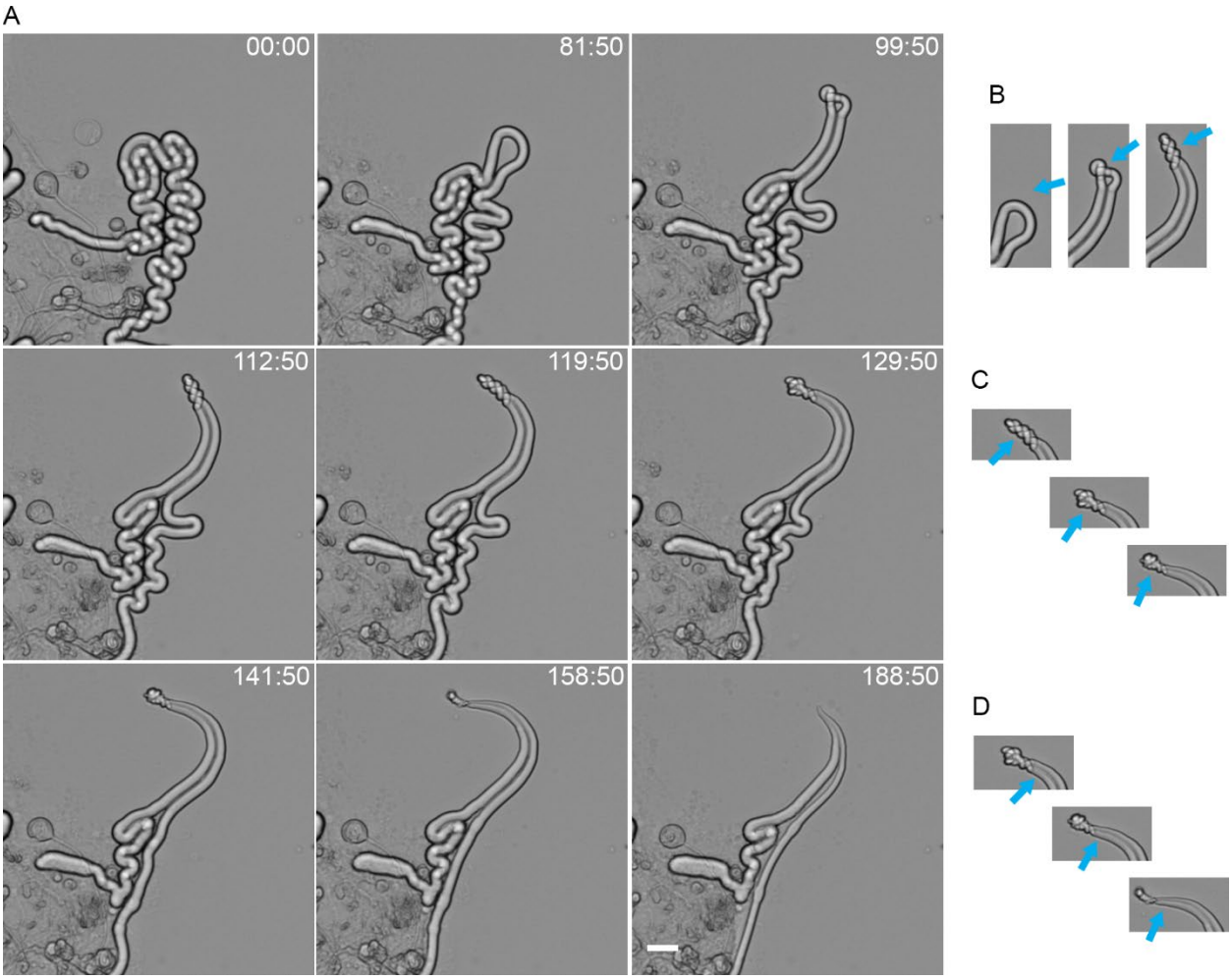

Figure 3.4. Proposed Intermediates of Surfactant-Mediated Myelin Solubilization. (A) A time-lapse depiction of a myelin composed of 100 mol% POPC hydrated with deionized water then exposed to an equal volume of 120 mM DDAPS after 5 minutes. The myelin exhibits "ironing out wrinkles" to recruit the needed length to coil. Time stamp, sec:centisec; Scale bar, 20 μm. (B-D): The cropped images highlight the concurrent development of the (B) loose coiled state, (C) tight coiled state, and (D) peeled state intermediates with colored arrows pointing out relevant areas of behavior.

consistent pattern of tightening. While the diameters of uncoiled segments of participating myelins remained unchanged, the helices contracted: The pitch length – the length of a complete helical turn, measured along the helical axis – decreased and the width – the largest size perpendicular to the central axis – shrank (**Figure 3.5**). This gradual tightening of the helical coil, which increases the contact surface at the cost of bending the tube, is consistent with the notion that surface adhesion plays a role.[85] Notably, as the helices tightened, the pitch angle – defined as the arctangent of the ratio of the tube diameter to the pitch length – remained essentially unchanged, hovering around an average of ~39° (**Figure 3.6**). This then suggests that the two processes, the tightening of the helical segments and the thinning of the tubes, occur concurrently.

Visualizing the fate of the coiled myelins over the long term, we find that the coiled state is not permanent. Overtime ($t \geq 5$ min), helical myelins solubilized into the surrounding bath. This unraveling is gradual: The coiled myelins thin, uncoil, retract, and dissolve (**Figure 3.4**). The observation of solubilization is confirmed by monitoring the base of a helix: Linear myelin tubes at the root of the helix thinned or peeled as their external bilayers underwent delamination reminiscent of a lamellar unbinding transition (**Figure 3.4D and 3.5**).[86]

Real-time visual analysis of the base of the helices reveals a rate independent of the surfactant concentration (**Figure 3.5E**). Moreover, we find that the average solubilization kinetics yields a rate constant of $k \sim 0.01$ μm/s for the solubilization process. Assuming the myelin tube to be a smooth cylinder and using the approximations of each bilayer's thickness to be 5 nm and each phospholipid's lateral area to be 0.65 nm^2, we can calculate an approximate rate of material loss from the myelin figures.[87] Using this estimated rate constant, a singular myelin tube is losing roughly two bilayers per unit length per second or $\sim 9.75 \times 10^{-18} \frac{mol\ POPC}{(\text{sec})(\mu m\ length)}$ or $\sim 5.87 \times 10^{7} \frac{POPC\ molecules}{(\text{sec})(\mu m\ length)}$ because of its interactions with DDAPS in solution (**Figure 3.7**). These intermediate stages did not always appear as well-separated sequential events. In several instances, at the time resolution of 0.2 seconds per frame in our measurements, certain states seemed to be skipped, whereas others appeared to proceed concurrently (**Figures 3.4 and 3.7**).

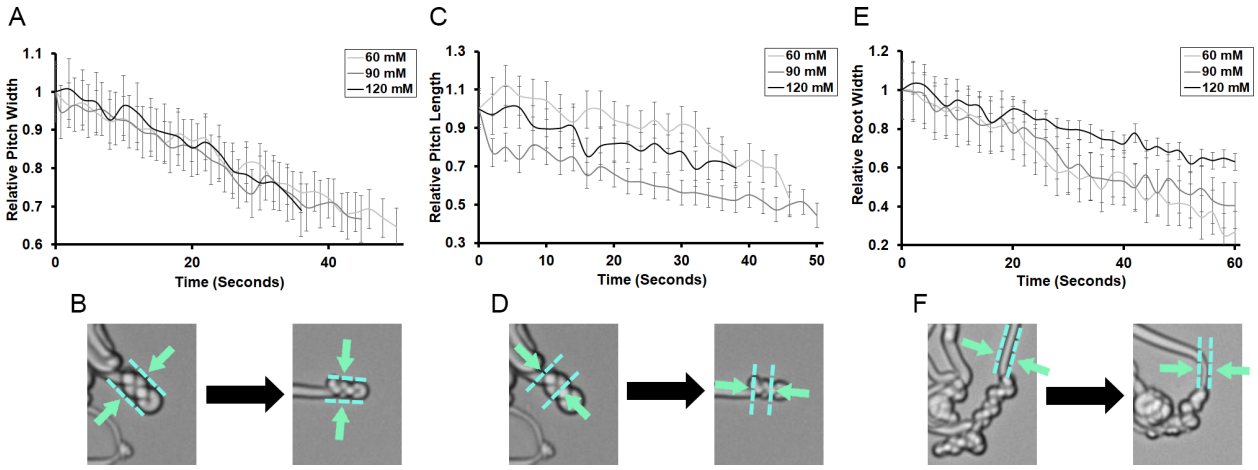

Figure 3.5. Coil Tightening and Myelin Thinning Stages during DDAPS-Mediated Solubilization of Single Component Myelin Figures. (A) The relative width (in comparison to the starting observed width) of the helical morphology was measured in real-time at various concentrations of DDAPS. Error bars, standard error based on image resolution, ±0.4 μm. (B) The helical width of myelin was measured as depicted by the distance between the dashed lines of the selected images. (C) The relative length of the helical pitches was measured versus time in a similar comparative manner to (A). (D) The helical pitch length of myelin was measured as depicted by the distance between the dashed lines of the selected images. (E) The relative width of the roots of the helical morphologies were measured over time to investigate the dissolution rate of the available bilayers. (F) The helical root width of myelin was measured as depicted by the distance between the dashed lines of the selected images.

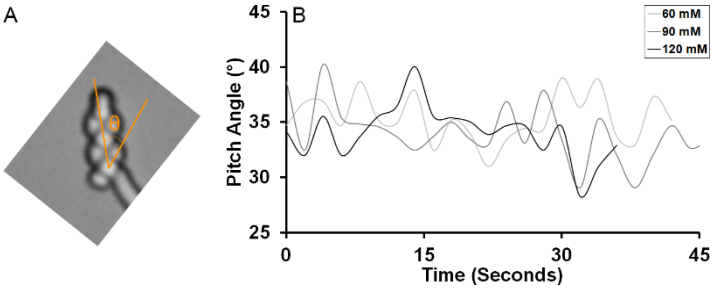

Figure 3.6. Definition and Analysis of the Pitch Angle of Myelin Helices. (A) The pitch angle (θ) of a myelin helix was measured for selected figures like the provided visual depiction. The specific angle is found between the long axis of a myelin helix's half-pitch and a line overlaid on the central lumen of the coiling tube as accurately as possible given the resolution of the microscope. (B) The pitch angle of myelins coiling into helices was plotted over time due to DDAPS exposure at various concentrations.

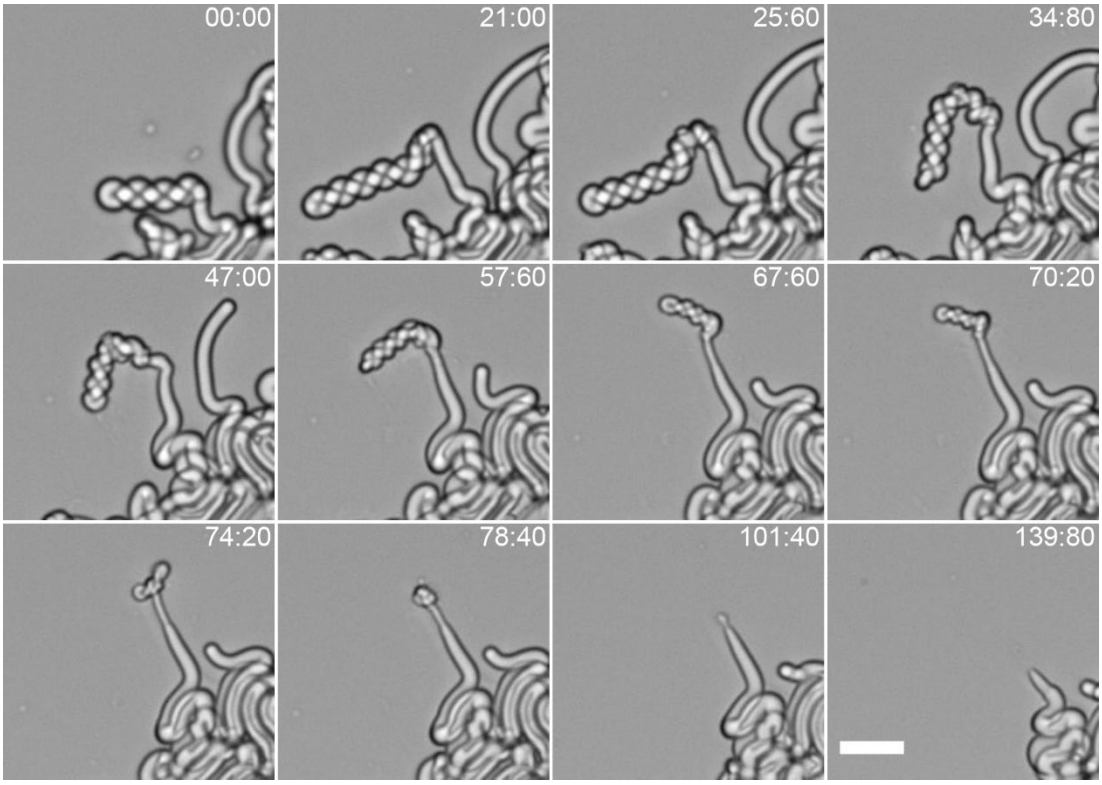

A

Figure 3.7. The Lifetime of a Myelin Figure Expressing Proposed Intermediates. A myelin composed of 100 mol% POPC expresses the loose coiled state, tight coiled state, and peeling state concurrently before dissolving into the surrounding solution when exposed to 120 mM DDAPS in the time-lapse depiction. A video of this myelin's lifetime is available as Video S9. Time stamp, sec:centisec; Scale bar, 20 μm.

A unique feature of the multilamellar myelinic organization is that it can stabilize gradients in chemical composition between lamellae.[77] In multi-component lipid mixtures, where different lipids hydrate and fluidize differently, the myelinic organization preserves the record of differences in their hydration kinetics. In a recent study, we have shown that this can give rise to long-lived spatial patterns of chemical composition. Specifically, we found that when lipid cakes containing phase-separating mixtures of unsaturated lipid, cholesterol, and sphingomyelin are hydrated, interlamellar molecular segregation ensues. The resulting myelins display continuous, interlamellar radial gradients of concentrations of cholesterol, sphingomyelin, and the unsaturated lipid. The latter fluid phase lipids concentrate in the inner lamellae and the former lipids, cholesterol and sphingomyelin, accumulate in the outer lamellae at the highest concentrations. An immediate consequence of this compositional gradient is that the outermost, cholesterol-enriched lamellae are stiffer and more resistant to solubilization by detergent.[5, 67, 88, 89] How would such graded organizations influence the abilities of surfactants to drive solubilization? Would it help shield the buried fluid phase lamellae within a protective coat of cholesterol-rich outer layers?

Myelin figures were assembled using a 1:1:1 molar ratio of POPC, SM, and CHOL with 0.1 mol% Rho B-DOPE and 0.3 mol% NBD-DPPE dopants (respectively) as fluorescent dyes, which labeled the liquid-disordered (L_d) and liquid-ordered (L_o) phases respectively. Upon hydration with an aqueous solution, the L_o phase preferentially partitioned to the external bilayers and the L_d phase preferred the internal core of the myelin figures, confirming previous work.[77]

Hydration with aqueous solutions containing DDAPS (90 mM) triggered the solubilization of these multi-component myelins. During the ~10 minutes following hydration, multi-component myelins displayed a continuous thinning. Of the many instances of myelin dynamics observed (n = 518), none coiled, and no helices were observed over tens of minutes of observation. Quantifying the thinning dynamics by monitoring the changes in the fluorescence of the two phase-sensitive lipid probes, Rho B-DOPE and NBD-DPPE, yielded further insights (**Figure 3.8**). When integrated and averaged, both channels displayed a thinning rate of $k \sim 0.04$, four times larger than that during the solubilization of the single

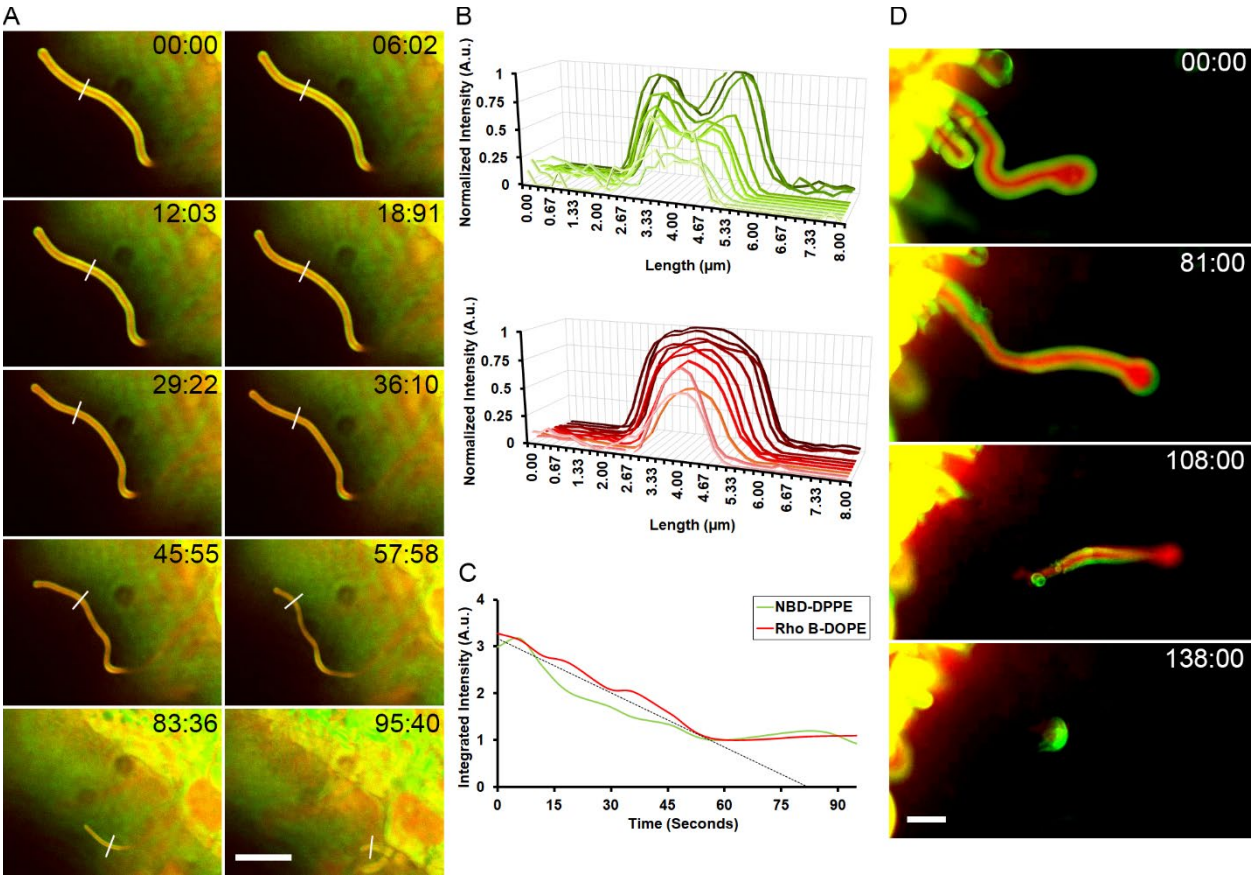

Figure 3.8. Solubilization and Detachment of Compositionally-Graded Multi-Component Myelins. (A) A time-lapse depiction of a multi-component myelin composed of a 1:1:1 ratio of POPC, SM, and CHOL with 0.1 mol% and 0.3 mol% Rho B-DOPE and NBD-DPPE dopants (respectively) showing thinning and retraction. The white line on each frame depicts the line along which fluorescence intensity was measured for (B). Time stamp, sec:centisec; Scale bar, 20 μm. (B) The fluorescence intensity of both the NBD-DPPE (Green) and Rho B-DOPE (Red) channels of the multi-component myelin figure were measured along the length of the manually drawn normal line and normalized to their average background intensity. Normalized fluorescence plots for both channels were measured throughout time and plotted together where the time points are 0 seconds (darkest shade), 6.02 seconds, 12.03 seconds, 18.91 seconds, 29.22 seconds, 36.10 seconds, 45.55 seconds, 57.58 seconds, 83.36 seconds, and 95.40 seconds (lightest shade). (C) The normalized intensity was integrated to elucidate the area under the curve at each time point for each channel. Integrated intensity data was plotted versus time for each channel. A trendline of the initial thinning is also plotted with a slope of $k \sim 0.04$. (D) A time-lapse depiction of a multi-component myelin composed of a 1:1:1 ratio of POPC, SM, and CHOL with 0.1 mol% and 0.3 mol% Rho B-DOPE and NBD-DPPE dopants (respectively) detaching from the lipid cake and solubilizing as a free-floating myelin. Time stamp, sec:centisec; Scale bar, 20 μm.

component POPC myelins. Using the same approximations as above, the myelin tube sheds roughly eight bilayers per unit length per second or ~2.39x10^{-16} $\frac{mol\ POPC}{(\text{sec})(\mu m\ length)}$ or ~1.44x10^{8} $\frac{POPC\ molecules}{(\text{sec})(\mu m\ length)}$ during the thinning stage. Monitoring the changes in the integrated fluorescence due to the two phase-sensitive dyes, we observe that the two – the NBD-DPPE channel pertaining to the external L_o phase and the Rho B-DOPE channel pertaining to the internal L_d – decay at comparable rates. This difference can be straightforwardly understood by considering the phase dependence of surfactant partitioning and accessibility. Although the L_d phase is less abundant in the exposed leaflets, the greater partitioning of DDAPS within that phase might account for increased local destabilization thereby yielding comparable apparent rates of delamination of the L_d and L_o phase components during thinning (**Figure 3.8C**).

The DDAPS-mediated thinning of multi-component myelins was accompanied by another notable difference. A sub-population of thinning myelin figures shortened in length, ultimately retracting to the mother lipid mass. An equally significant proportion of myelins displayed a remarkable topological transition, detaching the myelinic protrusions from the mother lipid mass and producing freely suspended tubules (**Figure 3.8D**). These isolated, discrete myelins are not long-lived: over time, their tubular geometry is abandoned, producing rounded mesophases *en route* to dissolving entirely. This general trend in surfactant-mediated morphological transitions was fully reproducible for different compositions of the ternary myelins. Changing the 1:1:1 lipid ratio to a 3:1:1 and 1:2:2 ratio of POPC, SM, and CHOL revealed qualitatively comparable solubilization dynamics.

Given the differentiated morphogenesis observed above, several factors must be considered to appreciate the kinetic and thermodynamic determinants of these unusual solubilization trajectories. First, the coiling of myelin tubes. Previous research efforts have deduced a number of mechanistic explanations for coiling depending on their observational contexts. First, helical coils of myelin tubes were hypothesized to originate from an adhesion force between the surface bilayers. This could manifest as either an electrostatic interaction between involved, negatively-charged headgroup lipids and dissolved cations or intermembrane interactions between neutrally-charged lipids.[48, 85, 90] Using some empirical estimates, the

attractive force outcompeted the energetic cost of bending bilayers in the tube. A confounding study exhibited that adhesion does not solely induce coiling, moreover, the presence of external, amphiphilic dopants could. Using the biopolymer dextran grafted with sixteen carbon aliphatic chains, myelin tubes began to coil more frequently.[72, 91] Here, the polymer becomes an integral part of the myelin composition, doping each lamellae of the multilamellar myelin architecture. These studies propose that the coiling of myelins arises because of the local polymer concentration, which induces spontaneous curvature, and the mobility of the polymer along the length of the myelin, which reduces the bending energy penalty. Last, an independent theoretical study identifies that a coiling instability may also emerge when non-externally perturbed myelin's lamellae are compressed, such as under osmotic stress, which acts to reduce the equilibrium distance between the lamellar membranes.[92] In these cases, the curvature energy penalty, which resists the decrease in radii of membrane lamellae, competes with the relaxation to the new equilibrium. This then sets the stage for a buckling instability – akin to a Helfrich-Hurault instability – promoting coiling.[93, 94] In the present case, the relevant, confounding hypotheses can be assimilated for a holistic understanding of myelin behavior. We begin by eliciting the interactions between the doped surfactant and the myelinic lamellae. They are determined by the kinetics and thermodynamics of (1) how DDPAS spatially distributes within the bilayer, distributing homogeneously or accumulating locally in mesophase domains; (2) how it partitions between the two leaflets of each bilayer; and (3) how the intercalation of the surfactant influences the flip-flop translocation of lipids comprising the myelin ultimately producing mixed micelles. Previous studies establish that the intercalation of DDAPS in the exposed, outermost bilayer is rapid. The partitioning coefficients of DDAPS, K_p (mol l^{-1} in the membrane /mol l^{-1} in the aqueous phase) have been reported to range from thousands to tens of thousands.[95] However, the subsequent distribution of DDAPS between the leaflets of the exposed bilayer is considerably limited, presumably because of DDAPS's zwitterionic head-group and positive molecular curvature.[95] Together, these behaviors promote the localized accumulation of DDAPS in outer leaflets of the exposed bilayer, asymmetrically expanding the bilayer, producing detergent-enriched domains, and generating curvature stress.[5] To relieve this elastic stress, single bilayers bend to assume the corresponding local spontaneous curvature, as predicted by the

so-called bilayer-couple hypothesis.[96] The bending of single leaflets, however, is strongly opposed by the interleaflet interactions and the interlamellar Helfrich interactions.[71] A slow morphological consequence of this tug-of-war between competing influences of local spontaneous curvature and interlamellar interactions – deduced previously in theoretical formulations based on equilibrium considerations – is the breaking of the stack's chiral symmetry leading to coiling.[72, 91, 92] These competing forces, as well as other factors like the mass transfer of both pure DDAPS micelles to and mixed micelles from the parent mesophase, dictate the kinetics of this process and explain why solubilization rate appears to be independent of concentration.[97]

In contrast, how is the coiling step suppressed when utilizing compositionally-graded, multi-component myelins? Our results robustly demonstrate that the myelins produced by the mixtures of POPC, cholesterol, and sphingomyelin exhibit little or no propensity for coiling. As shown previously, and confirmed here, individual lamellae of myelins produced by these lipid mixtures are not compositionally identical to the bulk stoichiometry.[77] Instead, the molecules segregate differentially: The outermost lamellae are more enriched in cholesterol and sphingomyelin (L_o phase components), and the L_d phase forming POPC populates the innermost layers. This radial gradient in composition creates gradients in membrane fluidity and bending rigidities, with the outermost layers exhibiting the highest bending rigidity and the lowest lateral fluidity. In these structurally dense L_o phases, surfactants and detergents have weak solubility and may promote intralayer domain formation by segregating cholesterol and sphingomyelin from the detergent and any fluid phase POPC lipids.[98-101] Based on these considerations, we propose that the reduced surfactant partitioning within the L_o phase lipids and the differential membrane bending properties might explain the observed suppression of the coiling instability in cholesterol-rich myelin layers.

Next, what dictates the thinning regime? Both single component and multi-component myelin figures exhibit a monotonic decrease in myelin widths. In the single component myelins, this thinning regime usually follows the tightening regime, but we also observed overlaps between the two. This overlap manifests as the coil tightening at fixed pitch angles, which require the two processes – a decrease in pitch size (tightening) and a decrease in a tube's diameter (thinning) – to become fully congruent with one

another. In the case of multi-component myelins, where the coiling stage is suppressed, the thinning occurs continuously, often extending and overlapping with the next stage characterized by myelin retraction or detachment. In both experimental cases, the observed thinning requires delamination of lamellae from the cylindrical, smectic, multilamellar myelins, a process consistent with the previously studied phenomenon of complete unbinding transitions in which thermal fluctuations and local short-range interactions can drive unbinding of lamellae in smectic phases.[86, 102, 103] Although our experiments do not resolve the kinetic pathways by which thinning proceeds, the partitioning characteristics of DDAPS suggests a plausible route: The asymmetric accumulation of DDAPS in the outer leaflet of the exposed myelin bilayer (see above) and the increased flip-flop of lipids then sets the stage for lamellae delamination via the so-called micellar mechanism.[68] Here, the lipids are extracted from the surfactant-doped outer leaflet of the exposed bilayer of myelins via interactions with the detergent micelles. The resulting depletion of lipids exposes the non-polar interstitial space of a bilayer which prompts increased rates of lipid flip-flopping for energetic balance, driving further dissolution of the exposed bilayer. With each successive delamination, new bilayers become exposed to the detergent micelles driving a stepwise cascade of myelin thinning, such as what was observed.

Last, why does the system choose to retract or detach? As a simultaneously elastic and fluid structure, myelin figures are dynamic and complicated. As deduced previously, myelin growth can be determined by its hydration potential, therefore, we elongate this rationality and propose that myelin retract (or reversibly grow) depending on each individual tube's hydration properties.[22] Contrarily, the striking topological transition characterizing the detachment of multi-component myelins and the appearance of free-floating myelins is a novel observation. For the myelinic protrusions to detach from the source lipid mass, an energy-intensive topological transition – a pinch-off event – in the vicinity of the myelinic root is needed. At present, we do not fully understand the mechanisms driving this localized fission. But it is tempting to speculate that the roots of the myelins – which can be expected to be at lower steady-state tension in growing myelins (out of equilibrium) because of the frictional drag induced by the water flow –

provide localized spatial and compositional niches for surfactant intercalation creating conditions for rupture.[104, 105] This proposition, however, is unverified.

With these complexities elucidated, how do they couple to form this solubilization pathway? *En route* to dissolution of single component myelin, we observed the development of a well-defined sequence of kinetic intermediates: (1) loose-coiled helices, upon surfactant intercalation and spontaneous curvature generation in the exposed bilayer; (2) maximally-coiled tight helices, which increases membrane contact and adhesion; and (3) peeled myelins, reflecting stepwise delamination of external lamellae. Their appearance suggests a plausible pathway for the solubilization of myelin figures. We propose that the pathway to the solubilization of myelins is marked by multiple free energy steps, each with its own activation energy barrier and each providing a corresponding lowering of the system's free energy (**Figure 3.9**).[106] First ($\Delta G_1^{\ddagger}$), DDAPS intercalates within the exposed bilayers of the myelin figures, reorganizing the lipid packing within the hydrophobic interior, producing local spontaneous curvature, and bending the bilayers of the myelin tube. These processes are antagonized by the interleaflet interactions, interlamellar Helfrich interactions, and elastic bending strain considerations of the tube, leading to the loose-coiled step.[71, 93] Next ($\Delta G_2^{\ddagger}$), the subsequent insertion of higher amounts of DDAPS more intensely bends the bilayers, further aggravating the factors mentioned for $\Delta G_1^{\ddagger}$ and increasing the activation energy of the step to access the tightened stage. In possible contrast, the increased contact line of tightened myelin helices presents the opportunity for a beneficial interaction energy between the surface bilayers.[90] Also, each intermediate is stabilized by their increasing magnitude of spontaneous curvature.[93, 107] Upon reaching solubilizing circumstances ($\Delta G_3^{\ddagger}$), we anticipate the highest value of activation energy to reach the peeling step. In this step, mixed micelles begin leaving the mother mesophase and, as mother lipid material is lost, the hydrophobic core becomes exposed to external aqueous conditions and the zwitterionic lipids flip flop to relieve this thermodynamic consequence.[108] These interactions, as well as considerations in elastic bending strain and Helfrich interactions seen in the previous steps, maximize the activation energy.[93, 107] In return, entropy will be maximized by the mixing of the participating amphiphiles between phases as well

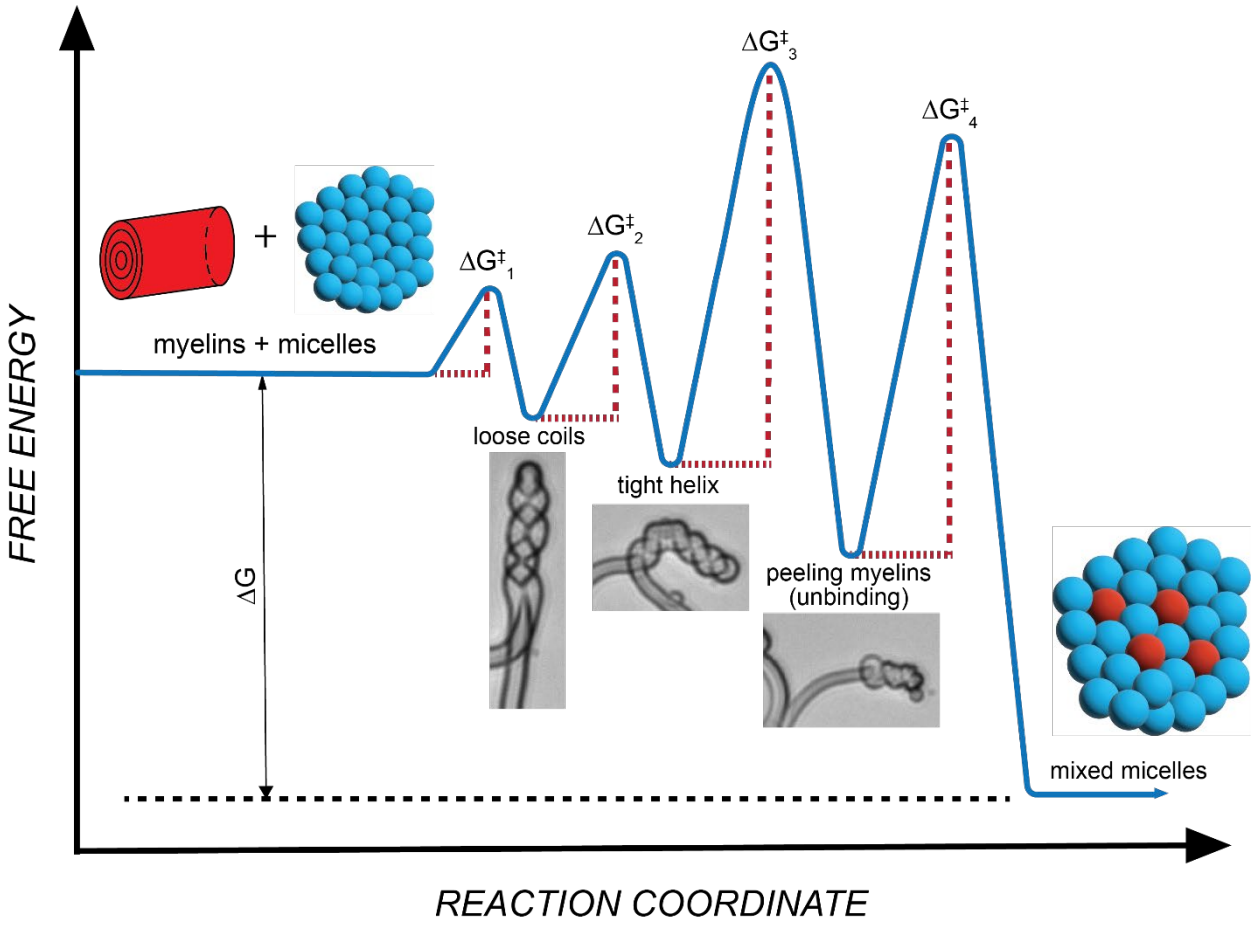

Figure 3.9. Free Energy Landscape of Detergent-Mediated Myelin Solubilization. A cartoon representation of the kinetic pathway of detergent-mediated myelin solubilization. The pathway is dotted with a sequence of metastable intermediates being loose coils, tight helices, and peeled myelins, in the order of decreasing free energy and increasing activation energy barriers until reaching the final state of a micellar suspension characterizing equilibrium (adapted from Ref. 106). ΔG represents the overall driving force and individual $\Delta G^{\ddagger}$ are local activation energy barriers.

as the translational degrees of freedom gained when the mixed micelles are removed from the lamellar phase.[107] Last ($\Delta G_4^{\ddagger}$), we anticipate that the energetic procession of peeling myelins to an isotropic solution of mixed micelles will be smaller in value than $\Delta G_3^{\ddagger}$. While incurring the same processes, the quantitative magnitude of the participating interactions will decrease as less mother lipid material is left. Overall (ΔG), this process occurs due to the complex balance of spontaneous curvature, interlamellar Helfrich interactions, elastic bending strain, the hydrophobic effect, possible adhesive interactions, available thermal energy, and entropy maximization of the involved components.[107] Thus, it appears that the observed multi-stage process of myelin solubilization loosely parallels the Ostwald's rule of stages and the Stranski-Totomanow conjecture, traditionally employed for the crystallization of molecules instead of the behavior of liquid-crystalline materials, where a phase transition occurs when its proceeds through the smallest loss of free energy to its immediate precursor by the smallest available activation energy barrier.[78, 109]

3.4. CONCLUSION

The solubilization of the chemically homogeneous, single component myelins (such as those obtained by the hydration of fluid phase POPC lipids) by a common zwitterionic detergent (DDAPS) begins with the appearance of an axial twist, which propagates to produce transient, but long-lived, extended helices. Over time, these helices *tighten*, increasing membrane line contact; *thin*, gradually shedding lamellae; and *retract*, re-mixing with the source lipid mass while solubilizing into the aqueous phase. In contrast, multi-component myelin figures (composed of an equimolar mixture of POPC, SM, and CHOL) did not exhibit any observable helical morphogenesis, but thinned and *retracted* or *detached*, producing free-floating myelins. While distinct, these metastable steps were observed to occasionally happen concurrently; measuring the pitch angle of certain coiled myelin figures elicited the possibility of tubes to have congruent tightening and thinning with an average angle of 39°. During this solubilization process, a multitude of factors dictated the kinetics, including the mass transfer of both pure DDAPS micelles to and mixed micelles from the parent mesophase, the partitioning of DDAPS molecules into bilayers from the

aqueous phase, the intercalation properties of DDAPS within a bilayer, and the energetically-intensive bending of bilayers within the myelin figure. The combination of these factors explains why solubilization rates appear to be independent of concentration.

These metastable states are segregated due to their thermodynamic considerations, including spontaneous curvature, the elastic bending of membrane bilayers, and the interlamellar Helfrich interactions. The partitioning and asymmetric accumulation of DDAPS in the outer leaflet of the exposed myelin bilayer induces a heterogeneous spontaneous curvature and desire for the populated bilayer to bend. The morphological change competes with the interlamellar Helfrich interactions holding the bilayers together, with tighter curvatures (or deviations from unperturbed bilayers) increasing the energetic cost. Upon reaching solubilizing concentrations within the bilayer, the system enacts the micellar mechanism where mixed micelles leave the bilayer organization and remove parent lipid material, inducing an increased rate of flip-flopping lipids to minimize exposure to the external aqueous phase. As parent lipid material is lost, lamellae can delaminate, solubilize, and expose the internal bilayers to the new pure DDAPS micelles. This occurs iteratively until the myelin figure has been fully destroyed or retracted. The solubilization of myelin by this proposed mechanism of energetic considerations possibly parallels the procedures of the Ostwald's rule of stages.

While similarly exposed to pure DDAPS micelles, multi-component myelins incur alternate mechanisms of morphological destruction. The helical morphogenesis is shunted in favor of thinning, and retraction or detachment. We propose that the reduced surfactant partitioning within the eternal L_o phase lipids and the differential membrane properties might explain the observed suppression of the coiling instability in cholesterol-rich myelin layers.

Our findings that the pathways of surfactant-mediated solubilization of multilamellar lipid mesophases are dotted with long-lived or metastable intermediates of well-defined morphologies – such as those that may be predicted by extending the Ostwald's rule of stages – may open interesting new possibilities. They suggest new pathways for deriving novel classes of transiently-organized and surfactant-

programmable mesostructures and self-assemblies outside thermal equilibrium.[110, 111] They might prove valuable in extending the tool kit for *in-meso* crystallogenesis – a rapidly evolving field for crystallizing membrane proteins within lipid environments.[61, 112, 113]

3.5. MATERIALS AND METHODS

Materials. 1-Palmitoyl-2-oleoyl-*sn*-glycero-3-phosphocholine (POPC), 1,2-dioleoyl-*sn*-glycero-3-phosphoethanolamine-N-(lissamine rhodamine B sulfonyl) (ammonium salt) (Rho B-DOPE), 1,2-dipalmitoyl-*sn*-glycero-3-phosphoethanolamine-*N*-(7-nitro-2-1,3-benzoxadiazol-4-yl) (ammonium salt) (NBD-DPPE), egg-sphingomyelin (SM), and cholesterol (CHOL) were purchased from Avanti Polar Lipids (Alabaster, Al). *n*-Dodecyl-*N,N*-dimethyl-3-ammonio-1-propanesulfonate (DDAPS) was acquired from MilliporeSigma (Burlington, MA). Chloroform, methanol, ethanol (denatured), and sucrose were purchased from Sigma-Aldrich (St. Louis, MO). Base and cover boro-silicate microscope slides were obtained from Corning (Corning, NY). Nitrogen gas was acquired from Praxair (Danburt, CT). Indium tin oxide (ITO) coated glass slides (resistance 4-30 Ω) were purchased from Delta Technologies (Loveland, CO). 8-well plastic bottom plates were obtained from MatTek Corp. (Ashland, MA). All chemicals were used without further purification.

Myelin Preparation and Experimentation. Myelin figures were prepared by adapting a previously-reported procedure of hydrating a dried mass of phospholipid molecules between two microscope slides.[22] Two separate stock solutions were prepared at a concentration of 25 mg/ml in 9:1 (v/v) chloroform to methanol, (1) 100% POPC and (2) an equimolar (1:1:1) ratio of POPC, SM, and CHOL with 0.3% NBD-DPPE and 0.1% Rho B-DOPE. Microscope slides were cleaned by sonication for 5 minutes in a bath of ethanol, dipping in chloroform for 1 second, and drying with nitrogen gas and desiccation. Small droplets (4 μL) of stock solution were placed on cleaned cover slides and the solution was allowed to dry in the atmosphere until a dried mass remained (~15 minutes). Droplets containing fluorescent labels were covered

with aluminum foil to protect them from light while drying. Coated cover slides and clean base slides were then pressed together into a lipid cake for 10 seconds using a Mettler Toledo (Greifensee, Switzerland) presser. Cakes were either used immediately or stored under a house vacuum and protected from prolonged exposure to ambient light. All cakes were used within a week of preparation. Lipid cakes were mounted onto the appropriate microscopy instrument, and a sharp, unobstructed edge of the dried mass was found (**Figure 3.10**). 40 μL of an aqueous solution was then pipetted onto the edge of the sandwich, and the solution moved into the gap by advection with the glass. Upon contact with the dried mass, tubules of myelin figures grew outwardly into the surrounding area. The lipid cake could be hydrated with deionized water, DDAPS at varying concentrations, or a two-step process of 40 μL of deionized water then 40 μL of 120 mM DDAPS after 5 minutes. All experiments were carried out at room temperature, which is above the gel-fluid phase transition temperature of almost all of the lipids used. SM, possessing a transition temperature of 37°C, posed no issues during myelin formation once assembled with aqueous solutions.[77] To confirm the surface nature of the surfactant's interactions, myelin was assembled using the two-step process (see above). Five minutes was chosen for step 2 because tubes seldomly intake the external aqueous solution and grow at that time. Thus, the incoming DDAPS (in the micellar phase) is limited to interacting with the surface bilayers of the myelins. Within 5-10 minutes, myelins began to coil qualitatively comparable to the previous exposure methods (**Figure 3.4**).

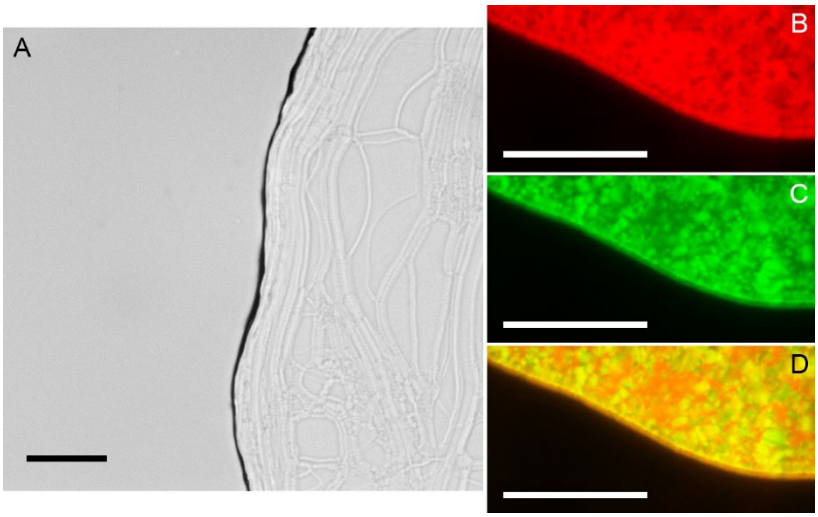

Figure 3.10. Satisfactory "Lipid Cakes". (A) Exemplary lipid cakes from 100 mol% POPC possess clean, almost linear edges when visualized by brightfield microscopy. (B-D) An exemplary lipid cake from a 1:1:1 ratio of POPC, SM, and CHOL with 0.1 mol% and 0.3 mol% Rho B-DOPE and NBD-DPPE dopants (respectively) possesses clean edges for all color channels when visualized by confocal fluorescence microscopy with the corresponding (B) red, (C) green, and (D) merged channels. Scale bars, 50 μm.

Giant Unilamellar Vesicle Preparation and Experimentation. Giant unilamellar vesicles were prepared in alignment with previously-established techniques using electroformation.[39] Two separate stock solutions were prepared at a concentration of 2 mg/ml in chloroform, (1) 100% POPC and (2) an equimolar (1:1:1) ratio of POPC, SM, and CHOL with 3% NBD-DPPE and 1% Rho B-DOPE dopants. 15 μL of the desired stock solution was spread on the conductive side of two ITO-coated microscope slides and dried for at least two hours under house vacuum. Once dried, a rubber 'O' ring (Ace Hardware, Davis, CA) was glued to one slide around the lipid film using vacuum grease (Dow Corning, Midland, MI) and about 1 mL of a 10 mM sucrose solution was added to the cavity. The chamber was then sealed with the other conductive slide to be water-tight with no air bubbles inside. With a function generator, a 4 Vpp AC sine-wave current was applied across both slides at 10 Hz for 1.5 hours. Afterwards, the current was switched to a 4 Vpp square-wave current at 2 Hz for 1.5 hours. Throughout current application, slides were covered with aluminum foil to minimize light exposure. Slides with lipid films of stock solution (2) were heated to 45°C on a hot plate while slides with lipid films of stock solution (1) were kept at room temperature during current application. Once finished, the sealed system was disassembled, and the solution of vesicles was transferred to a separate vial. The giant vesicles were then stored at 4°C for two days before use. 8-well plates were mounted on the appropriate microscopy instrument and 200 μL of the desired DDAPS solution (1 mM, 15 mM, or 120 mM) was added to a well. Giant vesicles were added to the solution at the bottom of the sample chamber, and the resulting dynamics were visualized.

Brightfield Microscopy. Brightfield microscopy measurements were performed using a Nikon Eclipse TE2000S inverted fluorescence microscope (Technical Instruments, Burlingame, CA) equipped with a Roper Cool Snap CCD camera (Technical Instruments, Burlingame, CA). Videos were taken using a Plan Fluor 20X (NA, 0.25) objective (Nikon, Japan).

Spinning Disk Confocal Fluorescence Microscopy. Spinning disk confocal fluorescence microscopy measurements were performed using an Intelligent Imaging Innovations Marianas Digital Microscopy Workstation (3i Denver, CO) fitted with a CSU-X1 spinning disk head (Yokogawa Musashino-sh, Tokyo, Japan) and a Quantem512SC EMCCD camera (Photometrics, Tuscon, AZ). Fluorescence micrographs were obtained using a Zeiss Plan-Fluor 63x (NA 1.4) oil immersion objective (Carl Zeiss, Oberkochen, Germany).

Wide-field Fluorescence Microscopy. Wide-field fluorescence microscopy images of myelin figures were acquired using a Carl Zeiss Axio Observer Z1, fitted with an EC Plan-Neofluar 63x/1.25 oil objective (Carl Zeiss, Oberkochen, Germany), and equipped with Zeiss set 10 (Ex: 450-490; Em: 515-565) and Zeiss set 31 (Ex: 550-570; Em: 590-650), and HXP 210 C mercury metal halide lamp (Carl Zeiss, Oberkochen, Germany). Wide-field fluorescence microscopy measurements of giant vesicles were performed using a Nikon Eclipse TE2000S inverted fluorescence microscope (Technical Instruments, Burlingame, CA) equipped with a Roper Cool Snap CCD camera (Technical Instruments, Burlingame, CA) and Hg lamp as a light source. Videos were taken using a Plan Fluor 20X (NA, 0.25) air objective (Nikon, Japan) and filter cubes to filter absorption and emission of the source and camera.

Analysis of Myelin. All images and videos were analyzed using the ImageJ software package. Helical morphogenesis, degradation rates, widths, diffusion coefficients, and handedness were computed by manual measurements or calculations.

3.6. FUNDING AND COLLABORATORS

This work is supported by a grant from the National Science Foundation (DMR-2104123) and the contributions of James C. S. Ho are supported by the Singapore Centre for Life Science & Engineering (SCELSE). The 3i Marianas spinning disk confocal fluorescence instrument used in these studies was

purchased using a NIH Shared Instrumentation Grant (1S10RR024543-01). I thank the Department of Molecular and Cellular Biology Light Microscopy Imaging Facility, which is a UC Davis Campus Core Research Facility, for the use of this microscope. I am grateful to my collaborator Dr. James C. S. Ho for his support of the above work.

CHAPTER 4 - Surfactant-Mediated Structural Modulations to Planar, Amphiphilic Multilamellar Stacks

4.1. ABSTRACT

The hydrophobic effect, a ubiquitous process in biology, is a primary thermodynamic driver of amphiphilic lipid membrane self-assembly. The consequences of such energetic considerations lead to the formation of unique morphologies, including two highly important classes of lamellar and micellar mesophases. The interactions between these two types of structures, and their involved components, have garnered significant interest because of their importance in key biochemical technologies related to the isolation, purification, and reconstitution of membrane proteins. This work investigates the structural organization of mixtures of the lamellar-forming phospholipid 1-palmitoyl-2-oleoyl-*sn*-glycero-3-phosphocholine (POPC) and two zwitterionic micelle-forming surfactants, being *n*-dodecyl-*N,N*-dimethyl-3-ammonio-1-propanesulfonate (Zwittergent 3-12 or DDAPS) and 1-oleoyl-2-hydroxy-*sn*-glycero-3-phosphocholine (O-Lyso-PC), when assembled by water vapor hydration with x-ray diffraction measurements, brightfield optical microscopy, wide-field fluorescence microscopy, and atomic force microscopy. The results reveal that multilamellar mesophases of these mixtures can be assembled across a wide range of POPC to surfactant (POPC:surfactant) concentration ratios, including ratios far surpassing the classical detergent-saturation limit of POPC bilayers, without significant morphological disruptions to the lamellar motif. The mixed mesophases generally decreased in lamellar spacing (D) and headgroup-to-headgroup distance (D_{hh}) with a higher concentration of the doped surfactant, but trends in water layer thickness (D_w) between each bilayer in the stack are highly variable. Further structural characteristics including mesophase topography, bilayer thickness, and lamellar rupture force were revealed by atomic force microscopy (AFM), exhibiting homogeneous multilamellar stacks with no significant physical differences with changes in surfactant concentration within the mesophases. Taken together, the outcomes present the assembly of unanticipated and highly unique mixed mesophases with varied structural trends from the involved surfactant and the lipidic com-ponents. Modulations in their structural properties can be

attributed to the surfactant's chemical specificity in relation to POPC, like the headgroup hydration and the hydrophobic chain tail mismatch. Taken together, our results illustrate how specific chemical complexities of surfactant-lipid interactions can alter morphologies of mixed mesophases and thereby alter the kinetic pathways by which surfactants dissolve lipid mesophases in bulk aqueous solutions.

4.2. INTRODUCTION

The hydrophobic interaction – the water-induced attraction between non-polar molecules (or parts thereof) – is a primary driving force for the spontaneous self-assembly of amphiphilic lipids in water.[44] Together with the molecular packing characteristics, this hydrophobic effect gives rise to a rich phase behavior stabilizing a variety of well-ordered lipid-based mesophases in water. Some common examples include lamellar (L_α), cubic (C), hexagonal (H), and inverted hexagonal phases (H_{II}).[42, 114, 115] In this phase space, the specific morphology adopted by a given lipid amphiphile is determined by a number of factors, including temperature, pressure, molecular structure and shape, membrane elasticity, and concentration.[93]

Unlike these water-insoluble lipids, many amphiphiles – such as detergents and soaps – are water-soluble. Below a threshold concentration, termed the critical micelle concentration (CMC), these surface-active agent molecules (or surfactants) coat interfacial surfaces and lower the surface tension, including gas, liquid, and solid interfaces.[5, 116] Above the CMC, surfactants organize into discrete spherical and cylindrical micellar mesostructures, which disperse in the bulk aqueous environment as a colloidal solution.[41, 43, 117-119] The interactions between these micelle-forming surfactants and the equilibrated mesophases of insoluble lipids have been a subject of long-standing interest.[5] This is because these interactions form the basis of many important technologies for the extraction, purification, crystallization, and reconstitution of membrane proteins, one of the most important classes of biomolecules targeted by prescription drugs..[61, 120, 121]

A significant body of previous research has led to generalized model of surfactant-membrane interactions. *En route* to dissolution, a series of complex and reversible phase transformations from lipidic

lamellar organizations to lipid-saturated mixed micelles to detergent-saturated mixed micelles when excess detergent is present in bulk aqueous solutions occurs.[6] This mechanism is termed the three-stage model, first proposed by Helenius and Simons in 1975.[6] The model pairs the above morphological changes to three different stages of local thermodynamic equilibration.

However, the thermodynamic equilibrium picture above does not fully describe the conditions in which surfactants and membranes interact where kinetics considerations dominate.[7, 68] A significant body of experimental and computational research on membrane-surfactant interactions suggests a more complex picture, which drives the surfactant-induced solubilization of the lipidic lamellar mesophases.[67, 122] Particularly, Nomura *et.* al. examined the dynamics of interactions between surfactants and giant unilamellar vesicles (GUVs) in real-time documenting a variety of kinetic pathways that characterize the dissolution dynamics. These pathways were dependent on the physical properties of the membrane and the partitioning behaviors of the surfactant used.[7] Extending these studies to the dissolution of different morphologies, a class of lipidic multilamellar cylindrical mesophases termed myelin figures, we found further evidence for how surfactant partitioning can affect the morphological evolution and the ultimate dissolution of the lamellar phase.[33] Taken together, these observations support the notion that a thorough understanding of how surfactants partition within a membrane's bilayers and the consequential deformations of the lipidic lamellar phase is needed to achieve a more complete understanding of surfactant-membrane behavior.

Here, we investigate the interactions and organization of bilayer-forming water-insoluble phospholipid, 1-palmitoyl-2-oleoyl-*sn*-glycero-3-phosphocholine (POPC) and a water-soluble, micelle-forming zwitterionic surfactant, Zwittergent 3-12 (*n*-dodecyl-*N,N*-dimethyl-3-ammonio-1-propanesulfonate or DDAPS) (**Figure 4.1**). Concurrently, we studied the dynamics of another micelle-forming zwitterionic surfactant 1-oleoyl-2-hydroxy-*sn*-glycero-3-phosphocholine (O-Lyso-PC) with the same procedures for comparison. In both cases, planar films of POPC to surfactant (POPC:surfactant) mixtures, between 100:1

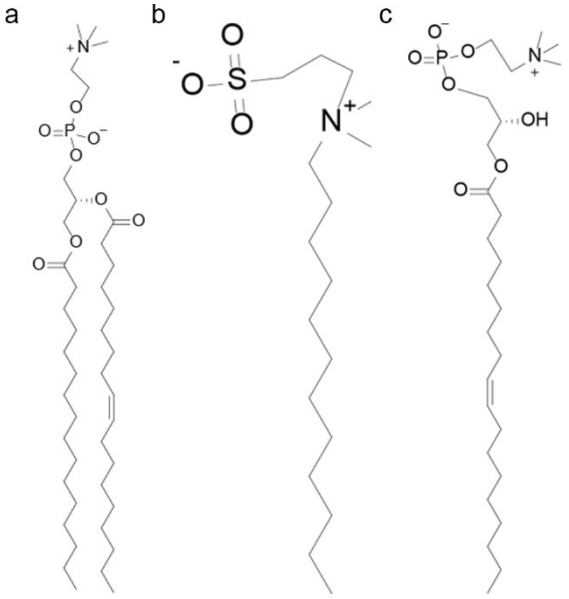

Figure 4.1. Chemical Structure of the Experimental Amphiphiles POPC, DDAPS, and O-Lyso-PC. The chemical structure of (a) 1-palmitoyl-2-oleoyl-*sn*-glycero-3-phosphocholine (POPC), (b) *n*-dodecyl-*N,N*-dimethyl-3-ammonio-1-propanesulfonate (DDAPS), and (c) 1-oleoyl-2-hydroxy-*sn*-glycero-3-phosphocholine (O-Lyso-PC).

and 1:4 molar ratios, deposited on solid supports are hydrated by water vapor in sealed humidity chambers containing saturated K_2SO_4 solutions (having a relative humidity, or RH, of 98%). The resulting morphologies are subsequently characterized using a combination of x-ray diffraction (XRD), brightfield optical microscopy, wide-field fluorescence microscopy, and atomic force microscopy (AFM).

Results presented here establish that the POPC:surfactant mixtures co-assemble into well-ordered multilamellar mesophases for a wide range of molar ratios. While previous work shows that surfactants to form interfacial monolayers on solid supports, the assembly and preservation of the lamellar motif across the multilamellar stack with surfactant-dominated compositions is highly unique.[116, 123] Furthermore, we found that the partitioning of the surfactant within the lamellar lipid phase did not induce large-scale lipid-surfactant phase separation nor distorted the lamellar phase to any noticeable degree. Instead, the two surfactants introduced subtle structural perturbations to the lamellar phase while preserving the multilamellar stack. With increasing DDAPS concentration, the lamellar spacing (D) of POPC mesophases decreases monotonically. Decreases in D were driven by corresponding gradual decreases in both the headgroup-to-headgroup spacing (D_{hh}) and the thickness of the interlamellar water layer (D_w) – consistent with the surfactant-mediated "drying" and disordering of the hydrophobic space of the lamellar phase.[5] By contrast, an increased concentration of O-Lyso-PC drives a surprising structural transition. Below a 1:2 molar ratio of POPC:O-Lyso-PC, the lamellar spacing of the POPC mesophases remain essentially unchanged. This apparent structural "stability" arises despite surfactant-induced disordering (as accompanied by a corresponding decrease in the headgroup-to-headgroup distance) of the lamellar phase. Curiously, the surfactant-induced disordering, which implies thinning, is counteracted and compensated by a corresponding increase in the interlamellar water layer thickness. However, at a 1:2 molar ratio of POPC:O-Lyso-PC, both the water layer thickness and the headgroup distance decreases. Taken together, our results illustrate how the chemical complexities of surfactant-membrane interactions alter the structure of mixed mesophases, and ultimately determine the kinetic pathways by which surfactants dissolve lamellar lipid mesophases.

This work is published in the *Journal of Physical Chemistry B* and reproduced here as it is open access.

4.3. RESULTS AND DISCUSSION

We begin by characterizing the lamellar mesophase consisting of just the single phospholipid, POPC, at room temperature using XRD. A detailed analysis of the data obtained (see "Materials And Methods" section above) yielded the values for the three lamellar periodicities: a lamellar spacing (D) of 51.8 Å, a headgroup-to-headgroup distance (D_{hh}) of 39.4 Å, and a water layer thickness (D_w) of 12.4 Å. It is important to note that D includes the water layer between the lipid bilayers. These values are in statistical agreements with those reported previously.[124-127]

To enable visualization of the lamellar mesophase by wide-field fluorescence microscopy, we doped a POPC stock solution with 1 mol% Rho B-DOPE. Visualizing the lamellar mesophase prepared from this doped solution revealed a homogeneous fluorescence intensity after normalization to the background and maximum value (94 ± 2.7% of max fluorescence intensity) across a line plot on the surface, consistent with a uniform, lamellar organization (**Figure 4.2**).

Next, we examined lamellar mesophases produced from mixtures of POPC and the surfactant DDAPS with systematically varied lipid:surfactant molar ratios (100:1, 40:1, 20:1, 5:1, 5:2, 2:1, 1:1, 2:3, 1:2, 2:5, 1:3, 20:61, and 1:4) using XRD measurements. *First*, we found that the lamellar motif was remarkably preserved across the broad concentration range. This is evident in the existence of single, well-defined lamellar repeat distances found in the XRD measurements (**Figure 4.3 and 4.4**). The preservation of the lamellar order in the mixed mesophase is particularly surprising since there is a significant mismatch

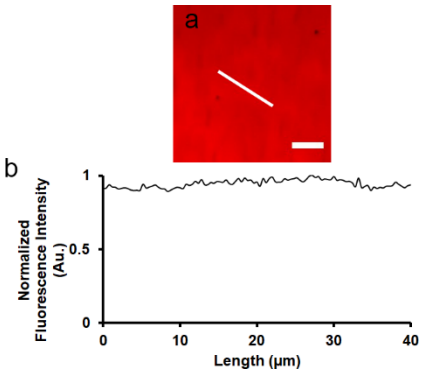

Figure 4.2. POPC Multilamellar Stack Fluorescence Intensity. (a) A wide-field fluorescence microscopy image of a multilamellar mesophase assembled with POPC and 1 mol% Rho B-DOPE. The white line across the stack depicts the manually-drawn line along which fluorescence intensity of Rho B-DOPE was measured for (b). Scale bar, 20 µm. (c) The resulting plot of Rho B-DOPE fluorescence intensity along the line normalized to the background and maximum value.

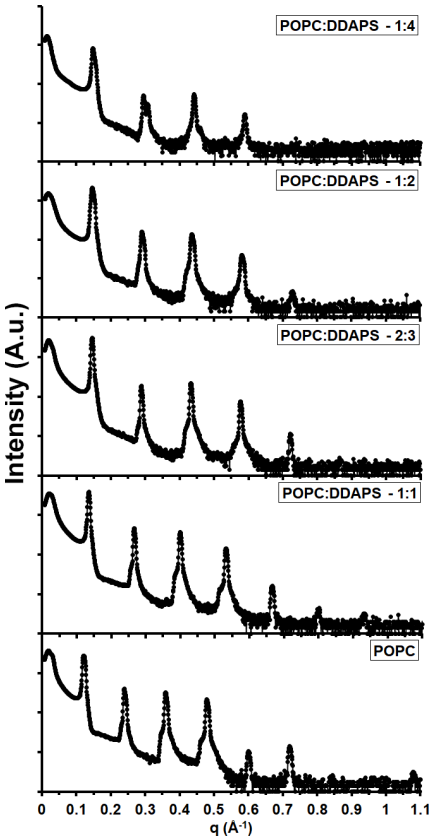

Figure 4.3. Experimental XRD Data of POPC:DDAPS Mesophases. A stacked plot of the intensities of the x-ray diffraction peaks of various POPC:DDAPS multilamellar mesophases was constructed. The molar ratios plotted include 1:0, 1:1, 2:3, 1:2, and 1:4 POPC:DDAPS.

Sample		q-values (Å^{-1})								
		q001	*q002*	*q003*	*q004*	*q005*	*q006*	*q007*	*q008*	*q009*
POPC		0.121	0.238	0.356	0.475	0.593	0.712	N.D.	N.D.	1.066
POPC:DDAPS	100:1	0.123	0.244	0.366	0.487	0.610	0.731	0.852	0.975	N.D.
	40:1	0.124	0.246	0.367	0.489	0.611	0.732	0.854	0.976	N.D.
	20:1	0.124	0.244	0.365	0.487	0.608	0.730	0.853	0.974	N.D.
	5:1	0.126	0.248	0.372	0.495	0.618	0.741	0.866	N.D.	N.D.
	5:2	0.128	0.251	0.377	0.502	0.629	0.754	0.879	N.D.	N.D.
	2:1	0.129	0.257	0.384	0.512	0.639	0.766	0.890	N.D.	N.D.
	1:1	0.135	0.267	0.399	0.532	0.666	N.D.	N.D.	N.D.	N.D.
	2:3	0.145	0.289	0.432	0.577	0.721	N.D.	N.D.	N.D.	N.D.
	1:2	0.145	0.291	0.436	0.581	0.729	N.D.	N.D.	N.D.	N.D.
	2:5	0.149	0.297	0.443	0.591	0.740	N.D.	N.D.	N.D.	N.D.
	1:3	0.138	0.276	0.412	0.549	N.D.	N.D.	N.D.	N.D.	N.D.
	1:4	0,14811	0.295	0.442	0.560	0.739	N.D.	N.D.	N.D.	N.D.

Figure 4.4. Indexed Q-Values of POPC and POPC:DDAPS Lamellar Mesophases. Indexed q-values for POPC and POPC:DDAPS lamellar mesophases as measured by XRD experimentation. Molar ratios bolded here are plotted in **Figure 4.3.**

in the spontaneous curvatures between DDAPS (presumedly J >> 0 $Å^{-1}$) and POPC (J = -0.0022 ± 0.0010 $Å^{-1}$).[33, 128] The disparity should be sufficient to drive the surfactant to phase segregate and deform the lamellar organization. At present, we do not understand the robust preservation of the lamellar order. However, the lipid-surfactant system easily dissolves when adding excess bulk water (**Figure 4.5**), therefore suggesting that our experimentally low amounts of water in the system could correlate with lamellar phase assembly within a larger phase diagram.[35, 129] *Second,* the addition of DDAPS molecules into the POPC bilayer stacks showed variable patterns of structural modulation (**Figure 4.6**). Up to a 2:3 molar ratio of POPC:DDAPS, lamellar spacing decreased gradually to a value of 43.6 Å. Concurrently, headgroup distance decreased to a near minimum of 34.4 Å at the same concentration. Above this concentration to a 1:4 molar ratio, D and D_{hh} marginally thinned to 42.5 Å and 33.5 Å respectively. In contrast, water layer thickness exhibited non-linear trends over an increasing concentration of DDAPS. At first, D_w hovered between 12.1 to 11.4 Å up to a 1:1 molar ratio but declined to 9.2 Å at a 2:3 molar ratio. Increasing DDAPS concentration beyond a 2:3 molar ratio minimally impacted water layer thickness except for an errant value of 10.9 Å around a 1:3 molar ratio. *Third*, visualizing the lipid-surfactant mixed mesophase by wide-field fluorescence microscopy displayed no significant morphological disruptions (**Figure 4.7**). Selected POPC:DDAPS mixtures (1:1, 1:2, 1:3, and 1:4) were doped with 1 mol% of Rho B-DOPE of the POPC concentration and lamellar mesophases were promptly assembled. Normalized fluorescence intensity values were examined on a line plot across the surface, and statistically homogenous intensities (94 ± 2.6%, 91 ± 4.4%, 92 ± 2.9%, and 91 ± 3.4%, for 1:1, 1:2, 1:3, and 1:4 molar ratios respectively) were observed. These observations further confirm the lamellarity of this mesophase and demonstrate a lack of significant perturbations. However, at the highest DDAPS molar fractions (≥ a 2:5 molar ratio) XRD data showed a small but detectable peak splitting towards higher q-values indicating a loss of total sample homogeneity. We anticipate that this could be a consequence of excess DDAPS within the mesophase.

To further understand the structural properties of these mixed multilamellar mesophases, samples were assembled from selected mixtures of POPC:DDAPS with 1 mol% Rho B-DOPE as a dopant and

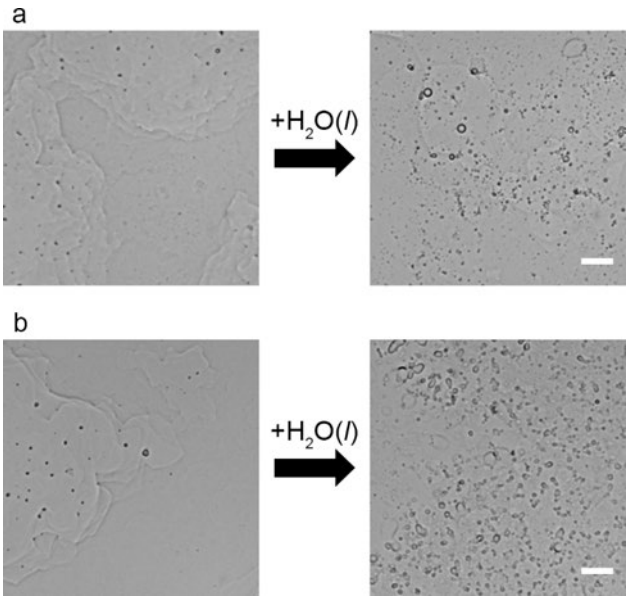

Figure 4.5. **Surface Hydration of Dried POPC:Surfactant Mixtures**. (a) Images of a dried 1:1 POPC:DDAPS mixture pre- and post-exposure to 25 μL deionized water by surface contact on the left and right respectively. (b) Images of a dried 1:1 POPC:O-Lyso-PC mixture pre- and post-exposure to 25 μL deionized water by surface contact on the left and right respectively. No lamellar structures were formed post-exposure event for (a) and (b), instead lipidic, amorphous particulate matter was seen floating in the aqueous solution after dissolution.

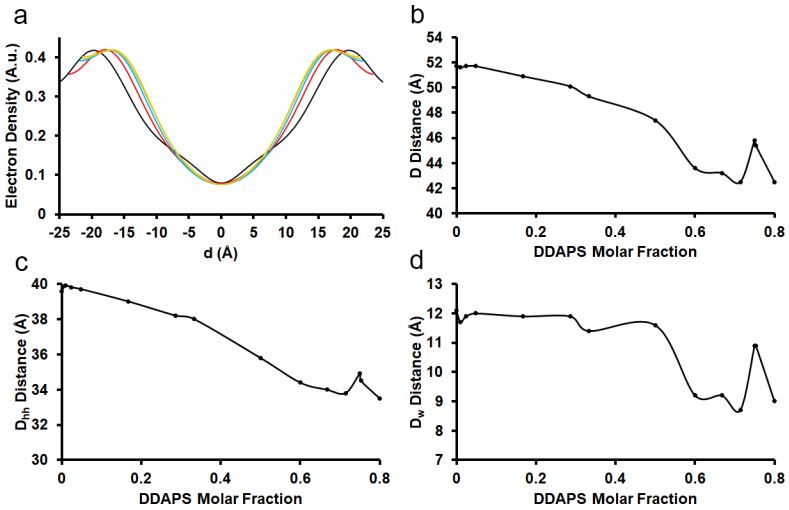

Figure 4.6. Lamellar Structure of POPC:DDAPS Multilamellar Mesophases by Molar Fraction. (a) Average electron densities normal to the bilayers were assembled from the diffraction peaks and plotted with an arbitrary scale. The molar ratios plotted include 1:0 (black), 1:1 (red), 2:3 (blue), 1:2 (green), and 1:4 (orange) POPC:DDAPS. (b) Lamellar spacing (D) of POPC:DDAPS multilamellar mesophases were deduced by XRD and plotted by molar fraction of DDAPS. (c) The headgroup-to-headgroup distance (D_{hh}) of POPC:DDAPS multilamellar mesophases were calculated by XRD and plotted by molar fraction of DDAPS. (d) Water layer thickness (D_w) was calculated from D and D_{hh} and similarly plotted.

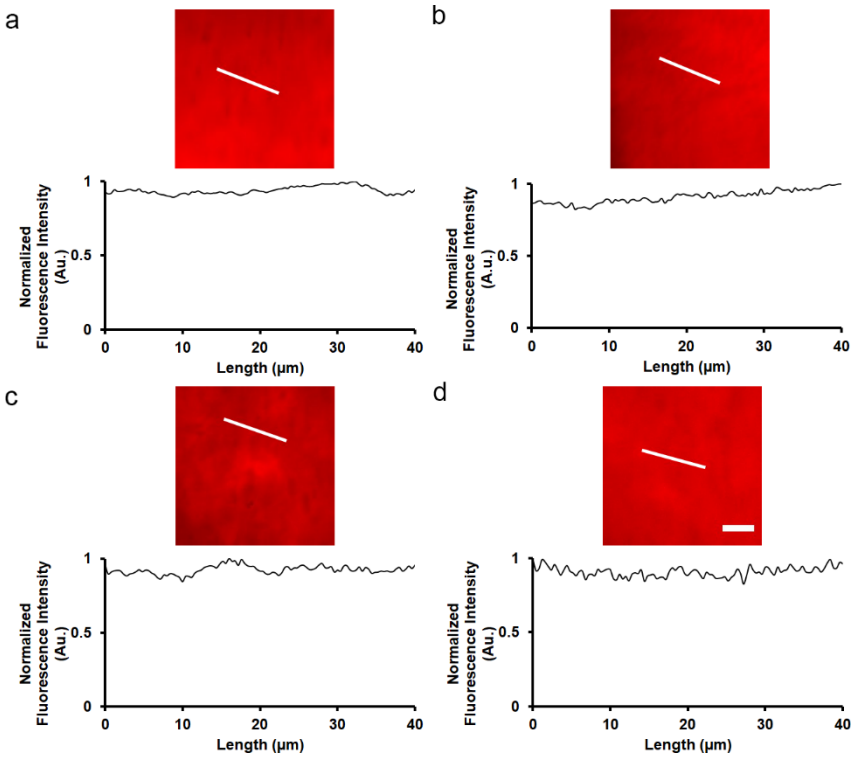

Figure 4.7. POPC:DDAPS Multilamellar Stack Fluorescence Intensity. (a-d) The wide-field fluorescence microscopy images of multilamellar mesophases assembled using a POPC:DDAPS molar ratio of (a) 1:1, (b) 1:2, (c) 1:3, and (d) 1:4 with 1 mol% Rho B-DOPE. Scale bar, 20 μm. The white line across the images depicts the manually-drawn line along which fluorescence intensity of Rho B-DOPE was measured, with the resulting measurements of fluorescence intensity of the stack normalized to the background and maximum values plotted below each image for (a-d).

investigated utilizing AFM measurements. First, AFM topographic images were acquired for the systems consisting of 1:0, 1:1, 1:2, 1:3, and 1:4 molar ratios of POPC:DDAPS respectively, all of which contained 1 mol% of Rho B-DOPE dopant (**Figure 4.8**). Topographic images clearly show plateaus and steps present among the 1:0, 1:1, and 1:2 samples (**Figure 4.8f**). At the edges of these materials, the step height of the stacked lamellae were measured to be consistent with the integer multiples of POPC bilayers (4.51 nm).[130] Therefore, these mesostructures are likely bilayer stacks similar to that prepared using the drop-and-dry method. At higher concentration ratios of DDAPS, the terraced steps are less smooth than samples with lower ratios of DDAPS (**Figure 4.8n and 4.8r**). Such structural dissonance could be a consequence of the unincorporated DDAPS as mentioned above. A commensurate edge of a different multilamellar stack with a 1:2 molar ratio of POPC:DDAPS and 1 mol% Rho B -DOPE was visualized using wide-field fluorescence microscopy, exhibiting a non-quantized increase in fluorescence intensity across the terrace morphology (**Figure 4.9**). Such an observation highlights the increased capability of AFM as a high-resolution technique for such structural analysis in future studies. Next, we measured the surface force curves (see "Materials and Methods" section above) of several selected mixtures of POPC:DDAPS (1:0, 1:1, 1:2, 1:3, and 1:4) with 1 mol% Rho B-DOPE. From these examinations, two properties could be determined: the bilayer thickness (D_t) and the bilayer rupture force (F_r) (**Figure 4.10**).[131] Surprisingly, D_t and F_r displayed no significant change in value (~4.2 nm and ~0.15 nN respectively) or correlation to surfactant concentration. Notably, the F_r values are an order of magnitude smaller than previously determined values of other liquid-crystalline bilayer mesophases.[131] We anticipate that the surfactant-induced packing disruption and non-trivial lyotropic arrangements of the hydration network in these mesophases highly modulate lamellar mechanical properties.[132, 133] It is also worth noting that discrepancies between measurements of D_t and D originate from the instrumental techniques as AFM provides precise measurement on local membranes nanomechanical properties, whereas XRD provides information about the global average modulations in lamellar structures.[131, 134]

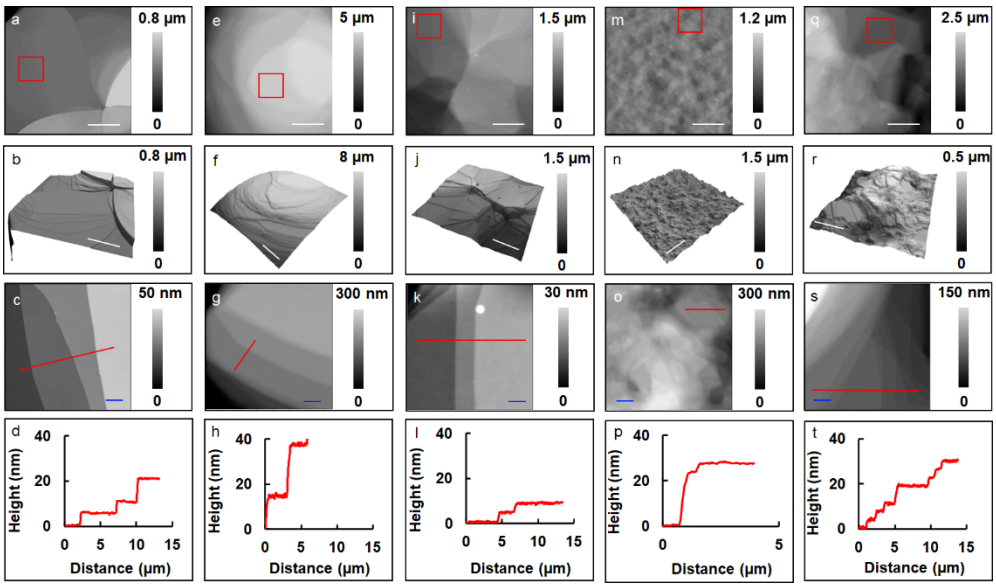

Figure 4.8. AFM Topographic Images of POPC:DDAPS Mesostructures. (a) An AFM topographic image of 1:0 molar ratio POPC:DDAPS. (b) A 3D display of (a). (c) The AFM topographic image of the area indicated by the red square in (a). (d) A cursor profile of height over the mesophase's surface as indicated by the red line in (c). (e) An AFM topographic image of 1:1 molar ratio POPC:DDAPS. (f) A 3D display of (e). (g) The AFM topographic image of the area indicated by the red square in (e). (h) A cursor profile of height over the mesophase's surface as indicated by the red line in (g). (i) An AFM topographic image of 1:2 molar ratio POPC:DDAPS. (j) A 3D display of (i). (k) The AFM topographic image of the area indicated by the red square in (i). (l) A cursor profile of height over the mesophase's surface as indicated by the red line in (k). (m) An AFM topographic image of 1:3 molar ratio POPC:DDAPS. (n) A 3D display of (m). (o) The AFM topographic image of the area indicated by the red square in (m). (p) A cursor profile of height over the mesophase's surface as indicated by the red line in (o). (q) An AFM topographic image of 1:4 molar ratio POPC:DDAPS. (r) A 3D display of (q). (s) The AFM topographic image of the area indicated by the red square in (q). (t) A cursor profile of height over the mesophase's surface as indicated by the red line in (s). Blue scale bar = 2 µm, white scale bar = 20 µm.

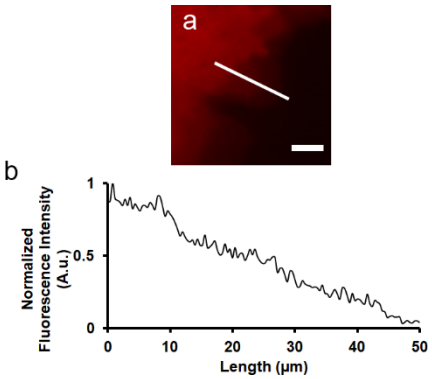

Figure 4.9. POPC:DDAPS Mutilamellar Stack Edge Fluorescence Intensity. (a) The wide-field fluorescence microscopy image of an edge of an exemplary multilamellar mesophase assembled using a 1:2 molar ratio of POPC:DDAPS with a 1 mol% Rho B-DOPE dopant. Scale bar, 20 μm. The white line across the images depicts the manually-drawn line along which fluorescence intensity of Rho B-DOPE was measured, with the resulting measurements of fluorescence intensity of the stack normalized to the background and maximum values plotted below each image for (b).

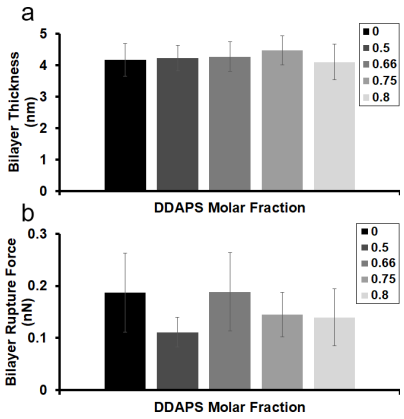

Figure 4.10. Bilayer Thickness and Rupture Force of POPC:DDAPS Multilamellar Mesophases by Molar Fraction as Measured by AFM. (a) Bilayer thickness (D_t) of POPC:DDAPS multilamellar mesophases were deduced by AFM across the entire stack, averaged, and plotted by molar fraction of DDAPS. Error bars are standard deviations. (b) Bilayer rupture force (F_r) of POPC:DDAPS multilamellar mesophases were similarly elucidated and plotted by molar fraction of DDAPS. Error bars are standard deviations.

Considering these findings, the dynamics of another micelle-forming zwitterionic surfactant, O-Lyso-PC (J = 0.0263 $Å^{-1}$), was investigated when mixed with POPC in the lamellar mesophases (at molar ratios of 100:1, 40:1, 20:1, 5:1, 5:2, 2:1, 1:1, 2:3, 1:2, 2:5, 1:3, and 1:4).[128] From a chemical perspective, O-Lyso-PC differs from DDAPS in multiple properties: CMC (being 2-4 mM for DDAPS and ~10^{-7}-10^{-6} M for O-Lyso-PC), headgroup structure (a sulfobetaine group for DDAPS and a phosphocholine group for O-Lyso-PC), and hydrophobic chain tail length (12 carbon atoms for DDAPS and 18 carbon atoms with a double bond at the 9^{th} position for O-Lyso-PC).[135] Modelling these two molecules have also displayed a difference in their headgroup hydration (in the form of their hydrogen bond acceptor count), being 3 for DDAPS and 7 for O-Lyso-PC in comparison to 8 for POPC.[136-138] The resulting XRD measurements elucidated trends in structural properties for this mixed lipid-surfactant system. *First,* the lamellar motif of these mixed mesophases was maintained across the entire concentration range of O-Lyso-PC (**Figure 4.11 and 4.12**). Again, these findings are notable due to the large discrepancy in curvature between the involved amphiphiles. *Second,* the addition of O-Lyso-PC perturbed the structural properties of the lamellar motif with unique directionality (**Figure 4.13**). Lamellar spacing (D) stayed mildly constant around a value of 52.1 Å from a 100:1 to a 2:3 molar ratio of POPC:O-Lyso-PC. At a 1:2 molar ratio, it markedly decreased to a value of 49.5 Å. With larger amounts of O-Lyso-PC, D monotonically decreased to a value of 48.6 Å at a 1:4 molar ratio. However, D_{hh} decreased continuously across the range of concentrations of O-Lyso-PC, beginning at 39.2 Å and ending at 33.7 Å for 100:1 and 1:4 molar ratios respectively. Therefore, the non-linear behavior of the trend in D can mainly be attributed to the variance in D_w. Up to a 2:3 molar ratio, the water layer thickness surprisingly increased from 12.8 Å to 16.3 Å. At a 1:2 ratio of POPC:O-Lyso-PC, the water layer thickness pointedly decreased to a value of 14.0 Å. Beyond this concentration of O-Lyso-PC, the thickness marginally increased to 14.9 Å at a molar ratio of 1:4. *Third,* no morphological anomalies were observed upon visualization by wide-field fluorescence microscopy (**Figure 4.14**). Certain POPC:O-Lyso-PC mixtures (1:1, 1:2, 1:3, and 1:4 molar ratios) were doped with 1 mol% of Rho B-DOPE of the POPC concentration and lamellar mesophases were similarly assembled. Normalized fluorescence intensity values were examined on a line plot across the surface, and a statistically homogenous intensity (95 ± 3.2%,

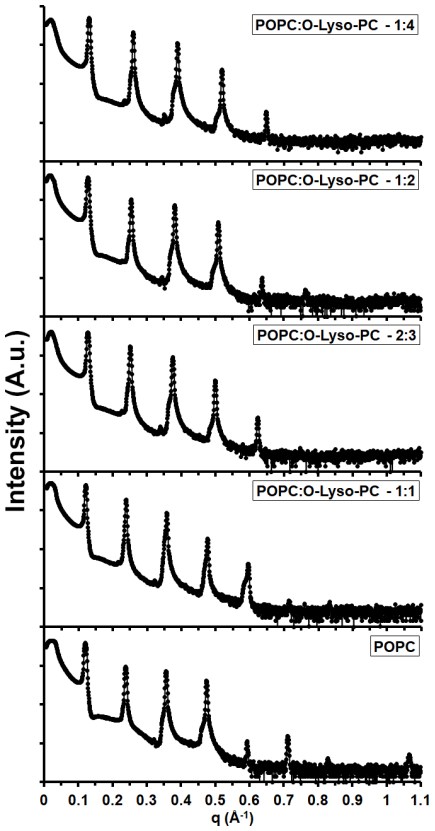

Figure 4.11. Experimental XRD Data of POPC:O-Lyso-PC Mesophases. A stacked plot of the intensities of the x-ray diffraction peaks of various POPC:O-Lyso-PC multilamellar mesophases was constructed. The molar ratios plotted include 1:0, 1:1, 2:3, 1:2, and 1:4 POPC:O-Lyso-PC.

Sample		q-values (Å^{-1})								
		q001	*q002*	*q003*	*q004*	*q005*	*q006*	*q007*	*q008*	*q009*
POPC		0.121	0.238	0.356	0.475	0.593	0.712	N.D.	N.D.	1.066
POPC:O-Lyso-PC	100:1	0.122	0.241	0.362	0.482	0.603	0.723	0.845	0.965	1.092
	40:1	0.123	0.242	0.362	0.483	0.603	0.723	0.844	0.964	1.081
	20:1	0.122	0.240	0.359	0.478	0.598	0.718	N.D.	N.D.	N.D.
	5:1	0.124	0.244	0.364	0.486	0.608	0.729	0.849	0.972	1.093
	5:2	0.125	0.246	0.369	0.492	0.615	0.737	N.D.	N.D.	N.D.
	2:1	0.122	0.239	0.358	0.477	0.597	N.D.	0.832	N.D.	N.D.
	1:1	0.122	0.239	0.357	0.476	0.595	0.714	N.D.	N.D.	N.D.
	2:3	0.127	0.251	0.376	0.499	0.624	N.D.	N.D.	N.D.	N.D.
	1:2	0.129	0.254	0.381	0.509	0.637	0.762	N.D.	N.D.	N.D.
	2:5	0.131	0.258	0.387	0.514	N.D.	N.D.	N.D.	N.D.	N.D.
	1:3	0.129	0.259	0.389	0.512	0.639	N.D.	N.D.	N.D.	N.D.
	1:4	0.132	0.260	0.389	0.519	0.649	N.D.	N.D.	N.D.	N.D.

Figure 4.12. Indexed Q-Values of POPC and POPC:O-Lyso-PC Lamellar Mesophases. Indexed q-values for POPC and POPC:O-Lyso-PC lamellar mesophases as measured by XRD experimentation. Molar ratios bolded here are plotted in Figure 4.11.

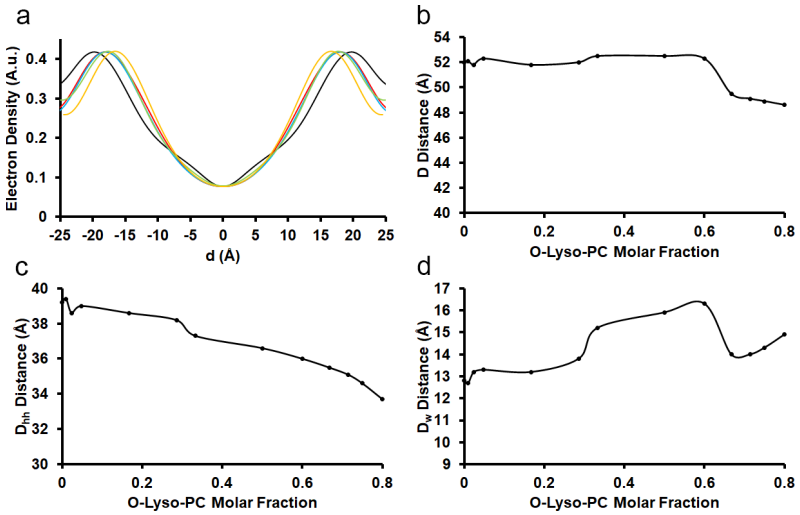

Figure 4.13. Lamellar Structure of POPC:O-Lyso-PC Multilamellar Mesophases by Molar Fraction. (a) Average electron densities normal to the bilayers were assembled from the diffraction peaks and plotted with an arbitrary scale. The molar ratios plotted include 1:0 (black), 1:1 (red), 2:3 (blue), 1:2 (green), and 1:4 (orange) POPC:DDAPS. (b) Lamellar spacing (D) of POPC:O-Lyso-PC multilamellar mesophases were deduced by XRD and plotted by molar fraction of O-Lyso-PC. (c) The headgroup-to-headgroup distance (D_{hh}) of POPC:O-Lyso-PC multilamellar mesophases were calculated by XRD and plotted by molar fraction of O-Lyso-PC (d) Water layer thickness (D_w) was calculated from D and D_{hh} and similarly plotted.

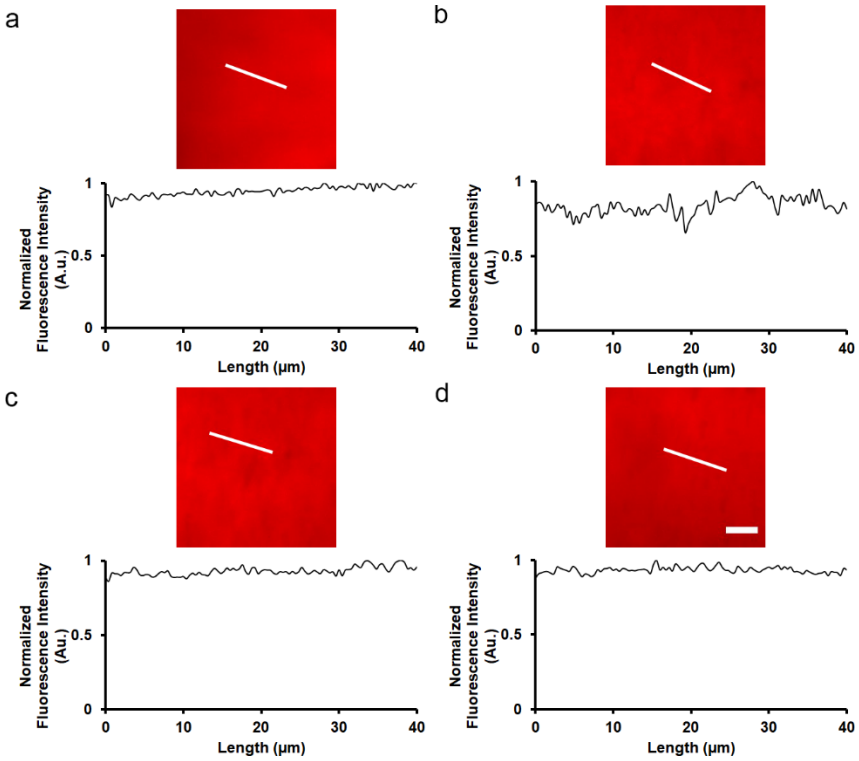

Figure 4.14. POPC:O-Lyso-PC Multilamellar Stack Fluorescence Intensity. (a-d) The wide-field fluorescence microscopy images of multilamellar mesophases assembled using a POPC:O-Lyso-PC molar ratio of (a) 1:1, (b) 1:2, (c) 1:3, and (d) 1:4 with 1 mol% Rho B-DOPE. Scale bar, 20 μm. The white line across the images depicts the manually-drawn line along which fluorescence intensity of Rho B-DOPE was measured, with the resulting measurements of fluorescence intensity of the stack normalized to the background and maximum values plotted below each image for (a-d).

84 ± 6.3%, 93 ± 2.8%, and 94 ± 2.1%, for 1:1, 1:2, 1:3, and 1:4 molar ratios respectively) was observed. These observations foreground the homogeneity of the lamellar mesophases without perturbations by physical phenomena, unlike the previous surfactant-rich POPC:DDAPS mesophases.

Given the above results, we investigated the necessity of POPC to form the lamellar motif within these mixed mesophases. An identical procedure of mesophase assembly was followed with a 0:1 molar ratio of POPC:DDAPS and POPC:O-Lyso-PC with Rho B-DOPE doped at a 1 mol% of the surfactant concentration. Visualizing the resulting morphologies with wide-field fluorescence microscopy featured little to no multilamellar mesophases (**Figure 4.15**). The amphiphilic mixtures, after water vapor hydration, appeared as amorphous "islands" with no indication of multilamellar stacks. Such results indicate that POPC is a necessity for the formation of the lamellar motif. Further analysis can describe the concentration-dependent relationship of the phase behavior of this ternary system.

The assembly of POPC:DDAPS and POPC:O-Lyso-PC multilamellar mesophases by water vapor hydration and their varied trends in structural properties elicit numerous questions. Primarily, how is the solubilizing action of detergents inhibited at ratios of POPC to surfactant greater than the saturation limit of POPC bilayers?[6, 139, 140] And, where do the different trends in structural properties originate as surfactant concentrations change? We believe that the proceeding insights foreground the need to abandon the three-stage model and create inclusive models of membrane-detergent mechanistic action..[7]

We begin by examining our experimental medium, water. Water has displayed an acute level of complexity as a solvent and local environmental medium. For example, terahertz time-domain spectroscopy found that the hydration network surrounding a self-assembling amphiphilic polymer differentiated depending on the phase of its assembled mesophase.[141] Specifically, the adjacent two layers of water molecules modulated in tune with amphiphile self-assembly. Further, past efforts have found a differentiated hydration network structure between the inside and outside of a multilamellar cylindrical assembly of cardanyl glucosides.[142] Another example of this principle occurs when exchanging the sodium from sodium didodecyl sulfosuccinate to lithium, aqueous solubility and lateral headgroup area

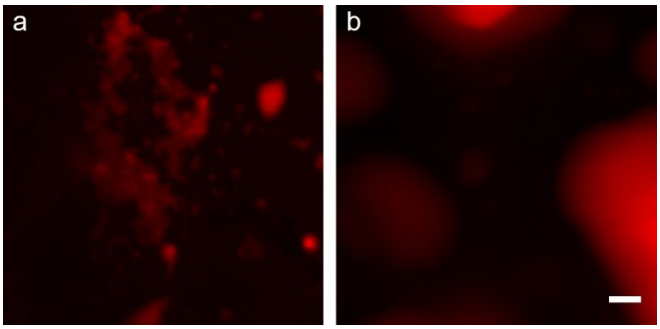

Figure 4.15. DDAPS And O-Lyso-PC Assemblies Upon Water Vapor Hydration. (a) A wide-field fluorescence microscopy image of the morphologies assembled by a 0:1 molar ratio of POPC:DDAPS with 1 mol% Rho B-DOPE doped. (b) A wide-field fluorescence microscopy image of the morphologies assembled by a 0:1 molar ratio of POPC:O-Lyso-PC with 1 mol% Rho B-DOPE doped.

dramatically increases due to changes in its resulting hydration network.[143] Other such works exhibit similar findings: mixed zwitterionic-anionic micellar mesophases modulate the CMC and precipitation phase boundaries (and therefore the surrounding hydration network). This is in contrast to the pure mesophases of the anionic amphiphile structures.[144] An array of studies exhibits a mutualistic relationship between environment and an experimental system's assembly.[145-147] Therefore our results, displaying surfactant specific trends in hydration network, agree with the notion that the chemical composition of the experimental mesophase modulates the hydrating water network.

Next, we focus on the non-trivial properties of lipidic multilamellar mesophases. This lyotropic arrangement of lamellae merits itself as an interesting subject of study due to its prevalence in nature, including plant chloroplasts and lamellar bodies.[45, 46, 148] The organization of these smectic layers is stabilized by interlamellar interactions (or Helfrich interactions) which separates individual bilayers.[71] Between the bilayers, an interstitial water layer exists which hydrates the amphiphiles' headgroups allowing for the exchange of monomers between layers.[71] Structurally locked by this balance of van der Waals forces and the hydrating network, participating amphiphiles still possess lateral fluidity amongst their neighbors.[149-151] One area of interest about these mesophases is what happens when an adjacent bilayer is perturbed? Recent efforts by our group have exhibited the ability of these stacks to couple their behaviors three-dimensionally during events such as domain-forming phase separation.[24] From this, it was proposed that the dynamics of headgroup hydration encourage interlayer alignment of phases across the membranous stack. Peculiar hydration dynamics are not limited to just planar stacks, but are also found in cylindrical multilamellar tubes (termed myelin figures) as well.[77] Such complexities in amphiphile behavior can be exploited for morphogenesis, especially in response to external dopants like the detergents of focus in this work.[33] However, here the involved surfactants are distributed within the amphiphilic mixture pre-water vapor assembly. Therefore, these detergents should be randomly arranged within the multilamellar mesophase and not doped externally. Given this knowledge, we suggest that the solubilizing activity of the focal detergents is inhibited within multilamellar frameworks by the energetic cost of morphologically

bending the membranes. This is compounded by the energetic cost to reorganize the lyotropic correspondence of adjacent bilayers and hydration networks within the stack (**Figure 4.16**).[93]

To study the impact of the surfactant's chemical properties on the lamellar stack, we investigate the amphiphile's headgroup. In our work, both the participating surfactants have zwitterionic headgroups at the pH of deionized water. Alone, this leads to a large discrepancy in their ability to intercalate within the bilayer and flip-flop into the other leaflet.[95, 97] Since these amphiphiles translocate so slowly, the surfactants will presumably accumulate locally in their resident leaflet instead of equilibrating across the bilayer.[5] Because of this, both the spatial configuration of the charges on the atomic components in the headgroup as well as their local population within the lamellae could non-trivially impact structural considerations. As an example, investigations of micellized sulfobetaine headgroups, like that in DDAPS, determined that ion spatial arrangement is influenced by the minimization of dipole-dipole repulsion, local entropic costs, and the maximization of hydration.[152, 153] Significantly, there is a calculated discrepancy in the hydrogen bond acceptor count of the two surfactant species and POPC (as computed by Cactvs 3.4.8.18 and released by PubChem), being 3 for DDAPS, 7 for O-Lyso-PC, and 8 for POPC.[136-138] Such discrepancies in hydration can influence the packing of lipid-lysolipid mixed mesophases.[154] These competing thermodynamic properties are further complicated by the variance of intermolecular interaction energies with bilayer composition: amphiphiles with identical chain lengths and different headgroups doped into lipidic lamellae can maximize their intermolecular interaction energies at different molar ratios. This foregrounds the consequences of differential van der Waals and electrostatic forces in structural behavior once intercalated into the bilayer.[155] Therefore, it is reasonable to suggest that the arrangement of the phosphocholine and sulfobetaine headgroups will modulate structural and hydration behavior relative to POPC:O-Lyso-PC mesophases.[156]

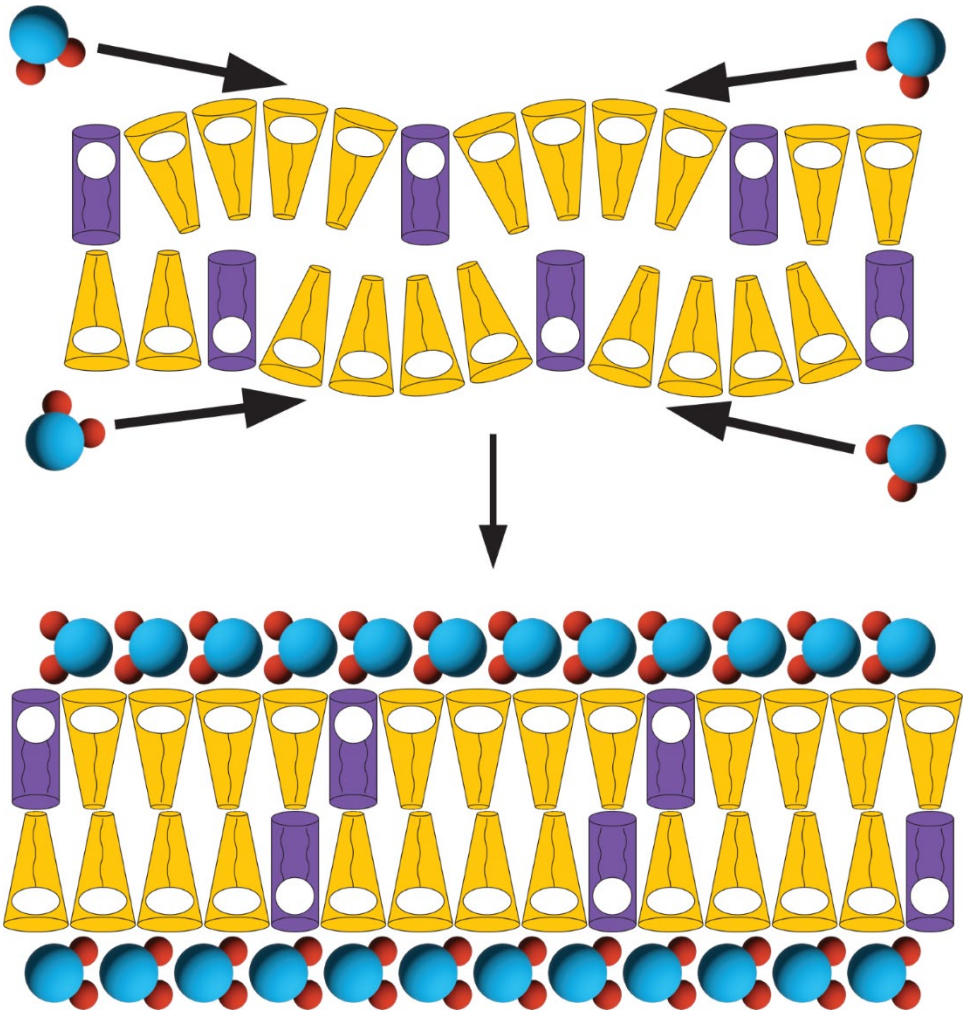

Figure 4.16. Water Vapor-Mediated Assembly of Multilamellar Mesophases. A cartoon representation of a proposed mechanism of the water vapor hydration of the POPC:surfactant mixtures into multilamellar mesophases. Dried mixtures of POPC (purple cylinders) and surfactants (yellow cones) are hydrated by the surrounding water (blue and red models) within the humidity chamber, and lyotropic networks of amphiphiles and water assemble. In this mechanism, the morphological consequences of differentiated spontaneous curvature (and therefore solubilization) are repressed upon hydration due to energetical considerations of bilayers bending and the hydration network reorganizing.

Second, we consider the amphiphile's hydrophobic chain tails. In our work, our experimental detergents have different tails: a C12:0 alkyl chain for DDAPS and a C18:1 (Δ^9) acyl tail for O-Lyso-PC, in comparison to POPC with a C18:1 (Δ^9) acyl tail and a C16:0 acyl tail. It is important to note that a significant array of experimental works have elicited a generalized surfactant-induced disordering of the non-polar space populated by the hydrophobic chain tails within bilayers.[5] The mismatch of van der Waals interactions between the lipid's and surfactant's hydrophobic components perturbs the bilayer's packing, leading to its thinning.[5, 157] Such perturbation can explain previously accounted behavior within multilamellar myelins, surfactant-mediated bilayer thinning can affect the exterior bilayers and initiate the twisting event of the multilamellar system.[33] Our work highly aligns with this principle, as seen between the strong negative correlation between surfactant concentration and headgroup-to-headgroup distance measurements. However, it is worth noting that our regressions of D_{hh} with surfactant concentration are component specific. We propose that this minute variability is a consequence of changes in van der Waals interactions due to the different chemical structures, consistent with previous literature. For example, lysolipid detergents can increase fluidity and decrease the bending rigidity of phospholipid membranes, exhibiting a positive correlation between chain length and bending rigidity.[158, 159] Furthermore, the same investigation found that the partitioning coefficients of the same lysolipid detergents within membranes correspond with acyl chain length.[159] This is similarly true for amphiphiles with sulfobetaine headgroups doped into lipidic bilayers, longer hydrophobic chain tails correlate with stronger partitioning and a higher potential to micellize.[160, 161] Further investigation found that hydrophobic chain tails of DDAPS can fold back on themselves within micellar structures, foregrounding their potential for packing mismatch.[162] Such results align with our proposal above, signifying that molecule-specific hydrophobic chain tail mismatch likely determines the value of D_{hh} and its relative regressions.

4.4. CONCLUSION

Here, multilamellar mesophases composed of POPC, POPC:DDAPS, and POPC:O-Lyso-PC mixtures were assembled by water vapor hydration and investigated with XRD techniques. Such mixed mesophases were formed across the entire concentration range employed, between 100:1 and 1:4 molar ratios of POPC:surfactant. Notedly, POPC:surfactant mixtures dissolved as an isotropic solution of mixed micelles when hydrated by bulk liquid water instead as visualized by brightfield optical microscopy. Lamellar spacing, headgroup-to-headgroup distance, and water layer thickness of the assembling bilayers were all calculated from the XRD measurements. Generally, D decreased with larger amounts of surfactant and D_{hh} decreased monotonically with increasing surfactant concentration. However, trends of D_w were highly variable with surfactant incorporation. D_w of POPC:DDAPS mesophases stayed mildly constant (around 11.8 Å) until a decline to 9.2 Å at a 2:3 molar ratio. In contrast, POPC:O-Lyso-PC mesophases displayed an increase of D_w from 12.8 Å at a 100:1 molar ratio to 16.3 Å at a 2:3 molar ratio, proceeded by a decrease to 14.0 Å at a 1:2 molar ratio. Selected molar ratios (1:1, 1:2, 1:3, and 1:4) of POPC:DDAPS and POPC:O-Lyso-PC mixtures were doped with 1 mol% Rho B-DOPE of the POPC concentration, assembled into multilamellar stacks, and visualized by wide-field fluorescence microscopy. This resulted in negligent perturbation of the lamellar motif by physical phenomena like phase separation events. Identical mixtures of POPC:DDAPS with 1 mol% Rho B-DOPE dopant were assembled into multilamellar mesophases and investigated using AFM. Such measurements indicated a homogenous topography across the multilamellar stack for surfactant-poor and surfactant-rich samples with bilayer thickness (D_t) bilayer rupture force (F_r) hovered around ~4.2 nm and 0.15 nN respectively for the entire surfactant concentration range.

Our findings regarding these unique multilamellar mesophases suggest a large scope of conclusions. *First,* these mesophases, composed of a wide range of POPC:surfactant molar ratios, foreground an interesting water-deficient phase behavior region. Further research could describe a complete depiction of the phase diagrams (POPC:DDAPS/O-Lyso-PC:water), leading to a more holistic

understanding of our surfactant-membrane systems. *Second,* the variance in trends of structural properties highlights the consequential, non-trivial thermodynamic interactions of our experimental components like the chemical potential of the hydrating water, the van der Waals interactions of the chemical structures, and the electrostatic considerations during packing. Specifically, the hydration of the hydrophilic headgroups and the mismatch of the hydrophobic chain tails likely dictate the structural properties of the involved bilayers. Such considerations are not traditionally considered when examining the macroscale morphological changes of surfactant-membrane systems.[7] *Third,* this work agrees with the sentiment that water is not just a bulk solvent but an involved component of this self-assembling system. Such shift in experimental framework can inform future scientific efforts in self-assembly and possibly lead to the development of novel solubilization assays for the efficient sequestering of membrane-bound proteins using solid-adsorbed surfactant material. Taken together, we stress that our understanding of surfactant activity must move beyond the three-stage model and into a kinetically and chemically complex world.

4.5. MATERIALS AND METHODS

Materials. 1-Palmitoyl-2-oleoyl-*sn*-glycero-3-phosphocholine (POPC), 1,2-dioleoyl-*sn*-glycero-3-phosphoethanolamine-*N*-(lissamine rhodamine B sulfonyl) (ammonium salt) (Rho B-DOPE), and 1-oleoyl-2-hydroxy-*sn*-glycero-3-phosphocholine (O-Lyso-PC) were purchased from Avanti Polar Lipids (Alabaster, Al). *n*-Dodecyl-*N,N*-dimethyl-3-ammonio-1-propanesulfonate (DDAPS) was acquired from MilliporeSigma (Burlington, MA). Chloroform, methanol, and 2,2,2-trifluoroethanol were purchased from Sigma-Aldrich (St. Louis, MO). Silicon [100] wafers were acquired from Sigma-Aldrich (St. Louis, MO) and borosilicate microscope slides were obtained from Corning (Corning, NY). Nitrogen gas was acquired from Praxair (Danburt, CT). Deionized water was prepared with a Milli-Q Synthesis water purification system (>15 M-Ohm/cm; MilliporeSigma; Burlington, MA). All chemicals were used without further purification.

X-Ray Diffraction Sample Preparation, Measurements, and Analysis. XRD experiments were performed on multilamellar stacks of oriented lipid bilayers deposited on freshly cleaned hydrophilic silicon [100] wafers. Silicon substrates, cut to 18x20 mm, were sonicated for 15 min in methanol followed by another 15 min in deionized water a total of three times. Substrates were then nitrogen-dried and exposed to short-wavelength UV radiation for 30 min to make the surface hydrophilic.

The wafers were placed on an accurately-leveled platform for amphiphile deposition. 0.002 mol of POPC and the desired amount of surfactant were dissolved in 200 μl of a 1:1 solution of chloroform:2,2,2-trifluoroethanol, and then the solution was deposited drop by drop on the silicon substrate. The wafer was left covered for 2 hrs in a fume hood for slow evaporation. It was then placed under high vacuum for 24 hrs to remove trapped solvents. The lipid-dried film was equilibrated under 98% relative humidity (RH) at a temperature of 50ºC for 48 hrs then, finally, it was equilibrated at room temperature for an additional 24 hrs at 98 % RH, which was achieved by a reservoir filled with a saturated K_2SO_4 solution.[163]

The diffraction measurements were carried out using an in-house Cu Kα tube spectrometer with wavelength 1.54 Å operating in the horizontal plane. During the in-house X-ray diffraction measurements, we used a specially constructed humidity cell designed for high accuracy and sensitivity in RH.[164] The scattered intensity was plotted as a function of Q (scattering vector), which is directly related to the scattering angle by $Q = 4\pi\sin(\theta)/\lambda$, where λ is the wavelength of the X-rays. Therefore, we obtained one-dimensional I(Q) profiles for each sample, showing up to nine Bragg orders of magnitude. The X-ray diffraction pattern presented a series of sequential peaks positioned at equal interpeak distance, characteristic of a lamellar phase. The diffraction peaks were fitted by Gaussians after background subtraction to determine their positions and areas under the peak. Miller indices (hkl) correspond to those of a lamellar phase for all studied samples: 001, 002, 003…. The lamellar spacing (D) of the mesophase was calculated following Bragg's lw for a 1D crystal on a plot of peak location (q) vs. diffraction order (h) and using the following equation: $D = 2\pi/\Delta q$. The addition of surfactants leads to an expected higher

disorder on the phospholipid lipid bilayers due to interferences between the bilayer and surfactant molecules. However, for all diffraction pattern obtained, the full width at half maximum (FWHM) of diffraction peaks remained between 0.005-0.007 for all samples, which indicates a similar quality in all the amphiphilic films. Moreover, XRD measurements show signatures of a form factor corresponding to possible thermal smectic fluctuations of lipid bilayers.[37, 165] However, an increase in peak widths has a minor effect compared to peak height changes.

The integrated intensity of n^{th} order peaks (I_n) was then used to calculate the electron density profiles with the following equation:

$$\rho_{bilayer}(z) = \frac{2}{D}\sum_{n=1}^{M} f_n v_n cos\left(\frac{2n\pi}{D}z\right)$$

where the coefficients f_n can be found with the formula $I_n = \frac{|f_n|^2}{Q_z}$, Q_z is the Lorentz correction factor equal to q for oriented bilayers, and v_n corresponds to the phase of the structure factor corresponding to the POPC.[24, 166] The phases used for each order were [-1, -1, +1, -1, +1, -1, -1, -1, -1]. Absorption correction for oriented samples was applied on intensities as described previously.[167] Finally, the distance between the two characteristic maxima was attributed to the lipid headgroup to headgroup distance (D_{hh}) along the bilayer normal and the water layer thickness (D_w) between lipid bilayers was defined as $D_w = D - D_{hh}$.

Lipid:Surfactant Sample Preparation for All Microscopy Techniques. Supported multilamellar membranes were prepared by adapting a similar method of liquid deposition and gaseous hydration to the section above.[24] Borosilicate glass cover slides were cleaned by sonication in methanol then deionized water for 15 min three times. The surface supports were then dried with nitrogen gas and treated by UV radiation (185 nm and 254 nm) for 30 min. Sample stock solutions were prepared by dissolving 1 μmol of POPC and 10 nmol of Rho B-DOPE in a 50% volume percent (v/v) solution of chloroform:2,2,2-trifluoroethanol. Then varying molar equivalents (in relation to POPC) of DDAPS or O-Lyso-PC was

added and diluted to a final volume of 200 µL of the 1:1 v/v mixture. Sample stock solutions used for brightfield optical microscopy experimentation did not include Rho B-DOPE. Once cleaned, 50 µL of the prepared lipid stock solution was pipetted on to the surface supports on a level platform. The supports were covered by aluminum foil and the solution was allowed to dry in the atmosphere for 2 hrs and then dried by house vacuum overnight. The surface supports were sealed in a humidity chamber and the relative humidity was elevated to 98% by a saturated K_2SO_4 solution for 24 hrs in a 55°C oven. The surface supports were allowed to equilibrate to room temperature for at least 24 hrs at 98% RH. Care was taken to minimize errors caused by condensation within the seal (by careful handling of the chamber or transfer to another humidity chamber). Afterwards, the surface supports were brought to the appropriate instrument for analysis or stored at room temperature in their sealed humidity chamber. All samples were used that same day or properly resealed for usage within 14 days.

Brightfield Optical Microscopy Visualization. Brightfield optical microscopy measurements were performed using a Nikon Eclipse TE2000S inverted fluorescence microscope (Technical Instruments, Burlingame, CA) equipped with a Roper Cool Snap CCD camera (Technical Instruments, Burlingame, CA). Videos were taken using a Plan Fluor 20X (NA, 0.25) air objective (Nikon, Japan). The resulting micrographs were processed using the ImageJ software package.

Wide-field Fluorescence Microscopy and Image Analysis. Wide-field fluorescence microscopy measurements were performed using a Nikon Eclipse TE2000S inverted fluorescence microscope (Technical Instruments, Burlingame, CA) equipped with a Roper Cool Snap CCD camera (Technical Instruments, Burlingame, CA) and Hg lamp as a light source. Videos were taken using a Plan Fluor 20X (NA, 0.25) air objective (Nikon, Japan) and filter cubes to filter absorption and emission of the source and camera. All images and videos were collected with the samples still housed in the humidity chamber and

analyzed using the ImageJ software package. Fluorescence intensity was computed by measurements normalized to the maximum and background values of the surface supports.

Atomic Force Microscopy Topography Investigation and Analysis. AFM images were acquired using a deflection type configuration (MFP-3D, Oxford Instrument, Santa Barbara, CA) following similar protocols reported previously.[131] Silicon nitride probes (MSNL-10 E, k = 0.1 N/m, Bruker, Camarillo, CA) were used to characterize the topology of the printed structures. Image acquisition was done using tapping mode with 40-60% damping.[168, 169] Image processing and display were performed using the MFP-3D software developed on the Igor Pro 6.20 platform. Supported multilamellar membranes were prepared following the same methods as that for wide-field fluorescence microscopy imaging.

The force versus distance profiles were acquired by approaching the probe to the lipid constructs from above at a constant velocity (100 nm/s). The vertical force applied to the amphiphilic mesophases was known to perturb the interactions between molecules.[134] The spring constant of each probe was calibrated based on measurements of thermal fluctuations of the cantilever.[170] All experiments were performed at 24°C in a temperature-controlled room with stability of ± 1°C. Force-distance plots were displayed and analyzed using the MFP-3D software developed on the Igor Pro 6.20 platform.

4.6. FUNDING AND COLLABORATORS

This work is supported by a grant from the National Science Foundation (DMR-2104123). I am grateful to my collaborators, Dr. Marta Salvador-Castell, Yuqi Huang, and Prof. Sunil Sinha for their support of the above work.

CHAPTER 5 – Destructive Tendencies of *Doryteuthis opalescens*: Perturbation of Lipidic Lamellar Mesophases by the Cellular Machinery of the California Market Squid

5.1. ABSTRACT

Cellular life can proliferate because of innumerous microscopic machines. Biological proteins, originating from the central dogma of molecular biology, are the cell's functional machinery. Their uses can include communication, digestion, transportation, and several others. One specific class of this family of biomolecules is membrane active proteins (MAPs) which interact or bind with lipidic, lamellar membranes as they perform their desired functions. Whether inserted into the bilayer or bound to the interface, such cellular machinery perform vital tasks for the organism at large. A highly unique example is the reflectin family of proteins in *Doryteuthis opalescens* (commonly known as the California market squid). Recent investigations found that these proteins reflect visible light in a tunable manner as part of the organism's camouflage mechanism while functionally possessing the ability to bind to cellular membranes. Here, we further investigate the membrane active properties of two specific reflectin proteins (A1 and C) when interacting with both unilamellar (in the form of giant unilamellar vesicles or GUVs) and multilamellar (in the form of myelin figures) mesophases. Using wide-field fluorescence and brightfield microscopy, consequential dynamics of reflectin-membrane interactions were visualized in real-time. We found that reflectin A1 commonly perturbs and reorganizes both lipidic structures in a concentration-dependent manner, while reflectin C does not qualitatively impact membranes. Unique pathways of morphogenesis were observed for each lipidic structure when exposed to reflectin A1: GUVs burst at high concentrations while budding or shrinking at lower concentrations and myelins lost material as lipid aggregates. Furthermore, GUVs exposed to sequential mixtures of reflectin C then A1 at molar ratios of ≤ 10:1 exhibited similar behaviors as those above, elucidating the aggressive activity of reflectin A1. Taken as such, these results illuminate the complex relationships of membrane active proteins *in vivo* and inspire the design of interesting thin film materials.

5.2. INTRODUCTION

Evolutionarily, aquatic animals (both pelagic and benthic) have developed different types of coloration for a plethora of reasons, including crypsis, camouflage, and thermoregulation.[171-173] While several coloration patterns can be accomplished due to common methods like pigmentary colors (also known as chromatophores) or mirroring scales, an alternative mechanism is the reflection of light.[18, 173, 174] Light reflection is commonly accomplished by purine crystals within aquatic animals; however, cephalopods can reflect a variety of colors of light due to a specialized set of skin cells called iridocytes.[175] These tissues act as an efficient, biological Bragg reflector system where light gets refracted from intercalated folds of cellular cytosol and extracellular fluid.[18, 175] Previous research efforts have elucidated one such system, the family of proteins known as reflectins in the California market squid (*Doryteuthis opalescens*).[176] Mechanistically, the neurotransmitter acetylcholine binds membrane-bound receptors which induce a multistep pathway leading to the phosphorylation of positively-charged, histidine-rich linkers within reflectin proteins.[176] By overcoming coulombic repulsion (either by phosphorylation or by pH *in vitro*), the proteins can reversibly condense and dehydrate such that water is expelled as a Gibbs-Donnan equilibration from the protein-rich sections of the cytosol into the extracellular space.[176-179] Further research has elucidated the tunability of this biological system, as condensation intensity and the wavelength of light are correlated, foregrounding its potential as a biophotonic material.[177, 180, 181] Immunohistochemical localization analysis found that these reflectin proteins exist in close proximity to cellular membranes within these Bragg reflector systems.[180] Therefore, are there any interactions between these functional proteins and the cellular membrane?

A recent study has investigated the membrane active behaviors of the reflectin proteins A1 and C, two unique individuals within the larger family.[18] There, small unilamellar vesicles (SUVs) composed of a mixture of neutral and negatively-charged biomimetic phospholipids were exposed to solutions of both proteins at various concentrations and acidities (as a parallel for protein condensation). The group found that both reflectins multivalently bound these SUVs and form aggregates in a pH- and concentration-

dependent manner.[18] In addition, it was found that reflectin A1 can aggressively reorganize lamellar membranous structures when partially or fully digested by proteinase K. In contrast, reflectin C exposed to identical treatments of proteinase K released their bound SUVs. Such results lead us to the current hypothesis that individual reflectin proteins within the biological mixture of the Bragg reflector system exhibit differentiated roles *in vivo* due to their accessible, unique amino acid sequence and secondary structure. Specifically, it is possible that reflectin C can act as a "shield" to protect the structural integrity of the cellular membrane upon biological activation. Taken as such, how can we better understand the relationship and membrane active behaviors of reflectin A1 and C?

Motivated by this question, we look to further investigate the membrane active behavior of these two reflectin proteins when interacting with lamellar mesophases in the hopes of elucidating their mechanisms of interaction in real-time. First, reflectin A1 and C were aliquoted into solutions of giant unilamellar vesicles (GUVs), formed by previously-established electroformation methods, as cell-sized mimics for experimentation.[23] These semi-permeable lipidic compartments have been commonly utilized for morphological studies of biomolecule-membrane interactions due to their simple topology and possible compositional variance.[19, 182, 183] Second, reflectin A1 and C interacted with the cylindrical, smectic mesophase called the myelin figure. These multilamellar membranes, whose lamellae are stabilized by the inter-lamellar Helfrich repulsion, possess a lyotropic, layered structure which complicates morphological processes when perturbed by external dopants.[33, 71] Through this experimentation, we can better elucidate how reflectins can perturb macroscopic soft matter systems and structurally modulate the original assembly, correlating macroscopic morphogenesis with microscopic behavior.

So, reflectin-membrane interactions were monitored in real-time through the exposure of the previously mentioned lamellar membrane assemblies to reflectin A1 and C. Using previously noted electroformation and directed hydration methods, these lamellar mesophases were assembled and exposed to pH-buffered solutions of the focal proteins on wide-field fluorescence and brightfield microscopy instruments. These lipidic assemblies were composed of 1-palmitoyl-2-oleoyl-*sn*-glycero-3-

phosphocholine (POPC) and 1,2-dioleoyl-*sn*-glycero-3-phospho-(1'-rac-glycerol) (sodium salt) (DOPG) with or without a 1 mol% dopant of 1,2-dioleoyl-*sn*-glycero-3-phosphoethanolamine-*N*-(lissamine rhodamine B sulfonyl) (ammonium salt) (Rho B-DOPE) for fluorescence imaging.[18] The results presented here exhibit a concentration dependent trend of morphological development for condensed reflectin A1 that significantly perturbs the original lamellar structure. When interacting with GUVs, a 1 μM solution of reflectin A1 caused the vesicles to shrink, a 2 μM solution induced extravesicular budding, and a 30 μM solution led to the bursting of the mesophases. In contrast, when interacting with either lamellar structure reflectin C generally caused minimal behavioral variance in comparison to control experiments. We further examined the relationship between the reflectin proteins by adding different concentration ratios of C then A1 to GUVs, allowing for sufficient residence time. We hypothesized that reflectin C would "protect" the GUVs from the more aggressive reorganization caused by A1, but this was observed to be untrue as the addition of A1 still significantly perturbed the membrane assemblies. When interacting with myelin figures, the presence of higher concentrations of reflectin A1 caused the mesophases to lose lipidic material as aggregates while the tubules grew outward into the bulk solution. Through these results, we demonstrate the highly specific membrane active behaviors of reflectin A1 and C *in vitro* and elucidate the possible applications of this family of proteins.[181]

5.3. RESULTS AND DISCUSSION

Preliminary characterization of reflectin-membrane interactions began with the exposure of GUVs with simple compositions to both reflectin A1 and C. At first, GUVs were prepared with only POPC by electroformation with 1 mol% Rho B-DOPE as a dopant for fluorescence imaging. Then, GUVs were aliquoted into a 3-(*N*-morpholino)propanesulfonic acid (MOPS) pH-buffered solution of reflectin A1 or C at various concentrations and the resulting dynamics were visualized by wide-field fluorescence. Solutions of A1 and C were buffered at pH = 7.5 as the cationic segments on the reflectin proteins are neutralized in these conditions and the proteins condense significantly in a multimeric manner.[18, 177] GUVs composed of

only POPC were aliquoted into a solution with 30 μM of reflectin A1 and nothing significant occurred. These GUVs did not undergo any unique morphogenesis when exposed to 30 μM solutions of reflectin C as well. As such, these results elucidated that an electrostatic attraction between reflectin proteins and the bilayer could initiate the binding and consequential behaviors.[18] So, the composition of the GUVs was modulated to a 6:4 molar ratio of POPC:DOPG but GUVs were not formed by electroformation. The composition was then adjusted to a final molar ratio of 9:1 POPC:DOPG with 1 mol% Rho B-DOPE.

These POPC:DOPG GUVs were then aliquoted into a 30 μM solution of reflectin A1 at pH = 7.5, where vesicles burst and collapsed within 5 minutes of exposure (**Figure 5.1**). Bursting events occurred faster than 0.2 seconds (as monitored with a frame rate of 5 frames per second) while collapses took minutes to complete. Previous work has exhibited the concentration-dependent activity of reflectin A1 and C with small unilamellar vesicles (SUVs), therefore we employed various other concentrations of reflectin A1 with these GUVs.[18] POPC:DOPG GUVs were aliquoted into a solution of 5 μM reflectin A1 and similar bursting events occurred. Reducing the concentration further, POPC:DOPG GUVs were then exposed to a 2 μM solution of condensed reflectin A1. Here, the membrane was perturbed and the vesicles uniquely reorganized. Over the span of 1 minute, a source GUV formed smaller, extracellularly-budded vesicles which bound to the GUV surface (**Figure 5.2**). Such aggressive perturbation and reorganization is reminiscent of previous work, where reflectin A1 collated SUVs into macroscopic structures.[18] Continuing this trend, the concentration of A1 was reduced further in solution. POPC:DOPG GUVs exposed to 1 μM reflectin A1 shrunk radially without any macroscopically-discernible morphogenesis (**Figure 5.3**). This process occurred over the span of multiple minutes. With these preliminary characterizations of the membrane active behaviors of reflectin A1, we then explored the dynamics of reflectin C.

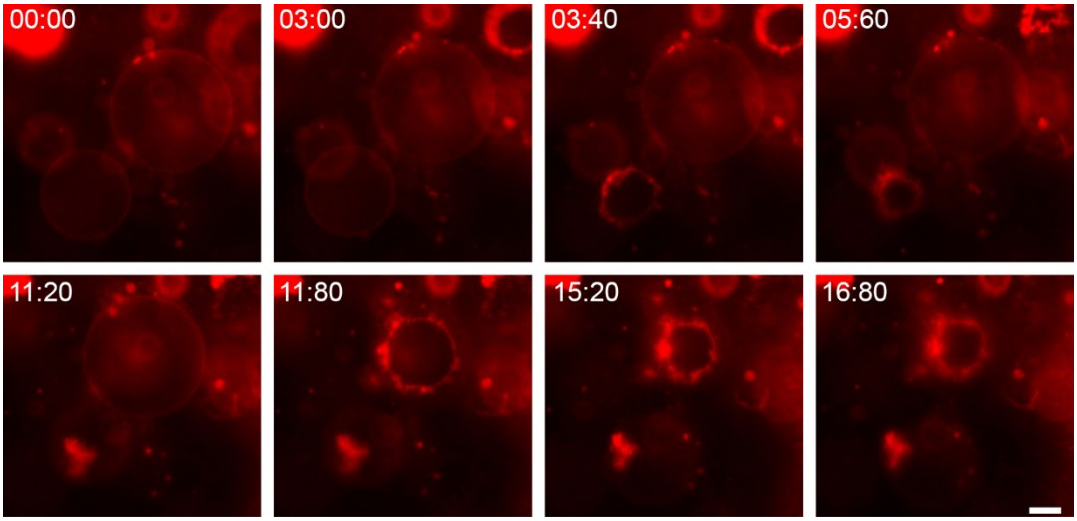

Figure 5.1. POPC:DOPG GUVs Bursting in a Solution of 30 µM Reflectin A1 at pH = 7.5. POPC:DOPG GUVs burst and collapsed when aliquoted into a solution of 30 µM reflectin A1 at pH = 7.5. Time stamp, sec:centisec; Scale bar, 20 µm.

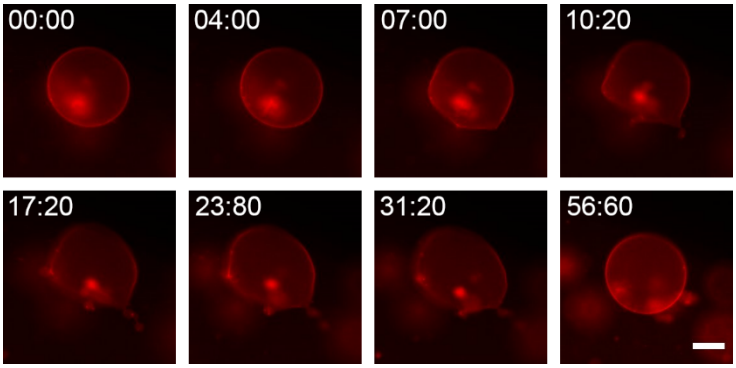

Figure 5.2. POPC:DOPG GUV Budding in a Solution of 2 μM Reflectin A1 at pH = 7.5. POPC:DOPG GUV reorganizing and budding when aliquoted into a solution of 2 μM reflectin A1 at pH = 7.5. Time stamp, sec:centisec; Scale bar, 20 μm.

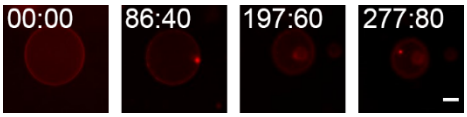

Figure 5.3. POPC:DOPG GUV Shrinking in a Solution of 1 μM Reflectin A1 at pH = 7.5. POPC:DOPG GUV shrinking when aliquoted into a solution of 1 μM reflectin A1 at pH = 7.5. Time stamp, sec:centisec; Scale bar, 20 μm.

POPC:DOPG GUVs were exposed to solutions of 30 μM reflectin C at pH = 7.5 and nothing macroscopically-significant occurred. These results, along with the immunohistochemical localization of reflectin C *in vivo*, inspired a possible hypothesis.[180] Does reflectin C binding act as a protective "shield" for the cellular membrane? POPC:DOPG GUVs were added into a solution of reflectin C and allowed a sufficient residence time of 5 min before adding a solution of reflectin A1 to the overall mixture.[18] As of our knowledge currently, stoichiometry of the proteins *in vivo* from homogenized squid tissue is approximately 5000-fold greater for C than A1 by MALDI-MS.[179] While valuable to the framework of this work, we decided to employ smaller ratios of C to A1. Future efforts can attempt to recreate this concentration ratio experimentally as small concentrations are needed (~30 μM reflectin C to 6 nM reflectin A1). First, a 1:1 molar ratio of reflectin C:A1was utilized by first aliquoting POPC:DOPG GUVs in a solution of C (with the final concentration of 30 μM) and allowing to settle for 5 min. During this time, no macroscopic morphogenesis occurred. Then, a solution of A1 was added to the mixture (for a final concentration of 30 μM) where GUVs rapidly burst within 1-2 min. This process was repeated with a similar 1:1 molar ratio but final concentrations of 5 μM reflectin C and 5 μM A1. Here, identical results were observed. 3:1 (6 μM to 2 μM), 5:1 (5 μM to 1 μM), and 10:1 (10 μM to 1 μM) molar ratios of reflectin C:A1 were investigated as well, all of which exhibited similar morphological developments of GUVs bursting and collapsing upon addition of A1. These results elucidate the destructive behaviors of reflectin A1 and dictate that the relationship between reflectin C and A1 is specifically tuned *in vivo* and model experiments must employ molar ratios closer to this 5000-fold amount.

Moving onward to the other focal lamellar mesophase, myelin figures were examined for their interactions with solely reflectin A1 or C. By depositing lipidic material between glass slides (also known as the "lipid cake"), hydration of the involved molecules can be directed and perturbing agents can be guided toward the assembling structures for surficial interactions.[33] Since condensed reflectin assemblies have been measured to be ~20 nm or larger in size by dynamic light scattering, we anticipate that proteins will not intercalate in the aqueous layer between the bilayers of the myelin figure, so any activity will be

surficial interactions.[177, 178] We began by hydrating a dried "lipid cake" of only POPC with 20 μL of a 30 μM solution of reflectin A1 buffered at pH = 7.5. The resulting dynamics were monitored by brightfield microscopy, of which no significantly different behaviors were observed. This procedure was repeated for a 30 μM solution of reflectin C buffered at pH = 7.5 and nothing of note was seen. Then, a "lipid cake" composed of a 9:1 molar ratio of POPC:DOPG lipids was hydrated with 20 μL of a 30 μM solution of reflectin A1 buffered at pH = 7.5. In result, no significantly altered behaviors occurred, therefore the concentration of A1 was increased. Repeating an identical procedure with 90 μM A1, myelin figures exhibited unique dynamics (**Figure 5.4**). At first, the tubules grew outward into the hydrating solution before entering a "frustrated" state where tubes sporadically grew outward and shrank with no predictability. Throughout this state, depositions of lipidic material were observed on the glass slide around the structures wherever they moved. From these apparent observations, reflectin A1 intercalated within the external bilayers of the myelins, removed lipidic material from those involved bilayers, and then settled and deposited this material as aggregates on the glass slide. Such "frustrated" behaviors are reminiscent of the dynamics induced by the surficial intercalation of detergents which also destroyed the myelins.[33] For comparison, hydrating this POPC:DOPG mixture with 20 μL of a 90 μM solution of reflectin C buffered at pH = 7.5 did not exhibit any similar behaviors to A1 experiments. However, coiling and helical morphologies was observed upon exposure to reflectin C (**Figure 5.5**). This morphological development occurs as a consequence of asymmetric doping of amphipathic molecules with variable curvatures and molecular packing parameters, exemplifying reflectin C's binding and intercalation into the tubules.[33] These such results further exhibit the diversified behaviors between the destructive reflectin A1 and the less aggressive reflectin C.

The intercalation, perturbation, and reorganization of macroscopic, lipidic, lamellar mesophases by the intrinsically disordered proteins reflectin A1 and C foreground numerous questions.[18] First, what causes reflectin proteins to bind and perturb membranes with different qualitative intensities? And

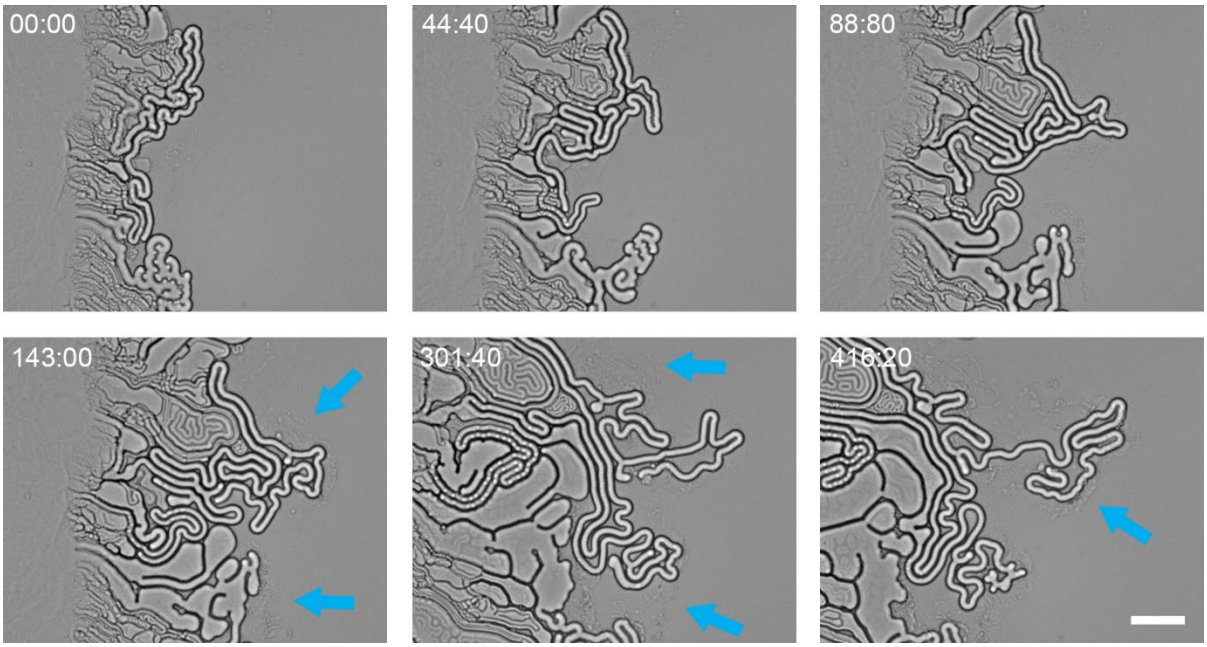

Figure 5.4. POPC:DOPG Myelin Figures Exhibiting "Frustrated" State and Losing Lipidic Material. POPC:DOPG myelin figures exhibit the "frustrated" state upon exposure to 90 μM reflectin A1. The myelin then lose externally-facing lipidic material, as indicated by the arrows. Time stamp, sec:centisec; Scale bar, 50 μm.

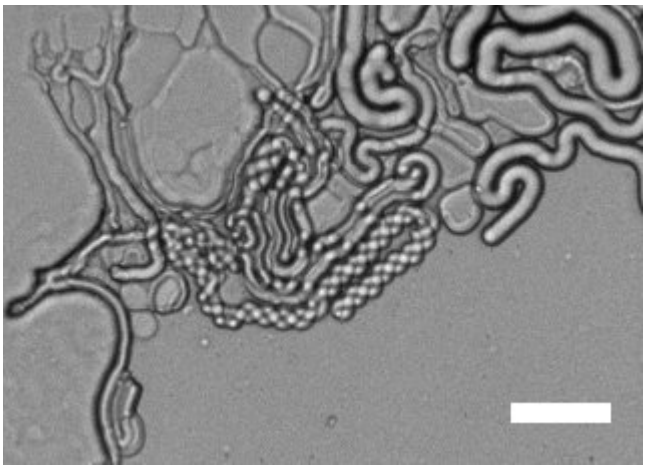

Figure 5.5. POPC:DOPG Myelin Figures Exhibiting Helical Morphogenesis. POPC:DOPG myelin figures crossing over themselves and forming helical morphologies upon exposure to 90 μM reflectin C. Scale bar, 20 μm.

what is the relationship between membrane activity and stoichiometry of the reflectin proteins? The following considerations attempt to form a conjecture on reflectin-membrane dynamics that both elucidates the chemical interactions determining membrane activity and emphasizes the evolved complexity of this proteinaceous "soup" *in vivo*.

Reflectin-membrane activity, as elucidated in previous work, most likely originates from the amino acid composition of the proteins and the possible secondary structures of which the condensed form of the proteins can assemble.[18, 177, 178] For example, reflectin proteins contain significant amounts of arginine (11%) and tyrosine (20%) throughout their sequence with a high density of histidine residues within the linker sections.[178] Arginine can bind to the interfacial region of a lamellar membrane favorably due to its hydrogen bonding ability, leading to the construction of thermodynamically favorable hydration shells, while also perturbing peptide packing within bilayers.[184, 185] Previous studies exhibited tyrosine's ability to intercalate within the hydrophobic space of a 1,2-dioleoyl-*sn*-glycero-3-phosphocholine (DOPC) bilayer around ~1.25 nm from its center, as determined by isolated molecular dynamics simulations.[17] This occurs due to the molecule's amphipathic nature and possible π-π interactions between its aromatic ring and unsaturated lipids.[17] And histidine, with an isoelectronic point of pH = ~7.5, populating the linkers of the protein sequence can electrostatically pair with the negatively-charged DOPG molecules in the lamellae as an initial attractive force to the membrane surface.[186, 187] As our results exhibit, this electrostatic attraction is an apparent necessity for the binding event to occur. The presence of these amino acids could encourage the binding, intercalation, and perturbation of lamellar membranes *in vitro* and *in vivo*.

At a higher level, the secondary folding and organization of the reflectin proteins also specifically influence their behaviors. Due to the intrinsically disordered nature of reflectin proteins, it can be difficult to predict their higher-order structures upon condensation; however, neural network-based predictions, circular dichroism spectroscopy experimentation, and calculations of net hydropathy have elucidated the potential for secondary structure formation during condensation.[177, 178] Previous work has illuminated the ubiquity of α-helices as methods of insertion into membranes, therefore the assembly of similar structures

within reflectin proteins would be marked indicators of membrane activity.[12, 15, 188] Indeed, previous work has hypothesized of the presence of transient α-helices within condensing reflectin *en route* to finalized β-structures like sheets.[177] Therefore, the highly specific membrane activity of reflectin A1 and C potentially originates from their structural considerations (since their amino acid composition is relatively similar), albeit more information on the externally-available amino acids and secondary structure is needed before confirmation.[18]

While we can percolate on the origins of membrane activity for the reflectin proteins, the question of their specific stoichiometry is far less clear to our current knowledge. As mentioned above, the apparent *in vivo* ratios between reflectin C to A1 is ~5000:1 from homogenized squid mantle tissue.[179] While helpful in inspiring experimental design, the complex mixture of various reflectin proteins and cellular content in the iridocyte platelets complicate the picture. However, recent studies have investigated the self-assembly dynamics of various reflectin proteins, providing this work with a higher amount of clarity. Primarily, previous work elicited that a delicate balance between intra- and intermolecular interactions of these biomolecules could determine multimeric assembly size as reflectin C and A1 have different sizes when condensed.[177] *In vitro*, reflectin proteins commonly assembled into isolated, spherical morphologies possibly due to the presence of amino acids which are known to participate in non-covalent liquid-liquid phase separation events.[178] So, it is possible that groups of reflectin proteins phase separate as thermodynamically favorable clusters when mixed *in vivo*, dictating local molar ratios when these families of proteins condense. As such, further experimentation is needed before any conclusions about stoichiometry can be made.

5.4. CONCLUSION

The dynamics between reflectin A1, C, and a sequential mixture of the two interacting with POPC:DOPG GUVs and myelin figures have been investigated. Real-time morphological developments were visualized by wide-field fluorescence microscopy with the fluorescent dopant Rho B-DOPE and

brightfield microscopy to understand the macroscopic consequences of their interactions. Through these examinations, we have elucidated three noteworthy points. First, condensed reflectin A1 exhibits a large potential to aggressively perturb and reorganize bilayer membranes in unique capacities. We see this through the concentration-dependent perturbations of POPC:DOPG GUVs at 1 μM (shrinking the GUVs), 2 μM (forming extravesicular buds), and 30 μM (bursting and collapsing the GUVs). Additionally, we observed that myelin figures exhibited "frustrated" states and lost lipidic material as aggregates, further exemplifying the aggressive membrane active behavior of reflectin A1. Second, condensed reflectin C exhibits a far less significant potential to disrupt bilayer membranes. This is apparent for both GUVs and myelin figures since no significant alterations in behavior experimentally occurred for the concentrations employed. Last, the relationship between reflectin A1 and C seems to be much more complex *in vivo* than explored in these *in vitro* experiments. Experimentally, qualitative morphogenesis aligned with the apparent behavior of isolated reflectin A1 exposure when molar ratios of 1:1, 3:1, 5:1, and 10:1 C:A1 were employed with sufficient residence time with GUVs. Since both biomolecules are part of a larger, specific proteinaceous mixture found in the platelets of iridocytes, further experimentation at *in vivo* molar ratios of C:A1 (closer to 5000:1) are needed before more definitive conclusions can be made. These results highlight the specific behaviors of these unique proteins and foreground the complexities of the system *in vivo*. Further examinations of this system could beget the design of valuable, light-reflecting thin film materials and synthetic recreations of these iridophores.

5.5. MATERIALS AND METHODS

Materials. 1-Palmitoyl-2-oleoyl-*sn*-glycero-3-phosphocholine (POPC), 1,2-distearoyl-*sn*-glycero-3-phospho-(1'-*rac*-glycerol) (sodium salt) (DOPG), and 1,2-dioleoyl-*sn*-glycero-3-phosphoethanolamine-*N*-(lissamine rhodamine B sulfonyl) (ammonium salt) (Rho B-DOPE) were purchased from Avanti Polar Lipids (Alabaster, Al). Chloroform, pentane, ethanol, methanol, glucose, sucrose, 3-(*N*-Morpholino)propanesulfonic acid (MOPS), sodium acetate trihydrate, glacial acetic acid, and

ethylenediaminetetraacetic acid (EDTA) disodium salt dihydrate were purchased from Sigma-Aldrich (St. Louis, MO). Base and cover boro-silicate microscope slides were obtained from Corning (Corning, NY). Nitrogen gas was acquired from Praxair (Danburt, CT). Indium tin oxide (ITO) coated glass slides (resistance 4-30 Ω) were purchased from Delta Technologies (Loveland, CO). 96-well polypropylene bottom plates were obtained from Corning (Corning, NY). All chemicals were used without further purification.

Expression, Purification, and Dialysis of Reflectin Proteins. Reflectin protein processing was implemented using previously published procedures.[177, 178] Recombinant *D. opalescens* reflectin A1 mutants were produced by mutagenesis, using standard techniques, of a nonaffinity-tagged, codon-optimized reflectin A1 WT construct cloned into a (pJ411) plasmid (ATUM, San Francisco, CA). All mutants were confirmed by DNA sequencing. All proteins were expressed in Rosetta 2 (DE3) *Escherichia coli* cells grown at 37°C in liter Luria-Bertani (LB) cultures from freshly plated transformants in the presence of 50 mg/ml kanamycin and 37 mg/ml chloramphenicol. Expression was induced at A_{600} ~0.6 and allowed to proceed for 6 hr. at 37°C, at which point cells were pelleted by centrifugation and frozen at 80 °C until ready for use. All reflectin proteins were expressed as inclusion bodies, similarly to WT, with roughly similar yields as judged by comparison on Sodium Dodecyl Sulfate (SDS) - polyacrylamide gels. Reflectin inclusion bodies were purified from cell pellets with BugBuster medium (Novagen, Inc., Madison, WI) as directed by the manufacturer. Inclusion bodies were solubilized in 5% acetic acid, 8 M urea, 6 M guanidinium hydrochloric acid followed by dialysis against 5% acetic acid, 8 M urea to remove guanidinium. Proteins were purified by ion exchange over a HiTrap XL (GE Healthcare, Chicago, IL) cation-exchange column and eluted with a gradient of 5% acetic acid, 6 M guanidinium. Fractions containing reflectin proteins were collected; diluted in 5% acetic acid, 8 M urea to lower guanidinium concentration; loaded onto a Mono S GL column (GE Healthcare, Chicago, IL); and then eluted with a step gradient of 5% acetic acid, 6 M guanidinium. Eluted reflectin proteins were concentrated, loaded onto an

HPLC reverse-phase C10 column equilibrated with 0.1% trifluoroacetic acid (TFA) in H_2O, and then eluted over a gradient of 95% acetonitrile, 0.1% TFA. Fractions were then lyophilized and stored in an 80 °C freezer until solubilization. Purity was assessed on 10% Tris acetate SDS-polyacrylamide gels (Life Technologies, Carlsbad, CA). Lyophilized pellets of reflectin A1 or C were dissolved in 25-50 μL of 10 mM acetate buffer at pH = 4.5. Then, the dissolved solutions were pipetted into 10 mm wide, 6-8 kilodaltons (kDa) molecular weight cut-off size dialysis tubing (Repligen, Waltham, MA) and dialyzed in a total of 1000x volume of 10 mM acetate buffer at pH = 4.5 for 12 hours. The dialysis solution was emptied and refilled every 4 hours with fresh buffer solution. Once the 12 hours were finished, the solution of reflectin protein was aliquoted into a new vial and brought to a Spectramax M4, single wavelength (endpoint read mode), ultraviolet visible spectroscopy instrument with the SpectraDrop Micro-Volume Microplate (Molecular Devices, San Jose, CA). The concentration of dialyzed reflectin A1 or C was found by measuring the absorbance of the proteins at 280 nm and calculated using known values of molar absorptivity for A1 (120685 M/cm) and C (16390 M/cm). All dialyzed solutions of reflectin A1 and C were stored at 4ºC when not in use, and solutions were equilibrated to room temperature before experimentation. For experimentation, dialyzed solutions of reflectin A1 and C were diluted to the correct concentration using 10 mM MOPS buffer at pH = 7.5 and tested with pH paper.

Giant Unilamellar Vesicle Preparation and Experimentation. Giant unilamellar vesicles (GUVs) were prepared using already-established techniques in electroformation.[23] Two separate stock solutions of lipids were prepared at 2 mg/ml in chloroform: (1) POPC and (2) a 9:1 molar ratio of POPC:DOPG both with 1 mol% Rho B-DOPE. Two Indium Tin Oxide (ITO) coated microscope slides were cleaned using pentane and chloroform before 15 μL of a stock solution was spread on each slide's conductive side. The slides were then allowed to dry under house vacuum for at least two hours. After drying, the film of deposited lipids was directly hydrated (~1 mL) with a 10 mM solution of sucrose and contained using a 1 mm thick rubber "O" ring (~20 mm diameter) from Ace Hardware (Davis, CA) sealed with high vacuum grease from

Dow Corning (Midland, MI). An effective water-tight "sandwich" was made by sealing the solution chamber with more vacuum grease and the second ITO-coated slide, ensuring no visible air bubbles were present inside. Using a function generator, a 4 Vpp AC sine wave was applied at 10 Hz for 1.5 hr. before a 4 Vpp AC square wave at 2 Hz for 1.5 hr. was then applied across the two slides at room temperature. During the formation, the sandwiches were covered to protect from light. After formation, the sandwiches were taken apart and the solution containing GUVs was transferred to small centrifuge tubes and either used immediately or stored at 4 °C. All GUVs were used within a week of their formation. 2 μL volumes of GUVs were aliquoted into 200 μL solutions of 10 mM MOPS buffer at pH = 7.5, 10 mM MOPS buffer at pH = 7.5 with various concentrations of reflectin A1, or 10 mM MOPS buffer at pH = 7.5 with various concentrations of reflectin C in glass-bottomed 96-well plates and mounted onto the wide-field fluorescence microscopy instrument (described below).

Myelin Preparation and Experimentation. Myelin figures were prepared by adapting a previously-reported procedure of hydrating a dried mass of phospholipid molecules between two microscope slides.[22] Two separate stock solutions were prepared at a concentration of 25 mg/ml in 9:1 (v/v) chloroform to methanol, (1) 100% POPC and (2) a 9:1 molar ratio of POPC:DOPG. Microscope slides were cleaned by sonication for 5 minutes in a bath of ethanol, dipping in chloroform for 1 second, and drying with nitrogen gas and desiccation. Small droplets (4 μL) of stock solution were placed on cleaned cover slides and the solution was allowed to dry in the atmosphere until a dried mass remained (~15 minutes). Coated cover slides and clean base slides were then pressed together into a lipid cake for 10 seconds using a Mettler Toledo (Greifensee, Switzerland) presser. Cakes were either used immediately or stored under a house vacuum and protected from prolonged exposure to ambient light. All cakes were used within a week of preparation. Lipid cakes were mounted onto the appropriate microscopy instrument, and a sharp, unobstructed edge of the dried mass was found. 20 μL of an aqueous solution was then pipetted onto the edge of the sandwich, and the solution moved into the gap by advection with the glass. Upon contact with

the dried mass, tubules of myelin figures grew outwardly into the surrounding area. The lipid cake could be hydrated with 10 mM MOPS buffer at pH = 7.5, 10 mM MOPS buffer at pH = 7.5 with various concentrations of reflectin A1, or 10 mM MOPS buffer at pH = 7.5 with various concentrations of reflectin C. All experiments were carried out at room temperature, which is above the gel-fluid phase transition temperature of all of the lipids used.

Wide-field Fluorescence Microscopy. Wide-field fluorescence microscopy images of GUVs were acquired using a Plan Fluor 20X (NA, 0.25) air objective (Nikon, Japan), a HXP 210 C mercury metal halide lamp (Carl Zeiss, Oberkochen, Germany), and filter cubes to filter absorption and emission of the source and camera. Wide-field fluorescence microscopy measurements of giant unilamellar vesicles were performed using a Nikon Eclipse TE2000S inverted fluorescence microscope (Technical Instruments, Burlingame, CA) equipped with a Roper Cool Snap CCD camera (Technical Instruments, Burlingame, CA) and Hg lamp as a light source.

Brightfield Microscopy. Brightfield microscopy measurements of myelin figures were performed using a Nikon Eclipse TE2000S inverted fluorescence microscope (Technical Instruments, Burlingame, CA) equipped with a Roper Cool Snap CCD camera (Technical Instruments, Burlingame, CA). Videos were taken using a Plan Fluor 20X (NA, 0.25) objective (Nikon, Japan).

Analysis of Myelin and GUVs. All images and videos were analyzed using the ImageJ software package. Respective morphogenesis was quantitated by manual measurements or calculations.

5.6. FUNDING AND COLLABORATORS

This work is supported by a grant from the National Science Foundation (DMR-2104123). I am grateful to my collaborators, Reid Gordon, Yahya Al Sabeh, and Prof. Daniel E. Morse for their support of the above work.

CHAPTER 6 - Proteinaceous Vesicular Coagulation: Aggregation of Giant Unilamellar Vesicles by Bacterial Growth Media (Ongoing and Future Work)

6.1. ABSTRACT

Biofilm is an exemplary system of community-oriented living. Individuals accumulate and coagulate onto a surface to form a community where biological substances can be passed around in highly efficient manners. One such component that previous research efforts have found imperative to biofilm development is the formation and passage of extracellular vesicles. While previous studies have elucidated an awareness of their contents and their importance, little is known about their behavior within biofilm matrices. So, given this inspiration, we investigate how a model biological matrix impacts vesicular behavior. Giant Unilamellar Vesicles (GUVs) were formed using common electroformation techniques and aliquoted into solutions of 2-YT, a common cell culture media acting as our model biofilm matrix, and isomolar glucose. The resulting qualitative dynamics were then visualized by confocal fluorescence microscopy. In addition, a common fluorescence recovery after photobleaching (FRAP) technique was implemented to calculate the fluidity (in the form of a diffusion coefficient) of GUVs. GUVs were composed of solely 1-palmitoyl-2-oleoyl-*sn*-glycero-3-phosphocholine (POPC) as well as a 1:2 molar ratio of POPC and cholesterol (CHOL) with a 1 mol% dopant of 1,2-dioleoyl-*sn*-glycero-3-phosphoethanolamine-*N*-(lissamine rhodamine B sulfonyl) (ammonium salt) (Rho B-DOPE) in all experiments. Once exposed to the 2-YT solution, GUVs of both compositions aggregated and adhered to one another within 1-2 min. We anticipate that this behavior originates from the binding to the membrane-active amino acids within the chemical recipe of the culture media. Vesicles exposed to solutions of 2-YT exhibited a greater immobile fraction for fluorescence recovery and we confirm here that the addition of CHOL lessens the diffusion coefficient. Taken as such, these results elucidate unique behaviors of vesicles within the model matrix and foreground implications for the efficient transportation of biological materials.

6.2. INTRODUCTION

The proliferation of microbial life is a beautiful example of community-oriented and defensible living.[189, 190] Individual bacterial organisms can accumulate into larger communities which coagulate on surfaces as biofilms.[190] These aggregated cells construct a habitable matrix which contains an incommensurable amount of self-produced biological substances, including polysaccharides, proteins, genetic material, digestive enzymes, and even lamellar vesicles.[189, 190] From these materials, communities can perform a plethora of biological functions like surface adhesion, cellular cohesion, oxidative stress management, communication, genetic adaption, and enzymatic protection, all of which promote the community's survival as a dense localization of individuals.[190-192] Such complex functionality would not be possible without biological exchange; therefore, one topic of study gaining traction within the scientific community is the purpose of lamellar vesicles within the biofilm matrix.[193-196]

Both gram-negative and gram-positive bacteria release extracellular lamellar vesicles around 20–400 nm in size which transport a multiplicity of cargo that promotes biofilm formation and antagonizes competition.[193, 194, 197-199] These vesicles are sourced and formed from the membranes of the individuals within the matrix by conserved blebbing or protein-mediated lysis.[193, 197] Experimental evidence suggested that genetically knocking out vesicle formation inhibits biofilm formation and development; however, overexpressing a gene related to vesicular production heavily enhanced biofilm formation, foregrounding their importance within these microbial communities.[193, 200] Further studies have shown that vesicular cargo is unique to the microbe's state and individuals can even exchange molecular ability to others through genetic information for defensibllity.[191, 195] Therefore, microbial extracellular vesicles seem to be vital components to the success of biofilm communities, leading us to ask the following: how do these vesicles behave within biofilm systems?

Due to the plethora of components within the biofilm matrix, it is difficult to singularize the substances and forces perturbing the extracellular vesicles. However, one family of chemicals within the matrix (as well as common bacterial culture medias) that has been rigorously examined in regard to its

membrane activity is proteinaceous content.[11, 12, 19, 201] Specifically, amino acids and peptides of various sizes have shown favorable thermodynamic interactions with lamellar membranes.[18, 202, 203] Such interactions can scale in intensity from interfacial binding and electrostatic pairing to aggressive reorganization and morphogenesis.[16-19, 184] Due to their membrane-active properties and their presence within biofilm matrices, peptides warrant themselves as worthwhile subjects of study.

Inspired by these discussions, we examined the perturbation of vesicular membranes when exposed to the bacterial cultural media 2-YT (a mixture of digested proteinaceous content from casein, sodium chloride, and yeast extract). Giant unilamellar vesicles (GUVs) were assembled using previously noted electroformation methods and visualized by confocal fluorescence microscopy when exposed to a bath of isomolar glucose or 2-YT.[23] Once settled, the resulting morphogenesis was imaged and the diffusion coefficient, a measure of a bilayer's fluidity, was calculated using a fluorescence recovery after photobleaching (FRAP) technique. GUVs had varied compositions of 1-palmitoyl-2-oleoyl-*sn*-glycero-3-phosphocholine (POPC) and cholesterol (CHOL) with a 1 mol% dopant of 1,2-dioleoyl-*sn*-glycero-3-phosphoethanolamine-*N*-(lissamine rhodamine B sulfonyl) (ammonium salt) (Rho B-DOPE) for fluorescence imaging. The results presented below exhibit three prominent observations. First, the calculated diffusion coefficients exhibit a loss of the fluidity of the lamellae by the presence of cholesterol, which is experimentally known to be generally true for fluid-phase lamellae.[204, 205] Second, there was a larger immobile fraction for the diffusion coefficient of GUVs exposed to the 2-YT bath. Third, GUVs coagulated within the 2-YT bath regardless of composition and their resulting diffusion coefficients possessed similar values to their isolated relatives. Such results demonstrate unique dynamics of vesicles and elucidate possible transportation mechanisms of materials within the matrix of biofilm communities.

6.3. RESULTS AND DISCUSSION

We begin by establishing the basal dynamics of fluid-phase GUVs composed of the phospholipid 1-palmitoyl-2-oleoyl-*sn*-glycero-3-phosphocholine (POPC). These vesicular membranes were doped with

1 mol% of the fluorescently-tagged lipid 1,2-dioleoyl-*sn*-glycero-3-phosphoethanolamine-*N*-(lissamine rhodamine B sulfonyl) (ammonium salt) (Rho B-DOPE) for visualization by confocal fluorescence microscopy. GUVs were aliquoted into an isomolar (300 mM) solution of glucose and imaged. As expected, vesicles diffused within the bath before settling still as individuals. Upon settling, the diffusion coefficient of the lamellar membrane was quantitated using a common fluorescence recovery after photobleaching (FRAP) technique (**Figure 6.1**). The resulting value of 0.79 $\mu m^2/s$ (n=1) was calculated for these POPC GUVs, within an order of magnitude of literature values.[206] After this, POPC GUVs were then exposed to the 2-YT media in a similar manner and the diffusion coefficient of an isolated individual was quantitated. In this solution, the diffusion coefficient was calculated to be 1.39 $\mu m^2/s$ (n=1), a 76% increase. From these calculations, we can determine the immobile fractions of these membrane compositions. When exposed to the solution of glucose the immobile fraction of the POPC GUVs was 9.87% (n=1), however the immobile fraction was 28.9% (n=1) for the POPC GUVs within the 2-YT solution.

For comparative analysis we decided to modulate the composition of our subject GUVs by the addition of cholesterol (CHOL). These new GUVs were composed of a 1:2 molar ratio of POPC/CHOL with the 1 mol% fluorescent dopant of Rho B-DOPE. When subjected to FRAP techniques, we quantitated their diffusion coefficients within similar glucose and 2-YT solutions. The resulting values of 0.070 $\mu m^2/s$ (n=1) and 0.089 $\mu m^2/s$ (n=1) were calculated for the glucose and 2-YT solutions respectively, this decrease was expected from past studies upon the addition of CHOL.[204, 205] Even with the majority amount of CHOL within the bilayers,

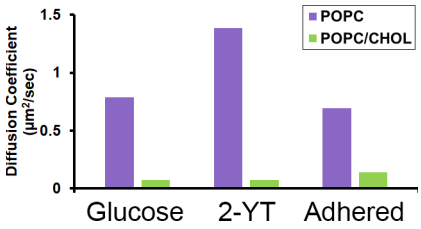

Figure 6.1. Calculated Diffusion Coefficients of POPC and POPC/CHOL GUVs within Glucose and 2-YT Solutions. Using confocal fluorescence microscopy, the diffusion coefficient for all permutations of POPC and POPC/CHOL GUVs within glucose and 2-YT solutions were calculated (n=1). Addition of cholesterol severely decreased the value of the diffusion coefficient while the adherence of GUVs did not significantly impact the membrane's fluidity.

fluorescence recovery plots still exhibited familiar trends for GUVs with both solutions (**Figure 6.2 and 6.3**). Again, the immobile fractions of these membranes can be consequentially quantitated. The immobile fractions were calculated as 8.42% (n=1) and 20.2% (n=1) for the GUVs in the glucose solution and 2-YT solution respectively. Notedly, the fluorescence recovery plots of both POPC and POPC/CHOL GUVs within both solutions expressed familiar trends, meaning the contents of 2-YT did not entirely inhibit lateral lipid movement within the bilayer but did incur a higher immobile fraction.

Within the time of settling (~1-2 min), both POPC and POPC/CHOL GUVs aliquoted into the bath with 2-YT began to adhere to one another (**Figure 6.4**). These adherence events could include a multitude of vesicles with different sizes or just two partners. Notably, the lipids participating within the adhered regions as well as their surrounding neighbors still possessed their fluidity, meaning that FRAP techniques could be applied to these vesicular aggregates. Specifically, the area of contact was subjected to the intensified laser light and the diffusion coefficient was quantitated for the contact patch (**Figure 6.5**). The resulting values for both POPC and POPC/CHOL GUVs were calculated to be 0.69 $\mu m^2/s$ (n=1) and 0.14 $\mu m^2/s$ (n=1) respectively, which is similar to the values of non-adhered GUVs. Notedly, the immobile fractions of the bilayers were quite different from non-adhered GUVs: the immobile fraction of the adhered POPC GUVs was 18.3% (n=1) and the immobile fraction of the adhered POPC/CHOL GUVs was 5.16% (n=1).

Given these observations of trends in fluidity and the morphogenesis of GUVs within 2-YT solutions, we must consider the behaviors of the components within the bath. 2-YT can best be described as a chemical “soup” filled with various biological molecules from a digested form of casein, sodium chloride, and yeast extract. This mixture includes mostly amino acids, ionic salts, and saccharides with smaller amounts of lipids and minerals. As such, it is important to highlight the membrane-active properties of the participating molecules, being the proteinaceous content, in 2-YT.

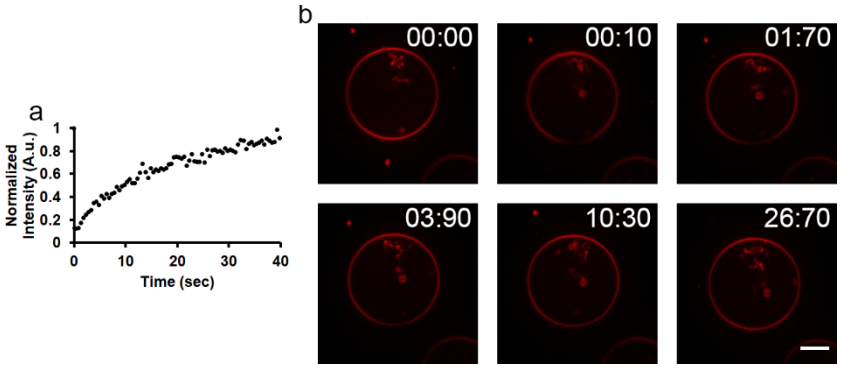

Figure 6.2. FRAP of POPC/CHOL GUV in a Glucose Solution. (a) The resulting fluorescence intensity recovery was plotted over time for a POPC/CHOL GUV. (b) The GUV was monitored over time after photobleaching and the time-lapse depiction shows its fluorescence recovery. Time stamp, sec:centisec; Scale bar, 10 μm.

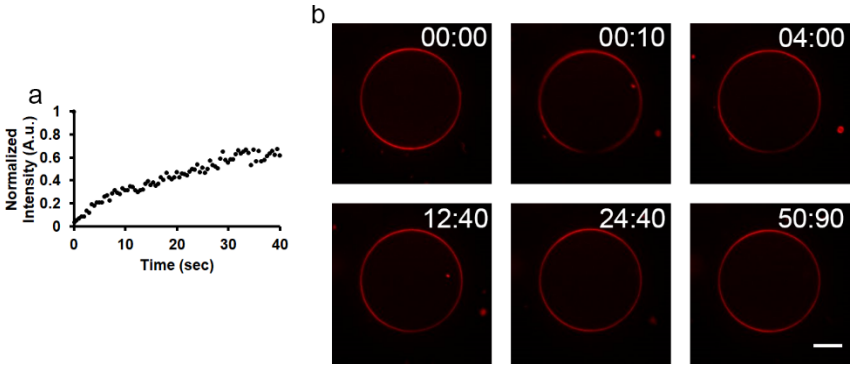

Figure 6.3. FRAP of POPC/CHOL GUV in a 2-YT Solution. (a) The resulting fluorescence intensity recovery was plotted over time for a POPC/CHOL GUV. (b) The GUV was monitored over time after photobleaching and the time-lapse depiction shows its fluorescence recovery. Time stamp, sec:centisec; Scale bar, 10 μm.

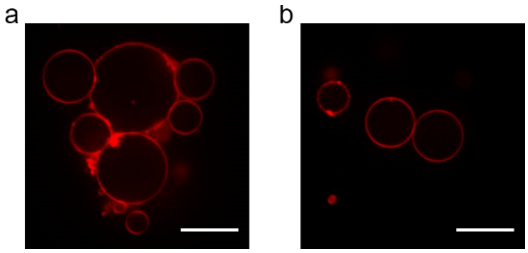

Figure 6.4. Adhered GUVs in a 2-YT Solution. (a) A multitude of variably-sized POPC GUVs adhered to one another when aliquoted into a 2-YT solution. Scale bar, 20 µm. (b) POPC/CHOL GUVs adhered to one another in a 2-YT solution. Scale bar, 20 µm.

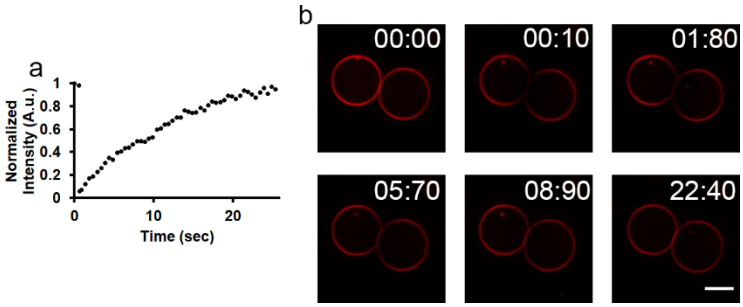

Figure 6.5. FRAP of Adhered POPC/CHOL GUVs in a 2-YT Solution. (a) The resulting fluorescence intensity recovery was plotted over time for the contact patch between POPC/CHOL GUVs. (b) The GUVs were monitored over time after photobleaching and the time-lapse depiction shows its fluorescence recovery. Time stamp, sec:centisec; Scale bar, 10 μm.

From chemical suppliers, 2-YT contains digested casein (tryptone) and yeast extract, both of which contain several membrane-active amino acids such as glutamic acid, arginine, tyrosine, and tryptophan.[207-209] Previous scientific efforts have elucidated the potential for membrane perturbation from digested protein, as breaking apart the peptides can release previously buried amphipathic components which can interact with and aggregate vesicles.[18] Therefore, understanding the behaviors of the above amino acids is imperative to hypothesize what perturbed the GUVs. Theoretical studies have previously highlighted the thermodynamic complexities of the interactions between amino acid side chains and bilayer membranes, where binding is correlated with charge.[17] For example, charged amino acids possess varying values of pKa with depth in the bilayer and lipid composition due to the hydrophobicity of their environment.[17, 202, 203] However, amino acids found within transmembrane helices can minimally impact membrane structure with changes in protonation due to their existent hydration shell.[202] Therefore, we focus on the impacts of individual amino acids on a bilayer membrane as these studies are likely more representative of digested protein. A multitude of amino acids experience an energetic minimum at the bilayer-water interface due to their binding mechanism.[16, 184, 185] For example, arginine can cluster phosphates and a hydration shell at the membrane interface effectively due to its hydrogen bonding capacity.[184] As another example, tryptophan can act like a membrane anchor at the water-bilayer interface due to its active hydrogen-bonding network and cation-π interactions between the indole group and the other phospholipid headgroups.[16] On a larger scale, tryptophan can dictate the dynamics of hydrophobic mismatch between lipids and the substituents within a transmembrane helix due to its interfacial binding.[16] With these such interactions, it is facile to believe that already bound amino acids like arginine and tryptophan within digested peptides can recruit other vesicular membranes to adhere to one another due to their interfacial membrane-active properties.

6.4. CONCLUSION

The exposure of POPC and POPC/CHOL GUVs to both isomolar glucose and 2-YT culture media solutions were visualized by the fluorescently-tagged lipid Rho B-DOPE using confocal fluorescence

microscopy. As such, the resulting morphogenesis and fluidity were determined. From these experiments, we can comment on three topics. First, the fluidity of POPC GUVs were much greater than POPC/CHOL GUVs, as expected from previous scientific efforts. Specifically, the diffusion coefficient of the POPC GUVs were 0.79 $\mu m^2/s$ (n=1) and 1.39 $\mu m^2/s$ (n=1) for glucose and 2-YT solutions respectively, while POPC/CHOL GUVs possessed values of 0.070 $\mu m^2/s$ (n=1) and 0.089 $\mu m^2/s$ (n=1) for the same solutions. Second, GUVs exposed to 2-YT solutions exhibited a larger immobile fraction in comparison to similar GUVs in glucose solutions. For example, POPC GUVs exhibited an immobile fraction of 28.9% in the 2-YT solution while only 9.87% in the glucose solution. Third, GUVs aggregated and adhered to one another within the 2-YT solution and exhibited comparatively similar values of diffusion coefficients to their isolated counterparts. These results highlight the unique characteristics of biological dopants perturbing lamellar bilayers and hypothesize the possible dynamics of extracellular vesicles within biofilm matrices. We suggest that the contents of the biofilm matrix can similarly aggregate vesicles for more efficient transportation amongst the community.

6.5. MATERIALS AND METHODS

Materials. 1-Palmitoyl-2-oleoyl-*sn*-glycero-3-phosphocholine (POPC), 1,2-dioleoyl-*sn*-glycero-3-phosphoethanolamine-*N*-(lissamine rhodamine B sulfonyl) (ammonium salt) (Rho B-DOPE), and cholesterol (CHOL) were purchased from Avanti Polar Lipids (Alabaster, Al). Chloroform, pentane, glucose, and sucrose were purchased from Sigma-Aldrich (St. Louis, MO). 2-YT broth was purchased from Thermo-Fisher Scientific (Waltham, MA). Indium tin oxide (ITO) coated glass slides (resistance 4-30 Ω) were purchased from Delta Technologies (Loveland, CO). 96-well polypropylene bottom plates were obtained from Corning (Corning, NY). All chemicals were used without further purification.

Giant Unilamellar Vesicle Preparation. Giant unilamellar vesicles (GUVs) were prepared using already-established techniques in electroformation.[23] Two separate stock solutions of lipids were prepared at 2

mg/ml in chloroform: (1) POPC and (2) a 1:2 molar ratio of POPC to cholesterol both with 1 mol% Rho B-DOPE. Two Indium Tin Oxide (ITO) coated microscope slides were cleaned using pentane and chloroform before 15 μL of a stock solution was spread on each slide's conductive side. The slides were then allowed to dry under house vacuum for at least two hours. After drying, the film of deposited lipids was directly hydrated with a 300 mM solution of sucrose (~1 mL) and contained using a 1 mm thick rubber "O" ring (~20 mm diameter) from Ace Hardware (Davis, CA) sealed with high vacuum grease from Dow Corning (Midland, MI). An effective water-tight "sandwich" was made by sealing the solution chamber with more vacuum grease and the second ITO-coated slide, ensuring no visible air bubbles were present inside. Using a function generator, a 4 Vpp AC sine wave was applied at 10 Hz for 1.5 hr. before a 4 Vpp AC square wave at 2 Hz for 1.5 hr. was then applied across the two slides at room temperature. During the formation, the sandwiches were covered to protect from light. After formation, the sandwiches were taken apart and the solution containing GUVs was transferred to small centrifuge tubes and either used immediately or stored at 4 °C. All GUVs were used within a week of their formation.

Spinning Disk Confocal Fluorescence Microscopy Experimentation. Spinning disk confocal fluorescence microscopy visualizations were performed using an Intelligent Imaging Innovations Marianas Digital Microscopy Workstation (3i, Denver, CO) with a CSU-X1 spinning disk head (Yokogawa Musashino-sh, Tokyo, Japan) and a Quantem512SC EMCCD camera (Photometrics, Tuscon, AZ). Fluorescence micrographs were obtained with oil immersion objectives (Zeiss Fluor 40x [NA 1.3], Zeiss Plan-Fluor 63x [NA 1.4], and Zeiss Fluor 100X [NA 1.46]; Carl Zeiss, Oberkochen, Germany). GUVs were prepared as described in the previous section. 2 μL volumes of GUVs were aliquoted into 200 μL solutions of 300 mM glucose or 2-YT media in glass-bottomed 96-well plates and mounted onto the microscope. After covering the objective with oil, the objectives were raised to form a meniscus between the well plate and the objective. Rho B-DOPE (Ex/Em; 560/583) was exposed with a 50 mW 561 laser line. The images

are subsequently analyzed using ImageJ software and Slidebook digital microscopy imaging software (3i, Denver, CO).

Fluorescence Recovery After Photobleaching Performance and Analysis. Fluorescence recovery after photobleaching (FRAP) experiments were performed using the same confocal fluorescence microscopy system as described above. A typical experiment begins when GUVs were brought into focus on their approximate midplane or contacting surfaces. The region of interest was selected on the Slidebook digital microscopy imaging software and the power of the Rho B-DOPE laser line was intensified for 1 second. Micrographs of fluorescence intensity signal recovery were obtained using the same oil-immersion objectives as described above. The resulting images were processed using ImageJ software and Slidebook software, then fluorescence recovery (normalized to the background) was computed using Microsoft Excel software (Redmond, WA).

6.6. FUNDING AND COLLABORATORS

This work is supported by a grant from the National Science Foundation (DMR-2104123). The 3i Marianas spinning disk confocal fluorescence instrument used in these studies was purchased using a NIH Shared Instrumentation Grant (1S10RR024543-01). I thank the Department of Molecular and Cellular Biology Light Microscopy Imaging Facility, which is a UC Davis Campus Core Research Facility, for the use of this microscope. I am grateful to my collaborators, Dr. Ting Gong and Prof. Cheemeng Tan for their support of the above work.

REFERENCES

1. Marth, J. A., A unified vision of the building blocks of life. *Nature Cell Biology* **2008,** *10* (9), 1015-1016.
2. May, S., Theories on structural perturbations of lipid bilayers. *Current Opinion in Colloid & Interface Science* **2000,** *5*, 244-249.
3. Singer, S. J.; Nicolson, G. L., The Fluid Mosaic Model of the Structure of Cell Membranes. *Science* **1972,** *175* (4023), 720-731.
4. Nicolson, G. L., The Fluid-Mosaic Model of Membrane Structure: still relevant to understanding the structure, function and dynamics of biological membranes after more than 40 years. *Biochimica et Biophysica Acta* **2014,** *1838* (6), 1451-1466.
5. Heerklotz, H., Interactions of surfactants with lipid membranes. *Q Rev Biophys* **2008,** *41* (3-4), 205-264.
6. Helenius, A.; Simons, K., Solubilization of Membranes by Detergents. *Biochimica et Biophysica Acta* **1975,** *415*, 29-79.
7. Nomura, F.; Nagata, M.; Inaba, T.; Hiramatsu, H.; Hotani, H.; Takiguchi, K., Capabilities of liposomes for topological transformation. *Proceedings of the National Academy of Sciences of the United States of America* **2001,** *98* (5), 2340-2345.
8. Heerklotz, H.; Binder, H.; Lantzsch, G.; Klose, G.; Blume, A., Lipid/Detergent Interaction Thermodynamics as a Function of Molecular Shape. *J. Phys. Chem. B* **1997,** *101*, 639-645.
9. Hamada, T.; Hagihara, H.; Morita, M.; Vestergaard, M. C.; Tsujino, Y.; Takagi, M., Physicochemical Profiling of Surfactant-Induced Membrane Dynamics in a Cell-Sized Liposome. *J Phys Chem Lett* **2012,** *3* (3), 430-435.
10. Nazari, M.; Kurdi, M.; Heerklotz, H., Classifying surfactants with respect to their effect on lipid membrane order. *Biophysical Journal* **2012,** *102* (3), 498-506.
11. Avci, F. G.; Akbulut, B. S.; Ozkirimli, E., Membrane Active Peptides and Their Biophysical Characterization. *Biomolecules* **2018,** *8* (3).
12. Cymer, F.; von Heijne, G.; White, S. H., Mechanisms of integral membrane protein insertion and folding. *J Mol Biol* **2015,** *427* (5), 999-1022.
13. Engel, A.; Gaub, H. E., Structure and mechanics of membrane proteins. *Annu Rev Biochem* **2008,** *77*, 127-148.
14. Cho, W.; Stahelin, R. V., Membrane-protein interactions in cell signaling and membrane trafficking. *Annu Rev Biophys Biomol Struct* **2005,** *34*, 119-151.
15. von Heijne, G., Membrane-protein topology. *Nat Rev Mol Cell Biol* **2006,** *7* (12), 909-918.
16. de Jesus, A. J.; Allen, T. W., The role of tryptophan side chains in membrane protein anchoring and hydrophobic mismatch. *Biochimica et Biophysica Acta* **2013,** *1828* (2), 864-876.
17. MacCallum, J. L.; Bennett, W. F.; Tieleman, D. P., Distribution of amino acids in a lipid bilayer from computer simulations. *Biophysical Journal* **2008,** *94* (9), 3393-3404.
18. Song, J.; Levenson, R.; Santos, J.; Velazquez, L.; Zhang, F.; Fygenson, D.; Wu, W.; Morse, D. E., Reflectin Proteins Bind and Reorganize Synthetic Phospholipid Vesicles. *Langmuir* **2020,** *36* (10), 2673-2682.
19. Bansal, S.; Su, W. C.; Budamagunta, M.; Xiao, W.; Ajena, Y.; Liu, R.; Voss, J. C.; Carney, R. P.; Parikh, A. N.; Lam, K. S., Discovery and mechanistic characterization of a structurally-unique membrane active peptide. *Biochimica et Biophysica Acta - Biomembranes* **2020,** *1862* (10), 183394.

20. Tamba, Y.; Yamazaki, M., Single Giant Unilamellar Vesicle Method Reveals Effect of Antimicrobial Peptide Magainin 2 on Membrane Permeability. *Biochemistry* **2005,** *44*, 15823-15833.
21. Dehsorkhi, A.; Castelletto, V.; Hamley, I. W.; Seitsonen, J.; Ruokolainen, J., Interaction between a cationic surfactant-like peptide and lipid vesicles and its relationship to antimicrobial activity. *Langmuir* **2013,** *29* (46), 14246-14253.
22. Zou, L. N., Myelin figures: the buckling and flow of wet soap. *Phys Rev E Stat Nonlin Soft Matter Phys* **2009,** *79* (6 Pt 1), 061502.
23. Angelova, M. I.; Dimitrov, D. S., Liposome Electroformation. *Faraday Discuss. Chem. Soc.* **1986,** *81*, 303-311.
24. Tayebi, L.; Ma, Y.; Vashaee, D.; Chen, G.; Sinha, S. K.; Parikh, A. N., Long-range interlayer alignment of intralayer domains in stacked lipid bilayers. *Nature Materials* **2012,** *11* (12), 1074-1080.
25. Virchow, R., Ueber das ausgebreitete Vorkommen einer dem Nervenmark analogen Substanz in den thierischen Geweben. *Archiv für pathologische Anatomie und Physiologie und für klinische Medicin* **1854,** *6*, 562-572.
26. Boullerne, A. I., The history of myelin. *Exp Neurol* **2016,** *283* (Pt B), 431-445.
27. Sakurai, I.; Kawamura, Y.; Sakurai, T.; Ikegami, A.; Seto, T., Morphology and Growth Behaviour of Myelin Figures of Lecithin. *Molecular Crystals and Liquid Crystals* **1986,** *130* (3-4), 203-222.
28. Sakurai, I.; Suzuki, T.; Sakurai, S., Cross-sectional view of myelin figures. *Biochimica et Biophysica Acta* **1989,** *985*, 101-105.
29. Buchanan, M.; Egelhaaf, S. U.; Cates, M. E., Dynamics of Interface Instabilities in Nonionic Lamellar Phases. *Langmuir* **2000,** *16*, 3718-3726.
30. Benkowska-Biernacka, D.; Smalyukh, II; Matczyszyn, K., Morphology of Lyotropic Myelin Figures Stained with a Fluorescent Dye. *J Phys Chem B* **2020,** *124* (52), 11974-11979.
31. Kennedy, A. P.; Sutcliffe, J.; Cheng, J. X., Molecular composition and orientation in myelin figures characterized by coherent anti-stokes Raman scattering microscopy. *Langmuir* **2005,** *21* (14), 6478-6486.
32. Stoeckenius, W., AN ELECTRON MICROSCOPE STUDY OF MYELIN FIGURES. *Journal of Biophysical and Biochemical Cytology* **1959,** *5* (3), 491-500.
33. Speer, D. J.; Ho, J. C. S.; Parikh, A. N., Surfactant-Mediated Solubilization of Myelin Figures: A Multistep Morphological Cascade. *Langmuir* **2022,** *38*, 8805-8816.
34. Novakova, E.; Giewekemeyer, K.; Salditt, T., Structure of two-component lipid membranes on solid support: an x-ray reflectivity study. *Phys Rev E Stat Nonlin Soft Matter Phys* **2006,** *74* (5 Pt 1), 051911.
35. Safinya, C. R.; Roux, D.; Smith, G. S.; Sinha, S. K.; Dimon, P.; Clark, N. A.; Bellocq, A. M., Steric interactions in a model multimembrane system: A synchrotron x-ray study. *Phys Rev Lett* **1986,** *57* (21), 2718-2721.
36. Sirota, E. B.; Smith, G., S.; Safinya, C. R.; Plano, R. J.; Clark, N. A., X-ray Scattering Studies of Aligned, Stacked Surfactant Membranes. *Science* **1988,** *242* (4884), 1406-1409.
37. Vogel, M.; Münster, C.; Fenzl, W.; Salditt, T., Thermal Unbinding of Highly Oriented Phospholipid Membranes. *Physical Review Letters* **2000,** *84* (2), 390-393.

38. Spaar, A.; Salditt, T., Short Range Order of Hydrocarbon Chains in Fluid Phospholipid Bilayers Studied by X-Ray Diffraction from Highly Oriented Membranes. *Biophysical Journal* **2003,** *85*, 1576-1584.
39. Su, W. C.; Gettel, D. L.; Chabanon, M.; Rangamani, P.; Parikh, A. N., Pulsatile Gating of Giant Vesicles Containing Macromolecular Crowding Agents Induced by Colligative Nonideality. *J Am Chem Soc* **2018,** *140* (2), 691-699.
40. Walde, P.; Cosentino, K.; Engel, H.; Stano, P., Giant vesicles: preparations and applications. *Chembiochem* **2010,** *11* (7), 848-865.
41. Israelachvili, J. N.; Mitchell, D. J.; Ninham, B. W., THEORY OF SELF-ASSEMBLY OF HYDROCARBON AMPHIPHILES INTO MICELLES AND BILAYERS. *Journal of the Chemical Society-Faraday Transactions Ii* **1976,** *72*, 1525-1568.
42. Israelachvil, J., Self-Assembly in Two Dimensions: Surface Micelles and Domain Formation in Monolayers. *Langmuir* **1994,** *10*, 3774-3781.
43. Israelachvil, J. N., *Intermolecular and Surface Forces, 3rd Edition*. Academic Press: Cambridge, MA, 2011.
44. Chandler, D., Interfaces and the driving force of hydrophobic assembly. *Nature* **2005,** *437* (7059), 640-647.
45. Keegstra, K.; Cline, K., Protein Import and Routing Systems of Chloroplasts. *The Plant Cell* **1999,** *11*, 557-570.
46. Schmitz, G.; Müller, G., Structure and function of lamellar bodies, lipid-protein complexes involved in storage and secretion of cellular lipids. *J Lipid Res* **1991,** *32* (10), 1539-1570.
47. Gellerich, F. N.; Trumbeckaite, S.; Opalka, J. R.; Seppet, E.; Rasmussen, H. N.; Neuhoff, C.; Zierz, S., Function of the mitochondrial outer membrane as a diffusion barrier in health and diseases. *Biochemical Society Transactions* **2000,** *28*, 164-169.
48. Sakurai, I.; Kawamura, Y.; Sakurai, T.; Ikegami, A.; Seto, T., MORPHOLOGY AND GROWTH-BEHAVIOR OF MYELIN FIGURES OF LECITHIN. *Molecular Crystals and Liquid Crystals* **1985,** *130* (3-4), 203-222.
49. Thorn, K., A quick guide to light microscopy in cell biology. *Mol Biol Cell* **2016,** *27* (2), 219-222.
50. Combs, C. A., Fluorescence microscopy: a concise guide to current imaging methods. *Curr Protoc Neurosci* **2010,** *Chapter 2*, Unit2 1.
51. Lakowicz, J. R., *Principles of Fluorescence Spectroscopy*. 3 ed.; Springer: New York, NY, 2006.
52. Elliott, A. D., Confocal Microscopy: Principles and Modern Practices. *Curr Protoc Cytom* **2020,** *92* (1), e68.
53. Ben-Shaul, A.; Gelbart, W. M., THEORY OF CHAIN PACKING IN AMPHIPHILIC AGGREGATES. *Annu Rev Phys Chem* **1985,** *36*, 179-211.
54. Nagarajan, R.; Ruckenstein, E., THEORY OF SURFACTANT SELF-ASSEMBLY - A PREDICTIVE MOLECULAR THERMODYNAMIC APPROACH. *Langmuir* **1991,** *7* (12), 2934-2969.
55. Lichtenberg, D., Characterization of the solubilization of lipid bilayers by surfactants. *Biochimica et Biophysica Acta* **1985,** *821*, 470-478.
56. Ngassam, V. N.; Howland, M. C.; Sapuri-Butti, A.; Rosidi, N.; Parikh, A. N., A comparison of detergent action on supported lipid monolayers and bilayers. *Soft Matter* **2012,** *8* (14), 3734-3738.

57. Urbaneja, M. A.; Alonso, A.; Gonzalezmanas, J. M.; Goni, F. M.; Partearroyo, M. A.; Tribout, M.; Paredes, S., DETERGENT SOLUBILIZATION OF PHOSPHOLIPID-VESICLES - EFFECT OF ELECTRIC CHARGE. *Biochemical Journal* **1990,** *270* (2), 305-308.
58. Lichtenberg, D.; Robson, R. J.; Dennis, E. A., SOLUBILIZATION OF PHOSPHOLIPIDS BY DETERGENTS - STRUCTURAL AND KINETIC ASPECTS. *Biochimica et Biophysica Acta* **1983,** *737*, 285-304.
59. Chabanon, M.; Rangamani, P., Solubilization kinetics determines the pulsatory dynamics of lipid vesicles exposed to surfactant. *Biochimica et Biophysica Acta - Biomembranes* **2018,** *1860* (10), 2032-2041.
60. Bordier, C., PHASE-SEPARATION OF INTEGRAL MEMBRANE-PROTEINS IN TRITON X-114 SOLUTION. *J Biol Chem* **1981,** *256* (4), 1604-1607.
61. Seddon, A. M.; Curnow, P.; Booth, P. J., Membrane proteins, lipids and detergents: not just a soap opera. *Biochimica Et Biophysica Acta - Biomembranes* **2004,** *1666* (1-2), 105-117.
62. Garavito, R. M.; Ferguson-Miller, S., Detergents as tools in membrane biochemistry. *J Biol Chem* **2001,** *276* (35), 32403-32406.
63. Silvius, J. R., SOLUBILIZATION AND FUNCTIONAL RECONSTITUTION OF BIOMEMBRANE COMPONENTS. *Annu Rev Biophys Biomol Struct* **1992,** *21*, 323-348.
64. London, E.; Brown, D. A., Insolubility of lipids in Triton X-100: physical origin and relationship to sphingolipid/cholesterol membrane domains (rafts). *Biochimica et Biophysica Acta* **2000**, 182-195.
65. Brown, D. A.; London, E., Structure and function of sphingolipid- and cholesterol-rich membrane rafts. *J Biol Chem* **2000,** *275* (23), 17221-17224.
66. Ahmed, S. N.; Brown, D. A.; London, E., On the Origin of Sphingolipid/Cholesterol-Rich Detergent-Insoluble Cell Membranes: Physiological Concentrations of Cholesterol and Sphingolipid Induce Formation of a Detergent-Insoluble, Liquid-Ordered Lipid Phase in Model Membranes. *Biochemistry* **1997,** *36*, 10944-10953.
67. Lichtenberg, D.; Ahyayauch, H.; Goni, F. M., The mechanism of detergent solubilization of lipid bilayers. *Biophysical Journal* **2013,** *105* (2), 289-299.
68. Kragh-Hansen, U.; le Maire, M.; Moller, J. V., The mechanism of detergent solubilization of liposomes and protein-containing membranes. *Biophysical Journal* **1998,** *75* (6), 2932-2946.
69. Toyota, T.; Tsuha, H.; Yamada, K.; Takakura, K.; Yasuda, K.; Sugawara, T., Fluorescence Microscopic Investigation on Morphological Changes of Giant Multilamellar Vesicles Induced by Amphiphilic Additives. *Langmuir* **2006,** *22*, 1976-1981.
70. Sudbrack, T. P.; Archilha, N. L.; Itri, R.; Riske, K. A., Observing the Solubilization of Lipid Bilayers by Detergents with Optical Microscopy of GUVs. *J. Phys. Chem. B* **2011,** *115*, 269-277.
71. Lis, L. J.; McAlister, M.; Fuller, N.; Rand, R. P.; Parsegian, V. A., Interactions Between Neutral Phospholipid Bilayer Membranes. *Biophysical Journal* **1982,** *37*, 657-666.
72. Tsafrir, I.; Guedeau-Boudeville, M. A.; Kandel, D.; Stavans, J., Coiling instability of multilamellar membrane tubes with anchored polymers. *Phys Rev E Stat Nonlin Soft Matter Phys* **2001,** *63* (3 Pt 1), 031603.
73. Lee, Y. C.; Baath, J. A.; Bastle, R. M.; Bhattacharjee, S.; Cantoria, M. J.; Dornan, M.; Gamero-Estevez, E.; Ford, L.; Halova, L.; Kernan, J.; Kurten, C.; Li, S. R.; Martinez,

J.; Sachan, N.; Sarr, M.; Shan, X. W.; Subramanian, N.; Rivera, K.; Pappin, D.; Lin, S. H., Impact of Detergents on Membrane Protein Complex Isolation. *J Proteome Res* **2018,** *17* (1), 348-358.
74. Kum, S. L.; Ho, J. C. S.; Parikh, A. N.; Liedberg, B., Amphiphilic Membrane Environments Regulate Enzymatic Behaviors of Salmonella Outer Membrane Protease. *ACS Bio & Med Chem Au* **2022,** *2* (1), 73-83.
75. Nollstadt, K. H.; Karkhanis, Y. D.; Gnozzio, M. J.; Crane, M. S. J.; Gurnett, A. M.; Schmatz, D. M.; Turner, M. J., POTENTIAL OF THE SULFOBETAINE DETERGENT ZWITTERGENT 3-12 AS A DESORBING AGENT IN BIOSPECIFIC AND BIOSELECTIVE AFFINITY CHROMATOGRAPHY. *J Chromatogr* **1989,** *497*, 87-100.
76. Church, W. R.; Ebner, K. E., Solubilization of prolactin receptor by a Zwitterionic detergent. *Experientia* **1982,** *38* (4), 434-435.
77. Ho, J. C. S.; Su, W.-C.; Chun Wang, X.; Parikh, A. N.; Liedberg, B., Non-equilibrium Self-organization of Lipids into Hierarchically Ordered and Compositionally Graded Cylindrical Smectics. *Langmuir* **2022,** *38* (3), 1045-1056.
78. Ostwald, W., Studien über die Bildung und Umwandlung fester Körper. *Zeitschrift für physikalische Chemie.* **1897,** *22* (1), 289-330.
79. Sakurai, I.; Kawamura, Y., GROWTH-MECHANISM OF MYELIN FIGURES OF PHOSPHATIDYLCHOLINE. *Biochimica et Biophysica Acta* **1984,** *777* (2), 347-351.
80. Reissig, L.; Fairhurst, D. J.; Leng, J.; Cates, M. E.; Mount, A. R.; Egelhaaf, S. U., Three-dimensional structure and growth of myelins. *Langmuir* **2010,** *26* (19), 15192-15199.
81. Sakurai, I.; Suzuki, T.; Sakurai, S., STRUCTURE AND GROWTH-BEHAVIOR OF MYELIN FIGURES. *Molecular Crystals and Liquid Crystals* **1990,** *180*, 305-311.
82. Mishima, K.; Yoshiyama, K., Growth rate of myelin figures of egg-yolk phosphatidylcholine. *Biochimica et Biophysica Acta* **1987,** *904*, 149-153.
83. Mishima, K.; Ogihara, T.; Tomita, M.; Satoh, K., Growth rate of myelin figures for phosphatidycholine and phosphatidylethanolamine. *Chemistry and Physics of Lipids* **1992,** *62*, 87-91.
84. Dave, H.; Surve, M.; Manohar, C.; Bellare, J., Myelin growth and initial dynamics. *J Colloid Interface Sci* **2003,** *264* (1), 76-81.
85. Lin, K. C.; Weis, R. M.; McConnell, H. M., INDUCTION OF HELICAL LIPOSOMES BY CA2+-MEDIATED INTERMEMBRANE BINDING. *Nature* **1982,** *296* (5853), 164-165.
86. Lipowsky, R.; Leibler, S., Unbinding transitions of interacting membranes. *Phys Rev Lett* **1986,** *56* (23), 2541-2544.
87. Petrache, H. I.; Dodd, S. W.; Brown, M. F., Area per Lipid and Acyl Length Distributions in Fluid Phosphatidycholines Determined by 2H NMR Spectroscopy. *Biophysical Journal* **2000,** *79*, 3172-3192.
88. Schuck, S.; Honsho, M.; Ekroos, K.; Shevchenko, A.; Simons, K., Resistance of cell membranes to different detergents. *Proceedings of the National Academy of Sciences of the United States of America* **2003,** *100* (10), 5795-5800.
89. Lichtenberg, D.; Goni, F. M.; Heerklotz, H., Detergent-resistant membranes should not be identified with membrane rafts. *Trends Biochem Sci* **2005,** *30* (8), 430-436.
90. Mishima, K.; Fukuda, K.; Suzuki, K., Double helix formation of phosphatidylcholine myelin figures. *Biochimica et Biophysica Acta* **1992,** *1108*, 115-118.

91. Frette, V.; Tsafrir, I.; Guedeau-Boudeville, M. A.; Jullien, L.; Kandel, D.; Stavans, J., Coiling of cylindrical membrane stacks with anchored polymers. *Phys Rev Lett* **1999,** *83* (12), 2465-2468.
92. Santangelo, C. D.; Pincus, P., Coiling instabilities of multilamellar tubes. *Phys Rev E Stat Nonlin Soft Matter Phys* **2002,** *66* (6 Pt 1), 061501.
93. Helfrich, W., Elastic Properties of Lipid Bilayers: Theory and Possible Experiments. *Zeitschrift für Naturforschung C* **1973,** *28* (11), 693-703.
94. Hurault, J. P., STATIC DISTORTIONS OF A CHOLESTERIC PLANAR STRUCTURE INDUCED BY MAGNETIC OR AC ELECTRIC-FIELDS. *J Chem Phys* **1973,** *59* (4), 2068-2075.
95. Pantaler, E.; Kamp, D.; Haest, C. W. M., Acceleration of phospholipid flip-flop in the erythrocyte membrane by detergents differing in polar head group and alkyl chain length. *Biochimica Et Biophysica Acta - Biomembranes* **2000,** *1509* (1-2), 397-408.
96. Sheetz, M. P.; Singer, S. J., BIOLOGICAL-MEMBRANES AS BILAYER COUPLES - MOLECULAR MECHANISM OF DRUG-ERYTHROCYTE INTERACTIONS. *Proceedings of the National Academy of Sciences of the United States of America* **1974,** *71* (11), 4457-4461.
97. Needham, D.; Zhelev, D. V., Lysolipid Exchange with Lipid Vesicle Membranes. *Annals of Biomedical Engineering* **1995,** *23*, 287-298.
98. Heerklotz, H.; Szadkowska, H.; Anderson, T.; Seelig, J., The sensitivity of lipid domains to small perturbations demonstrated by the effect of triton. *J Mol Biol* **2003,** *329* (4), 793-799.
99. Wang, J. W.; Megha; London, E., Relationship between sterol/steroid structure and participation in ordered lipid domains (lipid rafts): Implications for lipid raft structure and function. *Biochemistry* **2004,** *43* (4), 1010-1018.
100. Schnitzer, E.; Kozlov, M. M.; Lichtenberg, D., The effect of cholesterol on the solubilization of phosphatidylcholine bilayers by the non-ionic surfactant Triton X-100. *Chemistry and Physics of Lipids* **2005,** *135* (1), 69-82.
101. Mattei, B.; Franca, A. D. C.; Riske, K. A., Solubilization of Binary Lipid Mixtures by the Detergent Triton X-100: The Role of Cholesterol. *Langmuir* **2015,** *31* (1), 378-386.
102. Netz, R. R., COMPLETE UNBINDING OF FLUID MEMBRANES IN THE PRESENCE OF SHORT-RANGED FORCES. *Physical Review E* **1995,** *51* (3), 2286-2294.
103. Leibler, S.; Lipowsky, R., COMPLETE UNBINDING AND QUASI-LONG-RANGE ORDER IN LAMELLAR PHASES. *Physical Review B* **1987,** *35* (13), 7004-7009.
104. Pontes, B.; Monzo, P.; Gauthier, N. C., Membrane tension: A challenging but universal physical parameter in cell biology. *Seminars in Cell & Developmental Biology* **2017,** *71*, 30-41.
105. Nissen, J.; Gritsch, S.; Wiegand, G.; Radler, J. O., Wetting of phospholipid membranes on hydrophilic surfaces - Concepts towards self-healing membranes. *European Physical Journal B* **1999,** *10* (2), 335-344.
106. Chung, S. Y.; Kim, Y. M.; Kim, J. G.; Kim, Y. J., Multiphase transformation and Ostwald's rule of stages during crystallization of a metal phosphate. *Nature Physics* **2009,** *5* (1), 68-73.
107. Andelman, D.; Kozlov, M. M.; Helfrich, W., Phase Transitions between Vesicles and Micelles Driven by Competing Curvatures. *Europhysics Letters* **1994,** *25* (3), 231-236.

108. Tanford, C., *The Hydrophobic Effect: Formation of Micelles and Biological Membranes*. 2nd ed.; Wiley: Somerset, NJ, 1980; p 200.
109. Stranski, I. N.; Totomanow, D., Seed formation speed and Ostwald's step rule. *Zeitschrift Fur Physikalische Chemie-Abteilung a-Chemische Thermodynamik Kinetik Elektrochemie Eigenschaftslehre* **1933,** *163* (5/6), 399-408.
110. Mattia, E.; Otto, S., Supramolecular systems chemistry. *Nature Nanotechnology* **2015,** *10* (2), 111-119.
111. Mann, S., Self-assembly and transformation of hybrid nano-objects and nanostructures under equilibrium and non-equilibrium conditions. *Nature Materials* **2009,** *8* (10), 781-792.
112. Cherezov, V.; Clogston, J.; Papiz, M. Z.; Caffrey, M., Room to move: Crystallizing membrane proteins in swollen lipidic mesophases. *J Mol Biol* **2006,** *357* (5), 1605-1618.
113. Landau, E. M.; Rosenbusch, J. P., Lipidic cubic phases: A novel concept for the crystallization of membrane proteins. *Proceedings of the National Academy of Sciences of the United States of America* **1996,** *93* (25), 14532-14535.
114. Koynova, R.; Caffrey, M., An index of lipid phase diagrams. *Chemistry and Physics of Lipids* **2002,** *115* (1-2), 107-219.
115. Nagarajan, R., Molecular Packing Parameter and Surfactant Self-Assembly: The Neglected Role of the Surfactant Tail. *Langmuir* **2002,** *18*, 31-38.
116. Kalam, S.; Abu-Khamsin, S. A.; Kamal, M. S.; Patil, S., Surfactant Adsorption Isotherms: A Review. *ACS Omega* **2021,** *6* (48), 32342-32348.
117. Wennerstrom, H.; Lindman, B., MICELLES - PHYSICAL-CHEMISTRY OF SURFACTANT ASSOCIATION. *Physics Reports-Review Section of Physics Letters* **1979,** *52* (1), 1-86.
118. Puvvada, S.; Blankschtein, D., THERMODYNAMIC DESCRIPTION OF MICELLIZATION, PHASE-BEHAVIOR, AND PHASE-SEPARATION OF AQUEOUS-SOLUTIONS OF SURFACTANT MIXTURES. *J Phy Chem* **1992,** *96* (13), 5567-5579.
119. R., N.; Ruckenstein, E., Theory of Surfactant Self-Assembly: A Predictive Molecular Thermodynamic Approach. *Langmuir* **1991,** *7*, 2934-2969.
120. le Maire, M.; Champeil, P.; Moller, J. V., Interaction of membrane proteins and lipids with solubilizing detergents. *Biochimica Et Biophysica Acta - Biomembranes* **2000,** *1508* (1-2), 86-111.
121. Sood, V. D.; Gross, A. W., *Membrane Proteins as Targets for Biological Drugs*. 2019; p 49-65.
122. Lichtenberg, D.; Ahyayauch, H.; Alonso, A.; Goni, F. M., Detergent solubilization of lipid bilayers: a balance of driving forces. *Trends in Biochemical Sciences* **2013,** *38* (2), 85-93.
123. Tabor, R. F.; Eastoe, J.; Dowding, P. J., A two-step model for surfactant adsorption at solid surfaces. *J Colloid Interface Sci* **2010,** *346* (2), 424-428.
124. Gawrisch, K.; Gaede, H. C.; Mihailescu, M.; White, S. H., Hydration of POPC bilayers studied by 1H-PFG-MAS-NOESY and neutron diffraction. *European Biophysical Journal* **2007,** *36* (4-5), 281-291.
125. Binder, H.; Gawrisch, K., Dehydration Induces Lateral Expansion of Polyunsaturated 18:0 –22:6 Phosphatidylcholine in a New Lamellar Phase. *Biophysical Journal* **2001,** *81*, 969-982.

126. Foglia, F.; Drake, A. F.; Terry, A. E.; Rogers, S. E.; Lawrence, M. J.; Barlow, D. J., Small-angle neutron scattering studies of the effects of amphotericin B on phospholipid and phospholipid-sterol membrane structure. *Biochimica et Biophysica Acta* **2011,** *1808* (6), 1574-1580.
127. Schmiedel, H.; Almasy, L.; Klose, G., Multilamellarity, structure and hydration of extruded POPC vesicles by SANS. *European Biophysical Journal* **2006,** *35* (3), 181-189.
128. Dymond, M. K., Lipid monolayer spontaneous curvatures: A collection of published values. *Chemistry and Physics of Lipids* **2021,** *239*, 105117.
129. Linke, D., Detergents: an overview. *Methods Enzymol* **2009,** *463*, 603-617.
130. Kučerka, N.; Tristram-Nagle, S.; Nagle, J. F., Structure of fully hydrated fluid phase lipid bilayers with monounsaturated chains. *J Membr Biol* **2005,** *208* (3), 193-202.
131. Alessandrini, A.; Seeger, H. M.; Di Cerbo, A.; Caramaschi, T.; Facci, P., What do we really measure in AFM punch-through experiments on supported lipid bilayers? *Soft Matter* **2011,** *7* (15), 7054-7064.
132. Richter, R. P.; Brisson, A., Characterization of Lipid Bilayers and Protein Assemblies Supported on Rough Surfaces by Atomic Force Microscopy. *Langmuir* **2003,** *19*, 1632-1640.
133. Garcia-Manyes, S.; Sanz, F., Nanomechanics of lipid bilayers by force spectroscopy with AFM: a perspective. *Biochimica et Biophysica Acta* **2010,** *1798* (4), 741-749.
134. Relat-Goberna, J.; Beedle, A. E. M.; Garcia-Manyes, S., The Nanomechanics of Lipid Multibilayer Stacks Exhibits Complex Dynamics. *Small* **2017,** *13* (24), 1700147.
135. Yamazaki, M.; Tamba, Y., The Single GUV Method for Probing Biomembrane Structure and Function. *e-Journal of Surface Science and Nanotechnology* **2005,** *3*, 218-227.
136. PubChem Compound Summary for CID 84703, *N*-Dodecyl-*N,N*-dimethyl-3-ammonio-1-propanesulfonate. https://pubchem.ncbi.nlm.nih.gov/compound/3-_dodecyl_dimethyl_azaniumyl_propane-1-sulfonate (accessed October 12).
137. PubChem Compound Summary for CID 5497103, 1-Palmitoyl-2-oleoyl-*sn*-glycero-3-phosphocholine. https://pubchem.ncbi.nlm.nih.gov/compound/1-Palmitoyl-2-oleoyl-sn-glycero-3-phosphocholine (accessed October 11).
138. PubChem Compound Summary for CID 16081932, 1-(9Z-octadecenoyl)-*sn*-glycero-3-phosphocholine. https://pubchem.ncbi.nlm.nih.gov/compound/1-_9Z-octadecenoyl_-sn-glycero-3-phosphocholine (accessed October 12).
139. Tan, A.; Ziegler, A.; Steinbauer, B.; Seelig, J., Thermodynamics of Sodium Dodecyl Sulfate Partitioning into Lipid Membranes. *Biophysical Journal* **2002,** *83*, 1547-1556.
140. Partearroyo, M. A.; Urbaneja, M. A.; Goñi, F. M., Effective detergent/lipid ratios in the solubilization of phosphatidylcholine vesicles by Triton X- 100. *The FEBS Journal* **1992,** *302* (2), 138-140.
141. Hishida, M.; Tanaka, K., Transition of the hydration state of a surfactant accompanying structural transitions of self-assembled aggregates. *J Phys Condens Matter* **2012,** *24* (28), 284113.
142. Yui, H.; Guo, Y.; Koyama, K.; Sawada, T.; John, G.; Yang, B.; Masuda, M.; Shimizu, T., Local Environment and Property of Water inside the Hollow Cylinder of a Lipid Nanotube. *Langmuir* **2005,** *21*, 721-727.
143. Karaman, M. E.; Ninham, B. W.; Pashley, R. M., Some Aqueous Solution and Surface Properties of Dialkyl Sulfosuccinate Surfactants. *J Phys Chem* **1994,** *98*, 11512-11518.

144. Maneedaeng, A.; Flood, A. E., Synergisms in Binary Mixtures of Anionic and pH-Insensitive Zwitterionic Surfactants and Their Precipitation Behavior with Calcium Ions. *J Surfactants Deterg* **2016,** *20* (1), 263-275.
145. Boles, M. A.; Engel, M.; Talapin, D. V., Self-Assembly of Colloidal Nanocrystals: From Intricate Structures to Functional Materials. *Chem Rev* **2016,** *116* (18), 11220-11289.
146. Sato, Y.; Endo, M.; Morita, M.; Takinoue, M.; Sugiyama, H.; Murata, S.; Nomura, S.-i. M.; Suzuki, Y., Environment-Dependent Self-Assembly of DNA Origami Lattices on Phase-Separated Lipid Membranes. *Advanced Materials Interfaces* **2018,** *5* (14), 1800437.
147. Baxter, P. N. W.; Khoury, R. G.; Lehn, J.-M.; Baum, G.; Fenske, D., Adaptive Self-Assembly: Environment-Induced Formation and Reversible Switching of Polynuclear Metallocyclophanes. *Chemistry* **2000,** *6* (22), 4140-4148.
148. Seiwert, D.; Witt, H.; Ritz, S.; Janshoff, A.; Paulsen, H., The Nonbilayer Lipid MGDG and the Major Light-Harvesting Complex (LHCII) Promote Membrane Stacking in Supported Lipid Bilayers. *Biochemistry* **2018,** *57* (15), 2278-2288.
149. Fragata, M.; Ohnishi, S.; Asada, K.; Ito, T.; Takahasi, M., Lateral Diffusion of Plastocyanin in Multilamellar Mixed-Lipid Bilayers Studied by Fluorescence Recovery after Photobleaching. *Biochemistry* **1984,** *23*, 4044-4051.
150. Derzko, Z.; Jacobson, K., Comparative lateral diffusion of fluorescent lipid analogues in phospholipid multibilayers. *Biochemistry* **1980,** *19* (26), 6050-6057.
151. Blatt, E.; Vaz, W. L. C., THE EFFECTS OF Ca2+ ON LIPID DIFFUSION. *Chemistry and Physics of Lipids* **1986,** *41*, 183-194.
152. Silva, G. T. M.; Quina, F. H., Ion–micelle interactions and the modeling of reactivity in micellar solutions of simple zwitterionic sulfobetaine surfactants. *Current Opinion in Colloid & Interface Science* **2019,** *44*, 168-176.
153. Weers, J. G.; Rathman, J. F.; Axe, F. U.; Crichlow, C. A.; Foland, L. D.; Scheuing, D. R.; Wiersema, R. J.; Zielske, A. G., Effect of the Intramolecular Charge Separation Distance on the Solution Properties of Betaines and Sulfobetaines. *Langmuir* **1991,** *7*, 854-867.
154. Alves, M.; Bales, B. L.; Peric, M., Effect of lysophosphatidylcholine on the surface hydration of phospholipid vesicles. *Biochimica et Biophysica Acta* **2008,** *1778* (2), 414-422.
155. Aikawa, T.; Okura, H.; Kondo, T.; Yuasa, M., Comparison of Carboxybetaine with Sulfobetaine as Lipid Headgroup Involved in Intermolecular Interaction between Lipids in the Membrane. *ACS Omega* **2017,** *2* (9), 5803-5812.
156. Pfeiffer, H.; Klose, G.; Heremans, K., Thermodynamic and structural behaviour of equimolar POPC/CnE4 (n=8, 12, 16) mixtures by sorption gravimetry, 2H NMR spectroscopy and X-ray diffraction. *Chemitry and Physics of Lipids* **2010,** *163* (3), 318-328.
157. Vanni, S.; Riccardi, L.; Palermo, G.; De Vivo, M., Structure and Dynamics of the Acyl Chains in the Membrane Trafficking and Enzymatic Processing of Lipids. *Acc Chem Res* **2019,** *52* (11), 3087-3096.
158. Henriksen, J. R.; Andresen, T. L.; Feldborg, L. N.; Duelund, L.; Ipsen, J. H., Understanding detergent effects on lipid membranes: a model study of lysolipids. *Biophysical Journal* **2010,** *98* (10), 2199-2205.

159. Seu, K. J.; Cambrea, L. R.; Everly, R. M.; Hovis, J. S., Influence of lipid chemistry on membrane fluidity: tail and headgroup interactions. *Biophysical Journal* **2006,** *91* (10), 3727-3735.
160. Sehgal, P.; Doe, H.; Bakshi, M. S., Solubilization of Phospholipid Vesicular Structures into Mixed Micelles of Zwitterionic Surfactants. *J Surfactants Deterg* **2003,** *6* (1), 31-37.
161. Cheng, C.-j.; Qu, G.-m.; Wei, J.-j.; Yu, T.; Ding, W., Thermodynamics of Micellization of Sulfobetaine Surfactants in Aqueous Solution. *J Surfactants Deterg* **2012,** *15* (6), 757-763.
162. McLachlan, A. A.; Singh, K.; Marangoni, D. G., A conformational investigation of zwitterionic surfactants in the micelle via 13C chemical shift measurements and 2D NOESY spectroscopy. *Colloid and Polymer Science* **2010,** *288* (6), 653-663.
163. Greenspan, L., Humidity Fixed Points of Binary Saturated Aqueous Solutions. *Journal of Research of the National Bureau of Standards* **1977,** *81A* (1), 89-96.
164. Ma, Y.; Ghosh, S. K.; Bera, S.; Jiang, Z.; Tristram-Nagle, S.; Lurio, L. B.; Sinha, S. K., Accurate calibration and control of relative humidity close to 100% by X-raying a DOPC multilayer. *Phys Chem Chem Phys* **2015,** *17* (5), 3570-3576.
165. Salditt, T., Thermal fluctuations and stability of solid-supported lipid membranes. *J Phys: Cond Matt* **2005,** *17* (6), R287-R314.
166. Katsaras, J., X-ray diffraction studies of oriented lipid bilayers. *Biochemistry and Cell Biology* **1995,** *73*, 209-218.
167. Tristram-Nagle, S.; Liu, Y.; Legleiter, J.; Nagle, J. F., Structure of Gel Phase DMPC Determined by X-Ray Diffraction. *Biophysical Journal* **2002,** *83*, 3324-3335.
168. Li, J.-R.; Lusker, K. L.; Yu, J.-J.; Garno, J. C., Engineering the Spatial Selectivity of Surfaces at the Nanoscale Using Particle Lithography Combined with Vapor Deposition of Organosilanes. *ACS Nano* **2009,** *3* (7), 2023-2035.
169. Zhang, J.; Yu, H.; Harris, B.; Zheng, Y.; Celik, U.; Na, L.; Faller, R.; Chen, X.; Haudenschild, D. R.; Liu, G. Y., New Means to Control Molecular Assembly. *J Phys Chem C Nanomater Interfaces* **2020,** *124* (11), 6405-6412.
170. Florin, E.-L.; Rief, M.; Lehmann, H.; Ludwig, M.; Dornmair, C.; Moy, V. T.; Gaub, H. E., Sensing specific molecular interactions with the atomic force microscope. *Biosensors & Bioelectronics* **1995,** *10*, 895-901.
171. Johnsen, S., The Red and the Black: Bioluminescence and the Color of Animals in the Deep Sea. *Integr. Comp. Biol.* **2005,** *45*, 234-246.
172. Johnsen, S., Cryptic and conspicuous coloration in the pelagic environment. *Proc Biol Sci* **2002,** *269* (1488), 243-256.
173. Johnsen, S., Cryptic coloration and mirrored sides as camouflage strategies in near-surface pelagic habitats: Implications for foraging and predator avoidance. *Limnol. Oceanogr.* **2003,** *38* (3), 1277-1288.
174. Brady, P. C.; Gilerson, A. A.; Kattawar, G. W.; Sullivan, J. M.; Twardowski, M. S.; Dierssen, H. M.; Gao, M.; Travis, K.; Etheredge, R. I.; Tonizzo, A.; Ibrahim, A.; Carrizo, C.; Gu, Y.; Russell, B. J.; Mislinski, K.; Zhao, S.; Cummings, M. E., Open-ocean fish reveal an omnidirectional solution to camouflage in polarized environments. *Science* **2015,** *350* (6263), 965-969.
175. Crookes, W. J.; Ding, L.-L.; Huang, Q. L.; Kimbell, J. R.; Horwitz, J.; McFall-Ngai, M. J., Reflectins: The Unusual Proteins of Squid Reflective Tissues. *Science* **2004,** *303*, 235-238.

176. DeMartini, D. G.; Krogstad, D. V.; Morse, D. E., Membrane invaginations facilitate reversible water flux driving tunable iridescence in a dynamic biophotonic system. *Proceedings of the National Academy of Sciences of the United States of America* **2013,** *110* (7), 2552-2556.
177. Levenson, R.; Bracken, C.; Bush, N.; Morse, D. E., Cyclable Condensation and Hierarchical Assembly of Metastable Reflectin Proteins, the Drivers of Tunable Biophotonics. *J Biol Chem* **2016,** *291* (8), 4058-4068.
178. Levenson, R.; Bracken, C.; Sharma, C.; Santos, J.; Arata, C.; Malady, B.; Morse, D. E., Calibration between trigger and color: Neutralization of a genetically encoded coulombic switch and dynamic arrest precisely tune reflectin assembly. *J Biol Chem* **2019,** *294* (45), 16804-16815.
179. DeMartini, D. G.; Izumi, M.; Weaver, A. T.; Pandolfi, E.; Morse, D. E., Structures, Organization, and Function of Reflectin Proteins in Dynamically Tunable Reflective Cells. *J Biol Chem* **2015,** *290* (24), 15238-15249.
180. Tao, A. R.; DeMartini, D. G.; Izumi, M.; Sweeney, A. M.; Holt, A. L.; Morse, D. E., The role of protein assembly in dynamically tunable bio-optical tissues. *Biomaterials* **2010,** *31* (5), 793-801.
181. Naughton, K. L.; Phan, L.; Leung, E. M.; Kautz, R.; Lin, Q.; Van Dyke, Y.; Marmiroli, B.; Sartori, B.; Arvai, A.; Li, S.; Pique, M. E.; Naeim, M.; Kerr, J. P.; Aquino, M. J.; Roberts, V. A.; Getzoff, E. D.; Zhu, C.; Bernstorff, S.; Gorodetsky, A. A., Self-Assembly of the Cephalopod Protein Reflectin. *Adv Mater* **2016,** *28* (38), 8405-8412.
182. Emami, S.; Su, W. C.; Purushothaman, S.; Ngassam, V. N.; Parikh, A. N., Permeability and Line-Tension-Dependent Response of Polyunsaturated Membranes to Osmotic Stresses. *Biophysical Journal* **2018,** *115* (10), 1942-1955.
183. Hanson, J. M.; Gettel, D. L.; Tabaei, S. R.; Jackman, J.; Kim, M. C.; Sasaki, D. Y.; Groves, J. T.; Liedberg, B.; Cho, N. J.; Parikh, A. N., Cholesterol-Enriched Domain Formation Induced by Viral-Encoded, Membrane-Active Amphipathic Peptide. *Biophysical Journal* **2016,** *110* (1), 176-187.
184. Li, L.; Vorobyov, I.; Allen, T. W., The different interactions of lysine and arginine side chains with lipid membranes. *J Phys Chem B* **2013,** *117* (40), 11906-11920.
185. Vostrikov, V. V.; Hall, B. A.; Greathouse, D. V.; Koeppe II, R. E.; Sansom, M. S., Changes in Transmembrane Helix Alignment by Arginine Residues Revealed by Solid-State NMR Experiments and Coarse-Grained MD Simulations. *J Am Chem Soc* **2010,** *132*, 5803-5811.
186. Iwunze, M. O., The characterization of the fluorescence of l-histidine in simulated body fluid. *J Photochem Photobiol A* **2007,** *186* (2-3), 283-289.
187. Tiemeyer, S.; Paulus, M.; Tolan, M., Effect of surface charge distribution on the adsorption orientation of proteins to lipid monolayers. *Langmuir* **2010,** *26* (17), 14064-14067.
188. Schneggenburger, P. E.; Beerlink, A.; Weinhausen, B.; Salditt, T.; Diederichsen, U., Peptide model helices in lipid membranes: insertion, positioning, and lipid response on aggregation studied by X-ray scattering. *European Biophysical Journal* **2011,** *40* (4), 417-436.
189. Baeza, N.; Mercade, E., Relationship Between Membrane Vesicles, Extracellular ATP and Biofilm Formation in Antarctic Gram-Negative Bacteria. *Microb Ecol* **2021,** *81* (3), 645-656.

190. Flemming, H. C.; Wingender, J., The biofilm matrix. *Nat Rev Microbiol* **2010,** *8* (9), 623-633.
191. Remis, J. P.; Costerton, J. W.; Auer, M., Biofilms: structures that may facilitate cell-cell interactions. *ISME J* **2010,** *4* (9), 1085-1087.
192. van Niel, G.; D'Angelo, G.; Raposo, G., Shedding light on the cell biology of extracellular vesicles. *Nat Rev Mol Cell Biol* **2018,** *19* (4), 213-228.
193. Turnbull, L.; Toyofuku, M.; Hynen, A. L.; Kurosawa, M.; Pessi, G.; Petty, N. K.; Osvath, S. R.; Carcamo-Oyarce, G.; Gloag, E. S.; Shimoni, R.; Omasits, U.; Ito, S.; Yap, X.; Monahan, L. G.; Cavaliere, R.; Ahrens, C. H.; Charles, I. G.; Nomura, N.; Eberl, L.; Whitchurch, C. B., Explosive cell lysis as a mechanism for the biogenesis of bacterial membrane vesicles and biofilms. *Nature Communications* **2016,** *7*, 11220.
194. He, X.; Yuan, F.; Lu, F.; Yin, Y.; Cao, J., Vancomycin-induced biofilm formation by methicillin-resistant Staphylococcus aureus is associated with the secretion of membrane vesicles. *Microb Pathog* **2017,** *110*, 225-231.
195. Schooling, S. R.; Beveridge, T. J., Membrane vesicles: an overlooked component of the matrices of biofilms. *J Bacteriol* **2006,** *188* (16), 5945-5957.
196. Zarnowski, R.; Noll, A.; Chevrette, M. G.; Sanchez, H.; Jones, R.; Anhalt, H.; Fossen, J.; Jaromin, A.; Currie, C.; Nett, J. E.; Mitchell, A.; Andes, D. R., Coordination of fungal biofilm development by extracellular vesicle cargo. *Nature Communications* **2021,** *12* (1), 6235-6243.
197. Toyofuku, M.; Nomura, N.; Eberl, L., Types and origins of bacterial membrane vesicles. *Nat Rev Microbiol* **2019,** *17* (1), 13-24.
198. Yonezawa, H.; Osaki, T.; Kurata, S.; Fukuda, M.; Kawakami, H.; Ochiai, K.; Hanawa, T.; Kamiya, S., Outer membrane vesicles of Helicobacter pylori TK1402 are involved in biofilm formation. *BMC Microbiol* **2009,** *9*, 197.
199. Wang, Y.; Hoffmann, J. P.; Baker, S. M.; Bentrup, K. H. Z.; Wimley, W. C.; Fuselier, J. A.; Bitoun, J. P.; Morici, L. A., Inhibition of Streptococcus mutans biofilms with bacterial-derived outer membrane vesicles. *BMC Microbiol* **2021,** *21* (1), 234.
200. Nakao, R.; Myint, S. L.; Wai, S. N.; Uhlin, B. E., Enhanced Biofilm Formation and Membrane Vesicle Release by Escherichia coli Expressing a Commonly Occurring Plasmid Gene, kil. *Front Microbiol* **2018,** *9*, 2605.
201. Kuhn, A.; Koch, H. G.; Dalbey, R. E., Targeting and Insertion of Membrane Proteins. *EcoSal Plus* **2017,** *7* (2).
202. McKay, M. J.; Marr, K. A.; Price, J. R.; Greathouse, D. V.; Koeppe, R. E., 2nd, Lipid-Dependent Titration of Glutamic Acid at a Bilayer Membrane Interface. *ACS Omega* **2021,** *6* (12), 8488-8494.
203. Rajagopalan, V.; Greathouse, D. V.; Koeppe, R. E., 2nd, Influence of glutamic acid residues and pH on the properties of transmembrane helices. *Biochimica et Biophysica Acta - Biomembranes* **2017,** *1859* (3), 484-492.
204. Ladha, S.; Mackie, A. R.; Harvey, L. J.; Clark, D. C.; Lea, E. J. A.; Brullemans, M.; Duclohier, H., Lateral Diffusion in Planar Lipid Bilayers: A Fluorescence Recovery after Photobleaching Investigation of Its Modulation by Lipid Composition, Cholesterol, or Alamethicin Content and Divalent Cations. *Biophysical Journal* **1996,** *71*, 1364-1373.
205. Pucadyil, T. J.; Chattopadhyay, A., Effect of cholesterol on lateral diffusion of fluorescent lipid probes in native hippocampal membranes. *Chemistry and Physics of Lipids* **2006,** *143* (1-2), 11-21.

206. Miura, K., Bleach correction ImageJ plugin for compensating the photobleaching of time-lapse sequences. *F1000Res* **2020,** *9*, 1494.
207. Scientific, T.-F. 2-YT Broth.
208. Scientific, T.-F. Bacto Tryptone. (accessed 2023/03/20).
209. Scientific, T.-F. Yeast Extract. (accessed 03/20).